

---

# Everything from Nothing – Of Haloes and Voids

Benjamin Seidel

---



Munich 2022



---

# Aus dem Nichts das Ganze – Von Haufen und Leere

Benjamin Seidel

---



München 2022



---

# Everything from Nothing – Of Haloes and Voids

Benjamin Seidel

---

**Master's Thesis**

at the University Observatory Munich

Ludwig Maximilian University

Submitted by

**Benjamin Seidel**

born in Munich

Supervised by

Rhea-Silvia Remus

Klaus Dolag

Munich, 09.09.2022



# Contents

<b>1</b>	<b>Introduction</b>	<b>1</b>
<b>2</b>	<b>Why we build the box: Numerical Simulations</b>	<b>5</b>
2.1	The need for cosmological simulations . . . . .	5
2.2	An artist needs a canvas: Modelling spacetime . . . . .	5
2.3	Initial conditions . . . . .	6
2.4	Gravity . . . . .	6
2.5	Hydrodynamics . . . . .	7
2.6	Sub-grid models . . . . .	7
2.7	Subfind . . . . .	7
2.8	Boxes . . . . .	8
2.9	Outside the box: Summing up . . . . .	8
<b>3</b>	<b>The Emergence of Large-Scale Structure</b>	<b>11</b>
3.1	The Primordial Gaussian Field . . . . .	11
3.2	Linear Theory . . . . .	13
3.3	Beyond Linear Theory: Press-Schechter . . . . .	15
3.3.1	Roughly counting: Press-Schechter Formalism . . . . .	16
3.3.2	A little less roughly counting: Excursion Set theory and Extended Press-Schechter . . . . .	17
3.3.3	A hierarchy of clumps: From clusters to galaxies – or vice versa? . . . . .	19
3.3.4	The Mass accretion history of dark matter haloes . . . . .	19
3.3.5	From spherical cows to ellipsoidal ones . . . . .	21
3.4	The cosmic web . . . . .	22
3.4.1	Approaching the web: The Zel’dovich approximation . . . . .	22
3.5	Not complicated enough: Enter the Baryons . . . . .	23
3.6	So far from the theorists: Summary . . . . .	25
<b>4</b>	<b>Feeding the hungry: The in- and outflows of Magneticum haloes</b>	<b>27</b>
4.1	Flowing in the cosmos . . . . .	27
4.2	To answer a question, you first have to ask it: Goals . . . . .	29
4.3	Measurements: Setup and parameters . . . . .	30
4.3.1	Reconstructing the fields . . . . .	30

4.4	A sky full of flows: The spatial distribution of mass accretion and decretion	32
4.5	Must what goes in indeed come out? – Accretion rates across the scales . . .	39
4.6	How are you enriching yourselves?– Flow metallicity evolution . . . . .	42
4.7	Summing up: What we learned about haloes . . . . .	46
<b>5</b>	<b>The Presence of Absence: Cosmic Voids</b>	<b>49</b>
5.1	One man’s gain is an other’s loss: Decretion . . . . .	49
5.2	Turning the top hat inside out: Model of an isolated void . . . . .	50
5.3	Empty in numbers: The void size function . . . . .	51
5.3.1	The two-threshold excursion set formalism . . . . .	51
5.4	Nothing is ever really empty: Void substructure and other complications . .	53
5.4.1	A web between the web: Structure in voids . . . . .	53
5.4.2	Don’t leave me here to die: Void galaxies . . . . .	53
5.5	I have no sphere: The non-spherical shapes of voids . . . . .	54
5.6	These are(n’t) the voids you’re looking for: Void finding algorithms . . . .	56
5.7	Summing up: The end of the desert . . . . .	57
<b>6</b>	<b>Shaping up: Tracing cosmological parameters with void shapes</b>	<b>59</b>
6.1	Nothing (else) matters: Void shapes and cosmology . . . . .	59
6.2	Nothing is clear: Goals and questions . . . . .	60
6.3	Nothing on my mind: Tools and Methods . . . . .	60
6.3.1	VIDE setup . . . . .	60
6.3.2	Parameter Activity: The multi cosmology box from <i>Magneticum</i> . .	61
6.3.3	Resulting void catalogs . . . . .	62
6.4	The ellipticity distribution . . . . .	63
6.5	The big nothing: Void size and ellipticity . . . . .	67
6.6	The shape of nothing: Conclusions . . . . .	69
<b>7</b>	<b>Weaving it all together: Conclusions</b>	<b>71</b>
<b>A</b>	<b>Parents vs. children: Impact of the void hierarchy</b>	<b>73</b>
	<b>References</b>	<b>75</b>

# Chapter 1

## Introduction

“The world is the totality of facts, not of things”

---

Ludwig Wittgenstein, *Tractatus*

**Motivation** The standard model of the universe is rich in intriguing dichotomies. Among the most fascinating is the chasm between light and darkness, directly related to the divide of matter into two species: Ordinary – or baryonic – matter obeys the laws we intuitively understand from our everyday framework where matter has internal pressure and the ability to dissipate energy via heat and radiation. This is due to the fact that it couples to the electromagnetic field, which makes this type of matter directly observable to us. According to the current concordance model of cosmology however, most matter isn’t like that. From indirect observations, modern cosmology deduces that over 80% of the matter content of the universe interacts only gravitationally. Therefore it is cold, dark and pressureless, earning its name ‘(cold) dark matter’. Due to its proportional dominance over regular matter, most models of large-scale structure formation only consider the dark and gravitational side of the universe. As a consequence of gravity acting the same on all scales, a salient feature of these models is their self-similarity of structures. While this holds true to some degree for the largest of structures the increasing importance of baryonic physics (Halle & Combes, 2013) tends to break these self-similarities (Böhringer et al., 2012) around collapsed structures in conspiracy with gravitational non-linearity. To understand the complete palette of cosmic structures holistically, the coupling between these two regimes and the influence the smaller scale baryonic physics can exert on large scale structures need to be understood better. The most promising environments for studies of this transition are found in the intermediate between high density and relative emptiness. The regions of interest can both be interpreted as both the outer zones of collapsed structures and the walls of the relatively empty spaces in between them. As both views offer unique insights into cosmic structures and the influence of baryons on their evolution, this thesis will investigate the matter at hand from both sides of the density dichotomy. Because of the highly non-linear nature of the problem, numerical

simulations with their increasingly realistic baryonic physics present an ideal framework to study these complex environments from a theoretical perspective.

**The beginning of it all: The standard model** The history of structures in the universe starts with a bang: In concordance cosmology the universe began its existence as a hot plasma in a violent **big bang** and has been expanding ever since (albeit at different rates in different epochs). This standard model is called  $\Lambda$ CDM cosmology, named after its two principal components, cold dark matter (CDM) and dark energy ( $\Lambda$ ) (the previously mentioned baryons are usually considered a part of CDM from a cosmological perspective). The rate of expansion is governed by the ratio of the matter content to  $\Lambda$  (Friedman, 1922), with the former acting as a contracting force via gravity and the latter providing an expansive impetus. During the very energetic and chaotic first instants of the existence of our cosmos, the seeds that grow into the richness of structure we observe today, were already planted: The theoretical foundation of the  $\Lambda$ CDM concordance model is the **cosmological principle**, according to which the distribution of matter and energy in the universe is both homogeneous and isotropic on very large scales. This was validated by a serendipitous discovery in the 1960s (Penzias & Wilson, 1965) dubbed the **Cosmic Microwave Background** (CMB from here on). It revealed the radiation emitted at the time the plasma from the big bang had cooled enough by expansion for the photons to escape it for the first time, to be in accordance with this axiom. However there were deviations from this homogeneity. These inhomogeneities are today believed to be remnants of the fluctuations of a scalar quantum field (a later addition to  $\Lambda$ CDM) that caused a very short spurt of exponential expansion called the **inflationary epoch** (Mukhanov, 2005). More and more precise measurements of the CMB (Planck Collaboration, 2020) have revealed that the predictions of the inflationary model (Hawking (1982), Guth (1981), Dodelson & Schmidt (2021)) hold true to impressive precision. At the time of the escape of the first photons, the initially small density fluctuations arising had been spatially stretched out by the rapid expansion of the inflationary epoch and shortly afterwards began to evolve predominantly dictated by gravity, starting the formation of the structures we observe today:

**A quick guide to cosmic structures** In contrast to the chaotic systems we are used to in our baryon dominated world, on large scales we find the universe to be surprisingly structured, primarily by gravity. There is a distinct hierarchy of structures, inspiration for the hierarchical models of structure formation we will discuss later. The smallest and most numerous arrangements of matter for the scope of this thesis are galaxies. These basic building blocks of large scale structures consist of an extended dark matter halo with the baryonic matter condensed more centrally into dense features due to its ability to radiate away energy. In these dense baryonic regions the gas can further condense to form stars. The light emitted by these stars makes galaxies our primary tracer of large scale structure in observational studies. They exhibit a wide range of morphologies and dynamical characteristics due to their susceptibility to environmental influences like tidal torques and asymmetries in their

accretion. Because of this, understanding their coupling to their cosmic environments is one of the most important goals of galaxy formation theory, with many efforts both in observations (Papovich et al., 2018) and simulations (Gouin et al., 2022), (Fortuné, 2022) towards this goal. Moving on to larger scales, the distribution of these galaxies is exceedingly tidy. It was recognized relatively early on in the first large-scale surveys, that most of them are arranged in thin, string like arrangements called **filaments**, the occasional flat, **sheet**-like structure and the busiest of busy convergence points of these filaments and sheets, called **nodes**, forming a structure with a distinct, web-like topology, earning it the name **cosmic web** (Bond et al., 1991). The nodes of the cosmic web house the most massive clusters of galaxies, the most massive virialized structures in the universe. In addition to thousands of galaxies, **galaxy clusters** also contain hot gas atmospheres, which due to the energies involved is hot enough to emit in almost every observable waveband. Because of this and a strong self-similarity in many of their properties, these giants have contributed massively to advances made in cosmology and astrophysics over the last decades. Especially their gaseous outskirts, though notoriously difficult to observe due to the low luminosities (Walker et al., 2019), have been the subject of numerous environmental studies focused on the behaviour of the baryonic gas with regards to shocks (Zhang et al., 2020), and the overall geometry of the gas distribution (Gouin et al., 2022). High-Mach number accretion shocks in the outskirts of galaxy clusters are of special interest to us, as their heating might drive powerful outflows into the underdense regions surrounding the clusters and thus provide a large-scale baryonic feedback. As galaxy clusters are fed by galaxies in-falling along the filaments of the cosmic web, another focus of recent research has been the interaction of filaments and cluster outskirts (Rost et al., 2021) as well as the effect of filaments on the internal cluster properties (Zinger et al., 2016). Following the epigraph by Wittgenstein cited above, there is a fact we need to add to our hierarchy of things. A direct consequence of most of the mass accumulating in comparatively thin structures that do not fill much space is the presence of very nearly empty space in between those structures. Though not astrophysical 'objects' in a strict sense, these cosmic **voids** are structures of utmost importance nonetheless. As their walls are defined by the shape of the local cosmic web, they provide a unique view on the properties and evolution of the large scale structure. During the course of the last couple of years, voids have become a popular tool for numerous cosmological applications: Notable examples include the estimation of cosmological parameters via the void-galaxy correlation function of voids stacked to real-space spherical shapes (Hamaus et al., 2020), studying the effects of massive neutrinos on the void clustering bias (Schuster et al., 2019) or trying to resolve the Hubble tension by postulating a large local void impacting locally measured recession velocities (Castello et al., 2022). Furthering our understanding of these cosmic holes and how they evolve is therefore an important task for modern structure formation theory.

**Synopsis** In summary this thesis will feature two parts, dedicated to the dense and the underdense side of the density dichotomy. The principal questions we will try to answer will be:

- How self-similar is the accretion and decretion flow in the outskirts of simulated haloes in the presence of baryons?
- What is the difference between gravity dominated and baryon dominated flows in the outskirts of haloes?
- Where does outflowing gas in the outskirts of haloes originate?
- Is there an influence of baryonic physics on the relationship between void shapes and cosmological parameters?
- How do baryons influence the evolution of void shapes?

In chapter 2 I introduce the general principles behind numerical simulations and the main reasons for using them. Chapters 3 and 5 provide the long versions of the short introductions – featured above – to haloes and voids respectively. The first chapter featuring numerical results is chapter 4, in which the mass flows around haloes are investigated in the context of the dark matter vs. baryons dichotomy. Chapter 6 will be concerned with voids and their shapes. Here we will study how these shapes are tied to the cosmological initial conditions within  $\Lambda$ CDM and how this relation is influenced by the presence of baryons. Finally chapter 7 will provide a summary and re-contextualisation of these separate findings.

# Chapter 2

## Why we build the box: Numerical Simulations

### 2.1 The need for cosmological simulations

While the evolution of structures is governed by relatively simple and linear dynamics at the largest of scales, non-linearity is emerging quickly once structures start to collapse. Mathematically this means that the existence of analytical solutions is not guaranteed anymore, necessitating either approximations that oversimplify the dynamics significantly or numerical approaches (where simplifications are mitigated with computational power). This necessity is further enhanced by the presence of baryonic physics aggravating the non-linearity of the problem and coupling the purely gravitational physics to hydrodynamical effects. To realistically model the universe in detail but also on very large scales simultaneously there simply is no way around cosmological simulations. The following chapter will give an overview of the ingredients needed to build a simulation box for reliable comparisons to observations. Because this thesis will be limited to the *Magneticum* (<http://www.magneticum.org/simulations.html>) suite of simulations based on the integrator Gadget-3, the focus will be on the methods used in this specific set.

### 2.2 An artist needs a canvas: Modelling spacetime

A realistic cosmological simulation must be built on an expanding spacetime. The standard approach, compatible with the current concordance model is to implement a **flat FLRW** metric to model the expansion. This expansion depends only on the initial conditions, namely the initial ratio of matter density to dark energy and is governed by the **Friedmann equations** (Friedman, 1922), derived from general relativity. These differential equations describe the evolution of the **scale factor**  $a$  in terms of the contents of the universe. As the different components evolve differently with time, there are different epochs in the evolution of the scale factor. Because the dark energy density is constant, while the matter density evolves with  $a^{-3}$  (from simple geometrical considerations), late times are generally dark-energy

dominated, with the accelerated expansion that cosmological surveys have measured (Riess et al., 1998). It is generally convenient to move the metric to the background and decouple the evolution of the local densities from it (as this doesn't influence the overall metric evolution). This is done by switching to a **co-moving** frame i.e. all quantities are computed relative to a coordinate frame that expands with the metric. For further computational convenience, the integration based on the Gadget-3 code (Springel, 2005) additionally transforms the time coordinate, so the velocities and accelerations used are in an altered reference frame.

## 2.3 Initial conditions

As we will see later, initial conditions play a very important role in structure formation. It is therefore imperative to set up realistic starting conditions for cosmological simulations. First and foremost a proper power spectrum for the initial perturbations must be employed. *Magneticum* implements a WMAP7 power spectrum (Komatsu et al., 2011) with a spectral index  $n=0.963$ . There are various ways of obtaining realistic initial conditions. One of the most common methods involves setting up a glass-like state by initializing a random distribution with the appropriate amplitude spectrum and letting it evolve with negative gravity until a stable configuration is obtained. This glass state is then used as the matter distribution at the first time step, typically with a redshift  $z \approx 100 - 200$ . After setting up in this way, gravity is given free reign.

## 2.4 Gravity

The Gadget-3 integrator discretizes the action of gravity on the dark matter (or baryonic) fluid into the N-body interaction of representative particles. Unlike grid based codes, this means that the resolution is given by the number of particles the total mass is discretized into instead of a well defined spatial resolution. It is of great importance to balance the force resolution against computational efficiency to allow the forces to be resolved enough for modelling the short-range evolution accurately, while being able to afford large enough box sizes for realistic large-scale structures to form. To this end, Gadget-3 uses a hybrid of two different methods for the force calculation, effectively splitting the potential a particle feels into a long range and a short range contribution. The *Tree* method (Barnes & Hut, 1986) is optimized for short range interaction. As its name indicates it puts particles on a hierarchical tree by subdividing the volume into cells recursively, stopping when each subdivision contains a single particle. To calculate the force on a single particle, a tree walk is performed: Cells that are sufficiently far away such that their substructure doesn't influence the calculation above a certain threshold are counted as single "particles". If the error threshold is exceeded, its sub-cells are considered individually. This method calculates short range forces very precisely, whilst sacrificing accuracy for precision at long range. The long range force terms are therefore considered via the *Particle-Mesh (PM)* method. Here

the long range potential is calculated by putting particles on a grid and evaluating the Poisson equation in discrete Fourier space. With the *Fast-Fourier-Transform (FFT)* method this can be done very efficiently. Combined with a cutoff scale to distinguish long range and short range, these two force calculation methods give the Tree-PM scheme used by Gadget-3. To avoid 'collisions' of particles with singular contributions, the potentials are additionally *softened* to a characteristic scale  $r_s$ . Once the forces calculated, particles are advanced a time step via the *KDK-Leapfrog* integration scheme, which makes use of half-timesteps to ensure symplectic integration. A number of sophisticated algorithms, e.g. adaptive timesteps further improve efficiency to allow for large volumes.

## 2.5 Hydrodynamics

In addition to purely gravitational forces, baryonic particles also experience hydrodynamical forces. As the modelling of the gravity already involves a discretization of mass into individual fluid parcels, the Lagrangian *SPH* method is used. Here the gas continuum is once again discretized into fluid parcels or 'particles', whose hydrodynamical interaction is calculated from the continuum by smoothing particles over a characteristic length scale  $r_{hsm1}$  via a kernel function. We will see an example for this, when reconstructing the continuum in order to obtain the accretion fields in chapter 4. In contrast to dm particles, the baryonic component is discretized unevenly, with  $r_{hsm1}$  dependent on the local density, resulting also in particles of different masses.

## 2.6 Sub-grid models

Baryonic gas can cool radiatively and consequently form stars, which in turn provide pressure feedback via the various supernova explosion channels and enrich the gases present, altering e.g. their X-ray properties. Furthermore they can experience energy injection from AGN, which are present in most galaxies. These feedback effects can significantly alter the dynamics of objects up to galaxy cluster scale (Heinrich et al., 2021) and must therefore be considered. Modern cosmological simulations treat these effects in so-called *sub-grid models*, as they take place on scales far smaller than individual gas particles. The *Magneticum* suite applies sub-grid models for cooling and subsequent star formation (Springel & Hernquist, 2003), chemical enrichment from the stellar populations (Tornatore et al., 2007), (Dolag et al., 2017) and black hole feedback (Hirschmann et al., 2014) among others to model the sub-grid behaviour of baryonic gas as realistically as possible.

## 2.7 Subfind

Our later analysis involves the outskirts of haloes that are identified by the on-the-fly structure finding algorithm SUBFIND (Springel et al., 2001). For identifying haloes this code employs

a *Friends-of-friends* (FOF) algorithm. This algorithm groups dm particles with a distance smaller than a characteristic linking length  $b$ . The name indicates the transitivity of the grouping: If particle A is within one linking length of particle B and particle C is within one linking length of particle B, they all are part of the same group. With an appropriate choice of linking length (usually  $b = 0.2$  times a cosmology dependent factor (Dolag et al., 2009)) and a minimal number of particles criterion, one finds realistic virialized objects this way. SUBFIND also employs a saddle-point finding algorithm on the smoothed FOF density field in order to identify substructures within the FOF groups. For the scope of this thesis however, we are only considering **central** haloes.

## 2.8 Boxes

The *Magneticum* suite of simulations offers up a variety of simulated volumes with different resolutions plus a set of 15 simulations where the cosmological parameters within  $\Lambda$ CDM have been varied. The fiducial cosmology uses the *WMAP7* parameters (Komatsu et al., 2011). Below, Table 2.1 provides an overview of the boxes used in this thesis with the most important properties listed:

Box	run	$\Omega_0$	$\Omega_b$	$\sigma_8$	$H_0$	$f_b$	$L_{box}[\text{Mpc}/h]$	$N_p$	res
1a	C1	0.153	0.0408	0.614	66.6	0.267	896	$2 * 1512^3$	mr
	C2	0.189	0.0455	0.697	70.3	0.241			
	C3	0.200	0.0415	0.850	73.0	0.208			
	C4	0.204	0.0437	0.739	68.9	0.214			
	C5	0.222	0.0421	0.793	67.6	0.190			
	C6	0.232	0.413	0.687	67.0	0.178			
	C7	0.268	0.0449	0.721	69.9	0.168			
	C8	0.272	0.0456	0.809	70.4	0.168			
	C9	0.301	0.0460	0.824	70.7	0.153			
	C10	0.304	0.0504	0.886	74.0	0.166			
	C11	0.342	0.0462	0.834	70.8	0.135			
	C12	0.363	0.0490	0.884	72.9	0.135			
	C13	0.400	0.0485	0.650	67.5	0.121			
	C14	0.406	0.0466	0.867	71.2	0.115			
	C15	0.428	0.0492	0.830	73.2	0.115			
2b	-						640	$2 * 2880^3$	hr
2	-	0.272	0.0456	0.809	70.4	0.168	352	$2 * 1584^3$	hr
4	-						48	$2 * 576^3$	uhr

**Table 2.1:** The Simulation boxes used in this thesis. Parameters from (Dolag, 2022)

## 2.9 Outside the box: Summing up

We have seen how cosmological simulations with hydrodynamics can model the physical processes of both dark matter and baryons efficiently. An overview on the modelling of

background cosmology, gravity, hydrodynamics, sub-grid feedback, enrichment and structure finding was provided specifically for the *Magneticum* suite of simulations. A selection of boxes and runs within this suite was introduced with their respective specifications. In the next chapters we shall put these boxes to good use to learn about the physics between the cosmological scales.



# Chapter 3

## The Emergence of Large-Scale Structure

The rich structure we can observe in our universe today originated from the tiniest of perturbations in the primordial matter density field. A relic of the quantum fluctuations (Mukhanov, 2005) in the inflationary stages of the universe, these perturbations and their evolution have shaped our understanding of the geometry and contents of our universe significantly. The aforementioned discovery of the CMB in the mid-1960s (Penzias & Wilson, 1965) provided us with direct access to these perturbations by measuring a nearly homogeneous background of microwave radiation from the time at which photons could first escape the hot plasma filling the universe *tr.ec*. The perturbations in this background have since been measured to great precision (Planck Collaboration, 2020) and provide valuable insights about the early configuration of density fluctuations in the universe. Our goal for this chapter is to develop some intuition for how the structures that are going to feature heavily in the following chapters (i.e. filaments, galaxy clusters and galaxies) come to be and evolve from these initial perturbations. It is naturally not going to be an exhaustive review of the incredibly rich and diverse field of cosmic structure formation, but I aim to give an overview on where the pure theory can take us and where simulations have to step in. Furthermore there is a set of parameters ( $\delta, \sigma^2, D, \delta_c$ ) in structure formation, that will be integral to understanding the theoretical model for the mass accretion rate of haloes implemented in the next chapter, so I hope to physically motivate those parameters and with them the model.

### 3.1 The Primordial Gaussian Field

The initial conditions of the post-recombination epoch that emerge from inflationary theory and the radiation dominated era are mathematically described by Gaussian random fields (e.g.: Mukhanov, 2005). This means that an arbitrary sampling of  $N$  points  $\zeta = \{\delta_1, \delta_2, \dots, \delta_N\}$  in the overdensity field ( $\delta(\mathbf{x}) = \frac{\rho(\mathbf{x}) - \bar{\rho}}{\bar{\rho}}$ ) will be distributed according to the multivariate Gaussian distribution

$$p(\zeta) = \frac{\exp(-\frac{1}{2}\zeta^i M^{-1}_{ij} \zeta^j)}{\sqrt{(2\pi)^N \det M}} \quad (3.1)$$

where  $M_{ij} = \langle \delta_i, \delta_j \rangle$  is the covariance matrix of the field samplings (using Einsteins sum convention). This is because the probabilities are pairwise independent and individually Gauss distributed at each point. Equation 3.1 illustrates an important property of Gaussian fields: They are completely characterised by their second moment, the *two-point correlation function* defined by

$$\xi(|\mathbf{x}_i - \mathbf{x}_j|) = \langle \delta_i, \delta_j \rangle \quad (3.2)$$

where it has been assumed, that the random field additionally fulfils ergodicity in order to seamlessly switch from ensemble averages to spatial averages. In other words, the spatial correlations ( $\xi$ ) have to decay quickly enough as a function of separation  $r$  to maintain statistical independence between separate volumes, since we have been handed only one universe and thus would struggle to compute ensemble averages. An important quantity is given by the diagonal terms of the matrix:

$$\sigma^2 = \xi(|\mathbf{x}_i - \mathbf{x}_i|) = \xi(0) = \langle \delta_i \delta_i \rangle, \quad (3.3)$$

the variance of the density field, providing a measure for the amplitude of fluctuations. Another function sufficient for the specification of a Gaussian random field is the *power spectrum*  $P(k)$ , the Fourier transform of the correlation function, expressing the relative weight of modes with scale  $\lambda = \frac{2\pi}{k}$ . This is commonly assumed to have a power-law shape (e.g. Harrison (1970))

$$P(k) = Ak^n \quad (3.4)$$

where  $n$  defines the tilt of the power spectrum. In the linear regime the velocity and potential fields  $\mathbf{v}(\mathbf{x})$  and  $\Phi(x)$  are connected to the density field by simple equations (we will write them down below). Applying these, one finds that those fields are also Gaussian random fields. The importance of this property cannot be stressed enough, it will be the basis of many of the theoretical considerations in the following chapters. An interesting first consequence is the relationship between the power spectra of these fields, namely:

$$P_\delta(k) \propto P_{\mathbf{v}(k)} k^{-2} \propto P_\Phi k^{-4} \quad (3.5)$$

The powers of  $k$  arise due to the order of spatial derivatives present in the linear equations connecting the perturbations Equation 3.8. According to this relation the perturbations in the three parameters are tilted towards different scales, with the density perturbations most sensitive to the smallest scales and the potential perturbations most sensitive to the largest scales. An especially simple realization of a density perturbation field is one with  $n = 1$ , the so-called *Harrison-Zel'dovich Approximation* Harrison (1970). Its ideation precedes the idea of inflation, which predicts a spectral index close to 1 (Mukhanov, 2005), by over a decade and was motivated by the observed large scale structure to be later justified by inflation. Considering Equation 3.5 it can be seen that in this case

$$P_\Phi \propto k^{-3}. \quad (3.6)$$

It then follows that the variance of the potential, or its two-point correlation function at scale 0

$$\sigma_{\Phi}^2(k) \propto \iiint d^3k P_{\Phi}(k) = \iiint d^3k k^{-3} \propto \int \frac{dk}{k} = \int d \log(k) \times 1 \quad (3.7)$$

or in other words the potential fluctuation per logarithmic bin is constant in  $k$ . The most precise measurements of this power spectrum demonstrate only a slight red-tilt away from this idealized case:  $n_s = 0.9665 \pm 0.0038$  (Planck Collaboration, 2020), so this convenient spectrum is a very reasonable assumption for first-order estimates. After having specified the most important properties of the initial density fields, we can now let them evolve under gravity:

## 3.2 Linear Theory

If the energy density of the universe were entirely homogeneous, the gravitational field would also be. In such a universe, gravity would isotropically act against the dark energy component and slow down expansion. In the concordance model that would mean an eventual total dilution of the contents of the universe and increasingly accelerated expansion. The previously discussed minute density fluctuations save us from this boring reality in which we would have never come to be: Local differences in gravity due to local density fluctuations lead to locally reduced expansion and a thus a slight deviation from the Hubble flow. This in turn enhances the local overdensity (albeit in the beginning by not diluting as quickly as surroundings), in turn slowing down expansion even further, entering a feedback loop. Once a certain critical threshold is reached, the overdensity completely decouples from the Hubble flow and begins to collapse, eventually forming the astrophysical objects we can observe today. As the rich get richer, so do the poor get poorer: Initial underdense regions begin to expand *above* the mean expansion rate, in turn emptying out even further, ending up in the inverse feedback loop to the overdensities. In the following I will outline the mathematical formalism that describes this evolution to first order. The general structure is inspired by van de Weygaert (2018), which provided a very helpful and extensive overview for this formalism.

**Fluid equations** It is possible to completely write down the equations governing the developments described above. They are the **(inviscous) fluid equations** in co-moving coordinates

$$\frac{\partial \delta_i}{\partial t} = -\frac{(1+w_i)}{a} \nabla \cdot (1+\delta_i) \mathbf{v} \quad (\text{Continuity}) \quad (3.8a)$$

$$\frac{\partial \mathbf{v}}{\partial t} = -\frac{(\mathbf{v} \cdot \nabla) \mathbf{v}}{a} - \frac{\dot{a} \mathbf{v}}{a} - \frac{\nabla \phi}{a} \quad (\text{Euler Equation}) \quad (3.8b)$$

$$\nabla^2 \phi = 4\pi G a^2 (1+3w_i) \bar{\rho}_i \delta^i \quad (\text{Poisson Equation}) \quad (3.8c)$$

Where  $i$  denotes the  $i$ -th component (in  $\Lambda$ CDM  $i \in \{m, r, \Lambda\}$ ) and  $w_i$  represents the parametrization of the equation of state for each component ( $p_i = w_i \rho_i$ ). As we mainly

consider pressureless dark matter in the following we are going to drop the pressure terms containing  $w_i$  eventually. In Equation 3.8  $\mathbf{v}$  and  $\phi$  are the peculiar velocity and the potential perturbation i.e. those are already perturbative quantities with the backgrounds ( $\dot{a}\mathbf{x}$ , the Hubble flow and  $1/2a\ddot{a}x^2$ , the background potential) already subtracted. In the early stages (and later on large scales as we shall see), the perturbations  $\delta$ ,  $\mathbf{v}$ ,  $\phi$  are small, so the terms of second order can be ignored. Once they have grown to  $\delta \approx 1$ , this linear approximation is no longer valid and structures enter the non-linear regime. For now we will continue with the **linearized fluid equations** and drop the non-linear terms in Equation 3.8.

$$\frac{\partial \delta_i}{\partial t} = -\frac{(1+w_i)}{a} \nabla \cdot \mathbf{v} \quad (\text{Continuity}) \quad (3.9a)$$

$$\frac{\partial \mathbf{v}}{\partial t} = -\frac{\dot{a}\mathbf{v}}{a} - \frac{\nabla \phi}{a} \quad (\text{Euler Equation}) \quad (3.9b)$$

$$\nabla^2 \phi = 4\pi G a^2 (1+3w_i) \bar{\rho}_i \delta^i \quad (\text{Poisson Equation}) \quad (3.9c)$$

One of the most convenient simplifications linear theory brings can be seen by decomposing the perturbations into their Fourier modes:

$$[\delta, \mathbf{v}, \phi](\mathbf{x}) = \int \frac{d\mathbf{k}}{2\pi} [\delta, \mathbf{v}, \phi](\mathbf{k}) e^{-i\mathbf{k}\mathbf{x}} \quad (3.10)$$

Inserting into Equation 3.9a, Equation 3.9b, Equation 3.9c it becomes apparent, that the modes do not mix in the linear regime, i.e. modes behave independently! It can also immediately be seen how, once the linear regime is left, the non-linear terms (e.g.:  $(\mathbf{v} \cdot \nabla)\mathbf{v}$ ) mix the modes, transferring power between the scales and complicating the analysis significantly.

**Linear perturbations of dark matter during matter domination** One of the easiest concrete cases we can apply the apparatus developed above to is the linear evolution of dark matter perturbations during the era from  $z_{eq} = 3411$  (Planck Collaboration, 2020) onwards when matter starts to dominate over radiation due to the relative decay of density  $\frac{\Omega_r(a)}{\Omega_m(a)} \propto \frac{1}{a}$  and dark energy is still subdominant, so the only fluid component to consider is matter. During these early times the assumption of linearity is also most robust, because the density contrast has not grown much at all scales. Since the matter component is dominated by the (at least in the concordance model) pressureless dark matter component, the pressure terms in the continuity and Poisson equations (Equation 3.9a, Equation 3.9c) can also be neglected, leaving us with strongly simplified versions of the linearized equations:

$$\frac{\partial \delta_{dm}}{\partial t} = -\frac{1}{a} \nabla \cdot \mathbf{v} \quad (\text{Continuity}) \quad (3.11a)$$

$$\frac{\partial \mathbf{v}}{\partial t} = -\frac{\dot{a}\mathbf{v}}{a} - \frac{\nabla \phi}{a} \quad (\text{Euler Equation}) \quad (3.11b)$$

$$\nabla^2 \phi = 4\pi G a^2 \bar{\rho}_{dm} \delta_{dm} \quad (\text{Poisson Equation}) \quad (3.11c)$$

Taking the divergence of the Euler equation and combining it with the Poisson and the continuity equation leads to a second order differential equation in time:

$$\frac{\partial^2 \delta}{\partial t^2} = \frac{3}{2} \Omega_0 a^{-3} H_0^2 \delta - 2H(t) \frac{\partial \delta}{\partial t} \quad (3.12)$$

This gives us a lot of information already: Since the only derivatives in Equation 3.12 are w.r.t. time, the density perturbations can be expressed with the time dependent and the position dependent part separated:  $\delta(\mathbf{x}, t) = D(t) * f(\mathbf{x})$ . So the spatial configuration of the density perturbations remains exactly the same (n.b.: in co-moving space) and the contrast grows at every point in space at the same rate in linear theory! Furthermore due to the order of the PDE, there are two solutions  $\delta_+$  and  $\delta_-$  so that the general solution can be written as a linear combination of the two parts  $\delta = \delta_+ + \delta_-$ . The growth/decay rate of the density contrast is governed by Equation 3.12 and therefore depends on the time dependence of the scale factor, which in turn is determined by the background cosmology.

**Linear density evolution EDS universe** To go all the way in at least one special case, we can now solve Equation 3.12 for the simplest case that still retains some degree of realism for the epoch we are considering: The Einstein-de-Sitter universe is a flat FLRW universe with only a matter component ( $\Omega_0 = 1$ ). In this case the Friedmann equations for the evolution of the scale factor give us

$$a(t) = \left(\frac{3}{2} H_0 t\right)^{\frac{2}{3}} \quad (3.13)$$

Putting this into Equation 3.12 gives

$$\frac{\partial^2 \delta}{\partial t^2} = \frac{2}{3t} \delta - \frac{4}{3t} \frac{\partial \delta}{\partial t} \quad (3.14)$$

This looks like a power law differential equation and is indeed solved by:

$$\delta(t) \propto t^{\frac{2}{3}} f(\mathbf{x}) + t^{-1} f(\mathbf{x}) \quad (3.15)$$

which explains why we named the two solutions with superscripts + and -: There is a growing mode and a decaying mode in the evolution of the density contrast. With this solution it is now possible to estimate the density contrast of a given perturbation to linear order. However this estimate will only not be way off mark during the very early stages of structure formation, if we want a more realistic description, we have to leave the cozy simplicity of linear theory.

### 3.3 Beyond Linear Theory: Press-Schechter

The large scale astrophysicists' way to handle the fact that linear theory fails once overdensities grow enough to collapse is to simply cut off our ignorance of what happens afterwards and

count these regions as collapsed objects. A simple but very successful formalism was developed by Press and Schechter in the 70s (Press & Schechter, 1974):

### 3.3.1 Roughly counting: Press-Schechter Formalism

The approach of Press and Schechter is as follows: We have a Gaussian random field that evolves with the linear equation ( $\delta(t, \mathbf{x}) \propto D(t)\delta(t_i, \mathbf{x})$ ). Once a region reaches a certain overdensity  $\delta_c$  (a little more on that later) it starts to collapse and eventually form what we would call a halo. What is now the Mass of this object? One idea is to smooth our initial density field by convolving with a spatial filter (usually the spatial spherical top hat filter  $W(\mathbf{x}, R) = \frac{3}{4\pi R^3}\Theta(R - r)$ ). In other words we "take the average" inside a filter volume, ironing out all smaller fluctuations. This gives the fluctuations at scale  $R$ , which can be easily associated with a mass  $M$ , given by multiplying the mean density with the volume of the filter, for the spherical top hat  $M = \frac{4\pi}{3}\bar{\rho}R^3$ . Conveniently this smoothed field at mass scale  $\delta_M$  will still be a Gaussian random field, at least when convolving with the top-hat or Gaussian filter. The quantities defined in section 3.1 will have their corresponding partners for these smoothed fields. Most importantly, the variance of the smoothed field is defined as

$$\sigma_R^2 = \sigma_{M(R)}^2 = \langle \delta_R \delta_R \rangle \quad (3.16)$$

The conserved gaussianity also implies that the likelihood of the density smoothed at mass  $M$  exceeding the critical value in a single point is given by the univariate Gaussian distribution (compare Equation 3.1):

$$P(\delta_M > \delta_c)(x) \propto \int_{\delta_c}^{\infty} \frac{e^{-\frac{\delta_M^2}{2\sigma_M^2}}}{\sqrt{2\pi\sigma_M^2}} \quad (3.17)$$

. The central postulate of Press-Schechter (PS in the following) theory is that this probability is exactly equal to the fraction of the total mass in the universe that has collapsed to haloes with mass  $> M$ . It should be noted that everything here is a function of time, so both sides of the equation will evolve, as the density contrast grows according to linear theory. From this basic assumption the following mass function can be derived (Press & Schechter, 1974):

$$\frac{dn}{d\ln(M)}(M, z)dM = \sqrt{\frac{2}{\pi}} \frac{\delta_c(z)}{\bar{\rho} \sigma^2 M} e^{-\frac{\delta_c^2(z)}{2\sigma^2(M)}} d\sigma \quad (3.18)$$

It marked an important milestone in our understanding of cosmic structure and can make surprisingly good predictions to this day. Taking this equality to the extreme however, a paradox arises: Setting  $M \rightarrow 0$ ,  $\sigma_M$  diverges and the integral in Equation 3.17 evaluates to 1/2. So according to the PS formalism only 1/2 of all mass is contained in haloes. This was initially fixed by introducing a "fudge factor" of 2. To find out why, we have to extend our PS formalism.

### 3.3.2 A little less roughly counting: Excursion Set theory and Extended Press-Schechter

To understand the logic behind the formalism we will lay out in this section, it is a good idea to first get an intuitive understanding for why the PS-way was off by a factor of  $1/2$ : From the Gaussianity of the density field, we can immediately infer that the likelihood of an underdensity is exactly equal to that of an overdensity, in other words  $P(\delta < 0) = P(\delta > 0) = 1/2$ . So with the fudge factor in the PS formalism, we take into account that the mass initially in underdensities will either eventually also condense into (arbitrarily small) haloes or might even be part of an initial overdensity at a larger scale and thus end up inside a halo anyway.

Bond et al. (1991) developed an elegant formalism expanding on the PS ideas, but also capable of accounting for all the mass without introducing heuristic factors. Its foundation is laid by the concepts of **Excursion Set Theory**, a branch of probability theory concerned with the likelihood of a stochastic process (e.g. a random walk) performing an excursion, i.e. crossing above or below a certain threshold. In our case that threshold is given by the critical density. The general idea of this formalism is the following: Consider an infinitesimal mass element  $\delta m$  at some point  $\mathbf{x}_{\delta m}$  in space. To find the largest possible structure this mass element is a member of, we can once again use the idea of smoothing the density field at a scale  $R$ : Starting at  $R = \infty$ , the field  $\delta_R(\mathbf{x}_{\delta m})$  is 0 as the density in the infinitely extended filter is the mean density of the universe by definition. As we decrease our filter radius the smoothed overdensity for our mass element will deviate from 0. At some scale  $R_1$  (this can be arbitrarily small) the smoothed density will exceed the critical threshold, in other words at this scale a halo of mass  $M_1$  will eventually collapse and  $\delta m$  will be a part of this halo. If we now track and plot the value of the smoothed density field  $\delta(\mathbf{x}_{\delta m})$  we will see a trajectory similar to the one shown in Figure 3.1. Here the smoothing radius has been substituted for the variance  $S = \sigma_R^2$ , which in the relevant cases is a monotonically decreasing function of  $R$ , so increasing  $S$  means decreasing  $R$  (Bond et al., 1991). This trajectory resembles a single realization of a random walk. In fact it can be shown (Maggiore & Riotto, 2010) that if we switch the filter from a spherical top hat function to a sharp  $k$ -space filter  $W(k) = \begin{cases} 1 & k < k_c \\ 0 & \text{elsewhere} \end{cases}$  due to the uncorrelated random phases of the modes in a Gaussian random field, this is a Brownian (or Markovian) random walk with statistically independent steps. In this picture then, the fraction of mass in haloes with  $m > M$  is given by the fraction of all trajectories that lie above the critical threshold. These probabilities are relatively easy to calculate due to the Brownian nature of the trajectories and the Gaussian nature of the underlying density field. The keen eyed reader might have noticed, that this is PS all over again. Indeed, all we have done so far is to formalize PS within the framework of excursion set theory. This has gained us a new viewing angle on the fudge factor issue: What PS fails to capture are the trajectories that up-cross the threshold at some  $S_1$  and then down-cross it again at some  $S_2 > S_1$ . If you would probe a mass element with such a trajectory at a scale  $S_3 > S_2$  you would come to

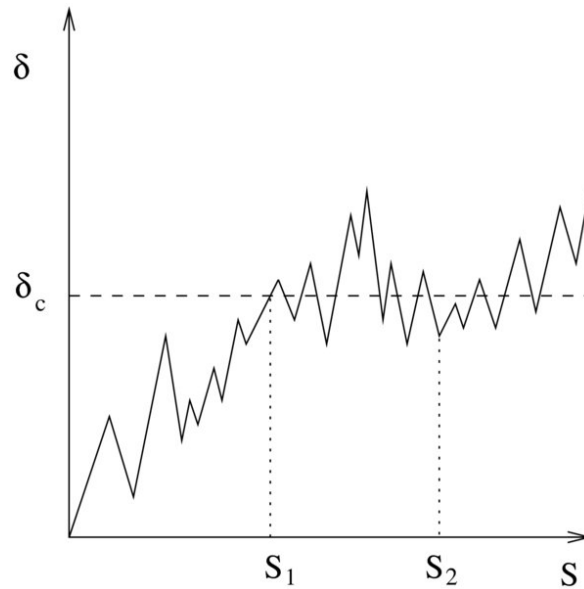


**Figure 3.1:** Single trajectory in  $\delta - S$  space. Figure 3 from Maggiore & Riotto (2010)

the conclusion that it is not contained in a halo with mass  $m > M_3$ . However between  $S_1$  and  $S_2$  the trajectory *does* exceed the threshold, so the mass element must be contained in a halo with mass  $m > M_1 > M_3$ , which is clearly contradictory. With the added tools of the Excursion Set framework it now becomes much clearer, how to mitigate the issue: We simply need to account for those missed trajectories somehow. Here a realization is useful: Each of these "problematic" trajectories has a dual that can be constructed by mirroring its course around the threshold starting at the point of first crossing. Since the original curve is below the threshold at the scale  $S_3$  where we initially missed it, the mirrored curve is guaranteed to be above it. Furthermore the Markovian nature of the walk ensures that all trajectories have the same probability. So we can simply count each curve that can be found above the threshold twice and will automatically have accounted for its mirror curve we are blind to at the given resolution due to it down-crossing again at a higher  $S$ . This is then the justification

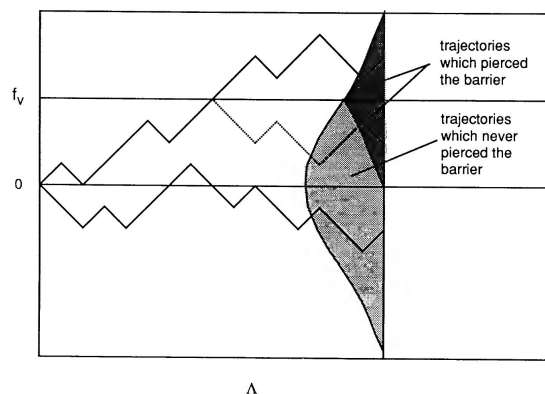


**Figure 3.2:** Figure 4 from Bond et al. (1991) demonstrating the distribution of trajectories that need to be considered. The black tail of the Gauss curve marks all trajectories that are above the threshold at the scale  $S$  of evaluation plus all trajectories that crossed earlier, but down-crossed again before  $S$ .

for the ad-hoc factor introduced by Press and Schechter. By calculating the mass fraction in a mass range  $m > M$  as the fraction of trajectories that had their *first* up-crossing at any

$m > M$ , the EPS formalism arrives at exactly the same result, namely the same halo mass distribution function, but it has the big advantage that it does so self-consistently. Still we add additional problems by now losing a solid definition of the filter mass, a flaw that was already recognized by Bond during the conception of the formalism (Bond et al., 1991). Haloes tend to not be infinitely extended sinc-like density wave packets (the Fourier transform of the sharp k-space filter). There are statistical remedies to this that involve computing the non-Brownian random walks a spatial top-hat gives with Monte Carlo techniques (Bond et al., 1991), but the standard approach is to just ignore this problem and use the spherical top hat filter mass for a sharp k-space filter, inevitably introducing inaccuracies. Still on EPS' shoulders rests the method developed by van den Bosch (2002), which will be centrally featured in my numerical analysis in the next chapter.

### 3.3.3 A hierarchy of clumps: From clusters to galaxies – or vice versa?

As in the next chapter we move on from the frozen-in-time  $\delta, S$  picture of EST to a temporal evolution we should take the time for a short intermezzo on – well, time. We can introduce dynamics to the picture of a single EPS trajectory by remembering that in the linear stage, all modes grow independently from each other. So for the single trajectory in Figure 3.1 this means that as time progresses from  $z_1$  to  $z_1 + dz$  the trajectory is simply lifted upwards by a factor of  $\frac{D(z_1+dz)}{D(z)}$  at every  $S$  (as long as we don't put too much value into what happens beyond  $\delta_c$ ). This can equivalently be viewed as the threshold being lowered, while the trajectory remains constant, sampling lower and lower parts of the curve above the critical density and into collapse. So there will be a natural hierarchy of collapse in the sense that modes with initially higher perturbation amplitude will collapse earlier than perturbation modes with lower initial amplitude. What this hierarchy looks like, depends on the cosmological model, mainly on the shape of the power spectrum Equation 3.4. In the standard cosmological model with  $n = 1$  or very nearly so, the power spectrum is in general tilted towards lower scales (remember that increasing  $k$  means decreasing spatial wavelength). So we expect a *bottom-up* collapse scenario with matter clumping first on smaller scales and large scales forming at later times. This is where the picture of a *Merger Tree* comes from, an example of such a tree constructed from a numerical simulation is shown in Figure 3.3. It shows how the final halo at  $z = 0$  is assembled step-by-step from smaller haloes which have formed first. A **top-down** scenario would produce dramatically different merger trees with the large haloes forming first and then fragmenting increasingly into smaller objects. As we will see in the next section, the idea of a merger tree is woven into the van den Bosch (2002) model, especially in the way, the actual algorithm is set up.

### 3.3.4 The Mass accretion history of dark matter haloes

The van den Bosch (2002) model for Mass Accretion Histories (MAH from now on) basically aims to reconstruct the merger trees discussed before from the statistics of the density field. Because in the EPS formalism all mass is contained in some collapsed structure, that may

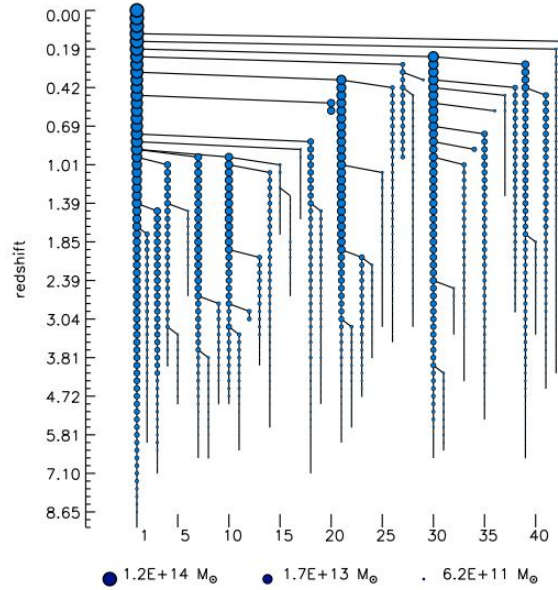


**Figure 3.3:** Example of a merger tree from a cosmological simulation. Only the most massive 42 branches are shown, with the x-labels indicating the branch number, redshift on the y-axis (decreasing in the positive y-direction) and the icon size indicating the mass at a given redshift. Figure 10 from Tweed et al. (2009).

be arbitrarily small, this accounts for both smooth accretion and proper mergers with similar masses. The central idea of the model is built on the fraction of trajectories with their first up-crossing in  $S, S + dS$  :

$$f(\delta_c, S)dS \propto \frac{\delta_c}{S^{3/2}} e^{-\frac{\delta_c^2}{2S}} dS \quad (3.19)$$

To extract an assembly history from the EPS formalism the first question one has to ask is: What is the conditional probability that a mass element contained in a halo of mass  $M_1$  at the present time was in a halo of mass  $M_2$  at some earlier time? This represents one step into the past on the merger tree from the present time. One can already guess that to trace the history of a halo back in time we have to ask this question again and again going back in time until we have achieved a sensible degree of fragmentation. Translating the question above to the language of Excursion Set Theory, what we are looking for is the conditional probability of a mass element having had its first up-crossing at a scale  $S_2$  with a critical density of  $\delta_c(z_2)$  given that it had its first up-crossing at a scale  $S_1$  at a lower redshift  $z_1$  and critical density  $\delta_c(z_1)$  (as before the linear increase of density contrast is described by a corresponding lowering of  $\delta_c$ ). But this is simply the probability that a trajectory starting at  $(S_1, \delta_c(z_1))$  has its first up-crossing of the barrier  $\delta_c z_2$  at  $S_2$ ! This is given by Equation 3.19:

$$P(\delta_c(z_2), S_2 | \delta_c(z_1), S_1) = f(\delta_c(z_2) - \delta_c(z_1), S_2 - S_1) \quad (3.20)$$

A merger tree for an object of mass  $M_0$  can then be reversely constructed by repeatedly drawing progenitor masses from Equation 3.20 one time step in the past at redshift  $z_1 > z_0$  until the largest progenitor mass is larger or equal to the mass of the initial mass minus the sum of all progenitor masses. At this point the largest mass is taken to be the mass of the

halo at  $z_1$  and the procedure is repeated at  $z_2 > z_1$  et cetera. This amounts to fracturing the "Most Massive Progenitor" (MMP) at each time step according to the statistics of the density field, then finding the 'new' MMP. [van den Bosch \(2002\)](#) now computes the average MAH as a function of present day mass by summing for each  $M_0$  and each time step  $z$  over 1000 realizations of the statistical process outlined above. To obtain the "universal MAH" [van den Bosch \(2002\)](#) then fits these statistically constructed MAHs, resulting in the following form for the universal history  $\langle \Psi \rangle := \frac{M(z, M_0)}{M_0}$ :

$$\log \langle \Psi(M_0, z) \rangle = -0.301 \left[ \frac{\log(1+z)}{\log(1+z_f)} \right]^\nu \quad (3.21)$$

From this I then computed the theoretical mass accretion rate, as suggested by the author:

$$\dot{M}_{th}(M_0, z) = M_0 \frac{d\Psi}{dt} \quad (3.22)$$

. The shape of this accretion rate in mass predicts a completely self-similarity for the mass accretion. We will explore how well this assumption holds against numerical simulations with added baryonic physics in the next chapter. The parameters  $z_f$  and  $\nu$  are fitting parameters, however the author provides a prescription to calculate them from cosmological parameters alone. I followed this prescription to obtain the parameters for the simulation cosmology used.

### 3.3.5 From spherical cows to ellipsoidal ones

So far we haven't physically motivated the threshold parameter  $\delta_c$  and just assumed it to be a constant of some value. In the standard PS and EPS approaches this parameter is derived from the **spherical top hat** collapse model ([Gunn & Gott, 1972](#)). In this simplified model of the non-linear collapse of an overdensity initially co-moving and concentric spherical shells detach from the background expansion at the so-called turnaround time  $t_{ta}$  and collapse completely self-similarly i.e. without any shells crossing until they all reach  $r = 0$  at the same time  $t_{coll}$ .  $\delta_c$  is then the linearly extrapolated density of an initial overdensity at the time it (theoretically) reaches  $r = 0$ . It should be noted that because of the self-similarity of the model, this value does not depend on the initial size of the region. In the spherical top hat model  $\delta_c$  is really a constant. However, as much as there are no spherical cows, there are no spherical top hats in the universe. A second order solution is the ellipsoidal collapse model by [Sheth et al. \(2001\)](#). Adapting the EPS formalism for this collapse model takes the tidal fields correctly into account by implementing a variable density threshold  $\delta_c(e, p)$  with  $e, p$  the initial ellipticity and prolateness. It has been shown to significantly reduce the deviation between EPS models ([Springel, 2004](#)). Unfortunately for such a variable threshold, similar to the case of a spherical top-hat, the nice analytical solutions vanish and one has to resort to statistical methods to calculate the mass function ([Sheth et al., 2001](#)). Still the universe

refuses to be linear and spherical, as will be highlighted even more in the following, so we have little choice but to follow into non-linearity and numerics if we want to be accurate.

### 3.4 The cosmic web

When the results of some of the earliest 3d cosmological N-body simulations were published, a key feature of non-linear structure formation emerged for the first time (Klypin & Shandarin, 1983): From the 2d sheet-like structures at this time already known as "pancakes", which constitute the first large-scale structures to emerge, evolved an intricate network of filaments connecting the largest structures (These simulations were set up on large scales only, using cell-sizes of 5 Mpc Klypin & Shandarin, 1983), with very underdense domains called voids in between. We will come back to these fascinating regions later on, for now we shall be concerned with the matter-rich regions. At this point in time structure formation theory was divided into two disjoint domains (Bond et al., 1996). One was the domain of hierarchical structure formation we have discussed so far, extending from cluster scales to galaxy scales. The other was the theory of super-cluster structure, with its foundation the **Zel'dovich approximation** (Zel'dovich, 1970) for quasi-linear collapse of large scale structures. While the former, as we already saw, was a bottom-up approach the latter is a top-down theory. From it the "pancakes" that were used as initial conditions for simulations like Klypin & Shandarin (1983) arise and it was later found that it had the potential to take us a long way towards a realistic description of non-linear large scale structure termed the **Cosmic Web** (Bond et al., 1996). For this reason I will outline this approximation and its connection to the cosmic web briefly. It is not essential for the work in the upcoming chapter but will become important again, when we dare to gaze into the void.

#### 3.4.1 Approaching the web: The Zel'dovich approximation

So far we have considered fluid dynamics from an **Eulerian** point of view, i.e. formulated the motion of the fluid from the perspective of a fixed point in (co-moving) space. An alternative perspective is the so-called **Lagrangian** view: We label a fluid elements with a certain mass with their initial positions (in the literature often denoted  $\mathbf{q}_i$ ) and follow their trajectories through space. The core statement of the Zel'dovich approximation is a simple connection between Eulerian and Lagrangian coordinates (Zel'dovich, 1970), which can be formulated in terms of co-moving coordinates:

$$\mathbf{x}(\mathbf{q}, t) = \mathbf{q} + D_+(t)\mathbf{s}(\mathbf{q}) \quad (3.23)$$

Here  $\mathbf{s}(\mathbf{q})$ , the initial displacement critically only depends on the initial coordinates and the motion of the fluid element continues along the direction of initial displacement. Furthermore

$$\mathbf{s}(\mathbf{q}) \propto -\nabla\phi_{lin} \quad (3.24)$$

In other words, the displacement vector is directly proportional to the linearly extrapolated gravitational potential. Mass conservation then implies

$$\rho(\mathbf{x}, t) d\mathbf{x} = \bar{\rho}(t) d\mathbf{q} \quad (3.25)$$

leading to

$$\frac{\rho(\mathbf{x}, t)}{\bar{\rho}(t)} = \det\left(\frac{\partial x_i}{\partial q_j}\right)^{-1} \quad (3.26)$$

Expressing this in terms of the Eigenvalues  $\lambda_i$  of the deformation tensor  $-\frac{\partial s_i}{\partial q_j}$  we get from  $\frac{\partial x_i}{\partial q_j} = \delta_{ij} + D_+(i) \frac{\partial s_i}{\partial q_j}$ :

$$\delta(\mathbf{x}, t) + 1 = \frac{1}{(1 - D_+(t)\lambda_1)(1 - D_+(1)\lambda_2)(1 - D_+(t)\lambda_3)} \quad (3.27)$$

From this beautiful result, the general anisotropy of large-scale collapse immediately arises: In general there will be an ordering of the Eigenvalues  $\lambda_1, \lambda_2, \lambda_3$ . This means that the density contrast will grow the fastest along the direction of the eigenvector with the largest corresponding  $\lambda$ , equivalent to the shortest initial axis, forming the "pancake" mentioned earlier. After the collapse along the eigenvector with the second largest eigenvalue, an elongated filament forms, to finally collapse along the third direction to a spherical node. Even though this simple approximation has its shortcomings and must be expanded on by an analysis of the singularities (the simplest example of such a singularity is our pancake) that arise within Lagrangian perturbation theory (Hidding et al., 2014), we can already derive the basic elements of the cosmic web from it. For the scope of this thesis, this shall be enough.

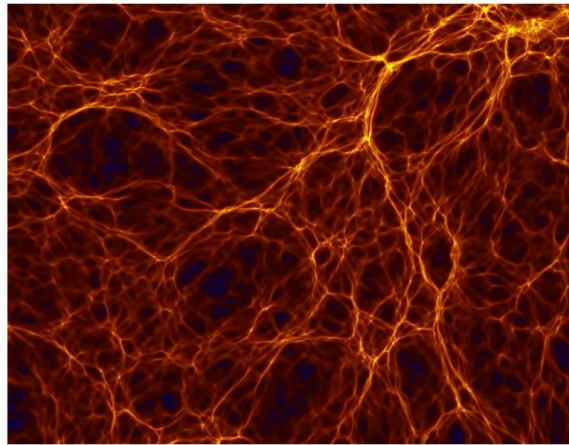


**Figure 3.4:** Density field evolved with Zel'dovich dynamics. The web-like structure is clearly visible. Figure 1 from Hidding et al. (2016)

### 3.5 Not complicated enough: Enter the Baryons

So far we have limited our considerations to dark matter. As the topic of this thesis is precisely the influence of baryons on large scale structure, we cannot leave them out of the picture.

Now for the large scale dynamics of the previous section the impact of baryonic processes is minimal (e.g. Cui & Zhang, 2017), so the picture outlined here is largely unaffected. However for smaller scales and in the highly non-linear environments of collapsed structures, they become increasingly important. A key distinction between dissipationless dark matter and baryonic gas is the ability of gas to form outflows. Up to the point where the combined matter density exceeds the critical density and an object starts to collapse, the baryonic overdensities simply grow along with the dark matter perturbations (for a concise review of pre-in-fall baryonic physics see van den Bosch, 2020 or Kimmig, 2022). Once the overdensity collapses however, as opposed to dark matter, baryons can shed angular momentum by radiative cooling, leading to more condensed cores in the centers of haloes while the dark matter reaches a more extended virial equilibrium configuration.

**Shocks** As the gas falls in on an already virialized overdensity either following a dark matter filament or from a void region, it will at some point encounter gas that has settled to the center and unlike the pressureless dark matter form violent accretion shocks at the boundaries of collapsed haloes (Bertschinger, 1985). These accretion shocks can then combine with shocks from halo mergers to form so-called MA-shocks that can exceed the virial surfaces of these haloes by factors of up to 3 (Zhang et al., 2020). Gas that is heated to extreme temperatures  $T \approx 10^8\text{K}$  at such caustics can undergo adiabatic expansion, forming a hot and out-flowing (or expanding) atmosphere.

**Galactic Feedback** Other channels of energy re-injection for baryons are AGN, capable of driving powerful outflows in galactic haloes (Santoro et al., 2020) and supernova feedback (Nguyen & Thompson, 2022), which is driven by the formation and evolution of stars from cool gas condensing in galactic disks. These feedback mechanisms can also change the chemical composition and observational properties of the gas, as supernovae create high-Z elements with their relative abundances dependent on the explosion channel (Kobayashi et al., 2020) and outflows distribute these elements into the haloes. This makes metallicities a viable tracer for outflows in both simulations and observations.

**Filamentary heating** Another important feature of baryonic physics at the intermediate is heating during filamentary in-fall. Due to shocks at the surface of and within filaments, gas can already be in the warm phase before it gets close to the virial surface of collapsed haloes. The high density in the filament and consequently short cooling time can allow gas in-falling in filaments to penetrate the shocks at cluster boundaries and inject hot gas into the cluster centers, significantly impacting their dynamical states (Zinger et al., 2016).

Overall the added complexity of baryonic physics makes numerical simulations a vital asset if we want to understand the role of gas in the coupling of haloes to large scale structures.

## 3.6 So far from the theorists: Summary

We have followed the process of structure formation from small fluctuations in an initial density field to the complex beauty of the cosmic web. Starting from the simplicity of the linear evolution in the earliest stages of structure formation, we then applied the results of this theory to the hierarchical collapse models such as [Press & Schechter \(1974\)](#). A key concept was the framework of **Excursion Set Theory**, viewing the density field frozen in time and filtered at varying smoothing radii as a trajectory in an abstract plane of  $\delta, S$ . This framework helped us to build our models more self-consistently ([Bond et al., 1991](#)) and was the crucial motivator in our approach to derive semi analytical accretion histories from cosmological parameters alone with the model of [van den Bosch \(2002\)](#). This will be compared to numerical results that include non-linear dynamic in the following chapter. Going up in scale we then explored the emergence of a rich network of filaments and nodes. We found a theoretical foothold in the **Zel'dovich approximation** which helped us gain a first understanding of the organization of matter on the largest of scales. It will be useful once more in the second part of this thesis. Finally we turned to the baryons and briefly reviewed the processes and features we will try to find in the simulated gas maps in the following chapter. The most important imprints of baryonic physics are the shocks that form through accretion and merging in the outskirts of haloes.



# Chapter 4

## Feeding the hungry: The in- and outflows of *Magneticum* haloes

### 4.1 Flowing in the cosmos

As we have seen in the previous chapter given slight perturbations in its earliest stages, the cosmos is all but static, even if the general expansion of space is accounted for. This chapter will be dedicated to the large scale flows that shape (and are shaped by) the developing structures in the universe we can observe today. In the linear regime this connection of flow fields to structures is particularly simple (recall [add cross reference]). From this simple picture it is immediately clear that the evolution of the velocity field must follow the evolution of the density field to first order, albeit the full picture is more complex. To visualize this, we can watch the evolution of the velocity field with redshift: Figure 4.1 shows this evolution for the dark matter component in the 352 Mpc hydrodynamical Box2 from the *Magneticum* suite of simulations. It can be seen how the velocity field traces the formation of the cosmic web. Considering the apparent non-linear nature of the velocity field in most regions of the slice illustrates the argument for the necessity of a numerical approach made in chapter 2 once more. The geometry of the streams leads to an intuitive classification of the different collapse modes mentioned in chapter 3 (albeit in 2d projection): The initial sheet-like structures (2d surfaces) first collapse along their shortest dimension to form the narrow filaments (streamlines converging in every direction but one) which then finally collapse into point symmetry configurations called nodes (streamline convergence points). Voids are effectively anti-nodes with all streamlines leading away from them. They emerge as the darkest and most linear regions in the figure, as they become more and more devoid of matter. We will return to these fascinating environments in chapters 5 and 6.

In Figure 4.1 only the evolution of the dark matter component is shown, which is collisionless in the standard  $\Lambda$ CDM model of the universe. When dark matter particles fall onto an overdensity, they cannot dissipate their energy efficiently, leading to extended dark matter haloes in galaxies and clusters of galaxies. In contrast the baryonic matter components are slowed down rapidly in violent shocks at the borders of collapsed structures, converting part

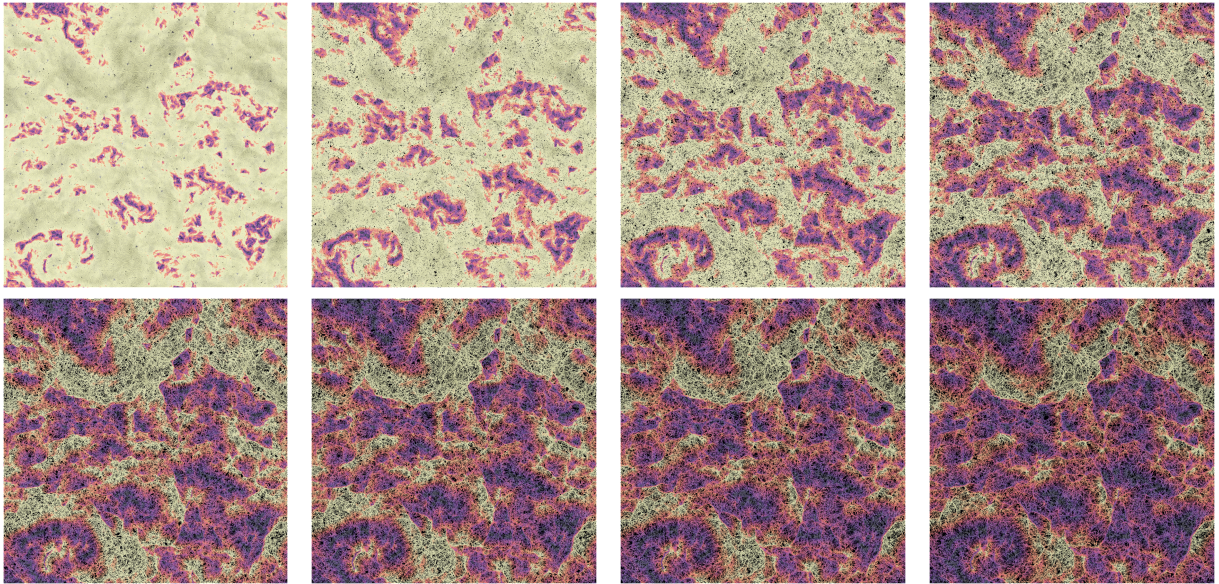


**Figure 4.1:** Evolution of the co-moving velocity field in Box2 *Magneticum*. A thin z-slice through the mid-plane was selected. The heat map shows the magnitude of the co-moving velocities, while the overdrawn streamlines indicate the flow direction. New plots coming up

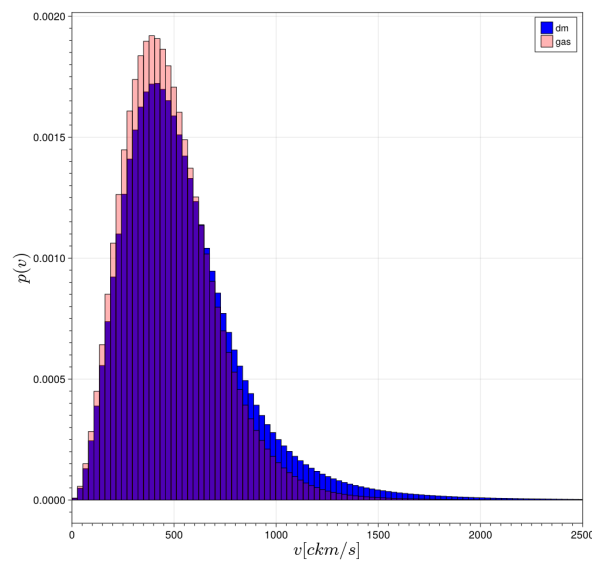


**Figure 4.2:** Histogram of the absolute velocities for the different matter components in *Magneticum*

of their gravitational energy to thermal and ultimately radiative energy. For this reason the gas components tend to be less extended in phase space. The high velocity tail in Figure 4.2 highlights this bigger spread of dark matter. From these two basic examples and from the relations laid out in chapter 3 it is clear that the peculiar velocity field is ripe with information about the formation and evolution of structure. In this chapter we shall make use of this by probing the field on the scales at which the linearity of the Mpc to Gpc velocities and the chaotic non-linearity of already collapsed or collapsing objects like clusters and galaxy filaments meet. Especially the gas will be of interest, since the boundaries of massive objects mark the transition zone where baryonic physics starts to really matter.

## 4.2 To answer a question, you first have to ask it: Goals

It is widely maintained that, while galaxy cluster-scale haloes retain, to a certain degree, the self-similarity of the initial Gaussian perturbations even in the presence of baryonic physics, galaxies break this self-similarity (Böhringer et al., 2012). One of the central questions we will address in this chapter is whether imprints of the initial self-similarity can also be traced by the flow fields in the outskirts of these objects, as well as if and at what scale these imprints might vanish. As the relatively robust scaling laws measured with galaxy clusters allow for a much easier analytical treatment than for galaxies, another closely related question is how well models based on analytical theory like the van den Bosch (2002) universal mass accretion history can trace the actual physical processes happening at the cluster to group boundary scale. This is an important question to consider when comparing these theoretical calculations to observations in particular and might help in shedding light on possible biases and deviations to keep in mind when comparing theory to observation.

The second question is concerned with what goes out: Recently there have been hints at streams of matter entering voids (Vallés-Pérez et al., 2021) (though these inflows would still be heavily outweighed by the general outflow from these regions of course). This begs the question whether it is at all possible for bound structures to push out matter so far that it might unbind and feed the galaxies left behind in the general exodus during the formation of the void. In the standard picture of galaxy evolution these void galaxies are considered the key to improve our understanding of the processes involved in shaping the rich zoo of galaxies we observe today. Their salient feature from an evolutionary perspective is that they can effectively be taken as decoupled from environmental effects. Unbinding outflows from neighbouring structures would be an interesting correction to this picture and necessitate further investigations of these objects. Furthermore the balance of inflows and outflows can be directly linked to the energy budget of the clusters, so a quantification of this balance can potentially provide insight into the dynamical states of these objects.

If present it is also important to consider the mechanisms that might drive such outflows: The supersonic in-fall of material onto a collapsed object like a galaxy cluster creates high Mach-number shocks at their peripheries. When runaway shocks from mergers undergone by the cluster encounter these accretion shocks, they are hypothesized to combine to a long living merger accelerated accretion shock (MA-shock, (Zhang et al., 2020)) that can propagate far outside the virial radius of the cluster, heating the gas it passes through. The expansion of this shock-heated gas could constitute an effective outflow at the cluster boundaries. At the group to galaxy scale other mechanisms become increasingly important. In galaxies, star forming activity triggers type-II supernovae from massive short-lived stars at early times and type-Ia supernovae later on. Both explosion modes generate significantly enriched gas outflows compared to cosmic averages, with the two modes discernible by the amount of iron produced (Kobayashi et al., 2020). Additional outflows might come from AGN jet feedback. Each of these channels creates outflows from gas at a specific processing stage: The gas heated by the shocks in galaxy cluster outskirts has most likely been processed in the in-falling filaments,

supernova driven outflows transport highly enriched gas out of their respective galaxies and AGN driven outflows tend to comprise of the gas that is cold enough to collapse to the central black hole. For this reason, gas temperature and metallicity are excellent tracers of outflow mechanisms at play.[citation needed]

To try and answer the questions outlined above, it is therefore imperative to measure the magnitude of these mass flows as well as their spatial distribution and the properties of the gas that comprises them, which is what we set out to do in this chapter.

### 4.3 Measurements: Setup and parameters

There are a number of different ways and proxy quantities to determine the accretion rate of galaxies and clusters in both simulations and observations (for exemplary methods see X for simulated and Y for observed clusters), but our goal here is to properly reconstruct the flows and *then* obtain an accretion rate from them. Because the simulations used in this work integrate their hydrodynamics with SPH methods, computing the gas (and dark matter) fluid continuum inversely to the SPH discretization is the most self-consistent way to calculate the simulated flows with the required spatial resolution. All post-processing in this section was executed with a modified version of the Map-Making program *SMAC* (Dolag et al., 2005), which provided a basic framework for calculating the fields at spherical shells I then expanded on. Instead of time (effectively spatially) averaging the flow over a spherical shell, in this work I calculate the *instantaneous* flow through the surface with the combined information from the smoothed density and velocity fields. In general this flow is given by

$$\int_V \nabla \cdot \mathbf{F} dv = \oint_{\partial V} \mathbf{F} \cdot \hat{n} da \quad (4.1)$$

integrating either the divergence of the velocity field over a given volume or the normal component over a bounding surface, with the Gaussian theorem connecting the left and right sides of the equation.

#### 4.3.1 Reconstructing the fields

The field contribution of the  $j$ -th particle at the  $i$ -th generalized volume element can be calculated as follows:

$$\alpha_i * f_i * w(|\mathbf{r}_{i,j}|) \quad (4.2)$$

where  $\alpha_i$  is a geometry factor encoding the overlap of the particle with the pixel and  $w(\mathbf{x})$  is the smoothing kernel. In this work I used the three dimensional *cubic spline* kernel:

$$w(\mathbf{r}) = w(r) = \begin{cases} \frac{8}{\pi}(1 - 6r^2(1 - r)) & r \leq 0.5 \\ \frac{16}{\pi}(1 - r)^3 & 0.5 < r \leq 1 \\ 0 & elsewhere \end{cases} \quad (4.3)$$

Cluster ID	$r_{vir} [kpc/h]$	$M_{vir} [10^{10} M_{\odot}/h]$
5	2346.1	113282.0
20	2177.5	90571.7
53	425.3	674.7
384	202.0	72.3

**Table 4.1:** The four "poster child" haloes.

In principle this works for any field and can be done both for voxels and pixels. The fields considered in this work are the density  $\rho$ , the density weighted radial component of the gas velocity  $v_t, v_r$  and the density weighted temperature and metallicity  $T, Z_X$  where  $X$  represents the different gas components (in the Tornatore et al. (2007) model  $X \in \{total, He, C, Ca, O, N, Ne, Mg, S, Si, Fe, > Fe\}$ ).

### Geometry

Because of the tendency of haloes to be spherical on large scales it is reasonable to collect the flow into a sphere centered on the halo. This is done by numerically making use of the r.h.s. of Equation 4.1. A sphere with radius  $r$  is tessellated into surface elements of equal angular dimensions (and thus also area) using the versatile *Healpix*<sup>1</sup> scheme (Gorski et al., 2005). For every surface element  $da$  the normal vector is then, in reasonable approximation, just the radial unit vector at the center of the surface element  $\hat{\mathbf{r}}(\mathbf{x}_{pix})$ . From this the differential flux follows easily:  $d\Phi = \mathbf{F}(\mathbf{x}_{pix}) \cdot \hat{\mathbf{r}}(\mathbf{x}_{pix}) da$ . The mass flow through a single pixel can thus be calculated as:

$$d\dot{M} = \rho(\mathbf{x}_{pix}) \mathbf{v}(\mathbf{x}_{pix}) \cdot \hat{\mathbf{r}}(\mathbf{x}_{pix}) da \quad (4.4)$$

and the accretion or decretion rate  $\dot{M}$  at a given radius  $r$  is the sum over all pixel contributions. Additionally a full-sky map is returned for each of the components at every radial bin. During the course of this chapter  $N_{pix}$  will be 196607.

### Sample

To probe across a wide range in mass I selected a total of 319 *Subfind* halos in 11 bins, 29 haloes per bin. Masses range from  $10^{12} M_{\odot}$  to  $10^{15} M_{\odot}$  covering a spread from very small groups/heavy galaxies to the heaviest clusters in the simulation. The haloes in the mass range of  $10^{12} - 10^{13} M_{\odot}$  are taken from the smaller, higher resolution Box4 (uhr, 68 Mpc side length), while the high-mass range of  $10^{13} - 10^{15} M_{\odot}$  is covered by the larger, less resolved Box2b (hr, 909 Mpc side length), with the  $10^{13} M_{\odot}$  bin present in both boxes. The data in this chapter, unless indicated otherwise, is taken from snap031 (*hr*)/ snap116 (*uhr*), corresponding to a redshift of  $z = 0.25$ . Each halo is sampled at 20 radii in the range  $r \in [1.2, \dots, 5] \times r_{vir}$  for the velocity, density, temperature and metallicity fields. For a more thorough individual analysis I selected four "poster child" haloes, representing dynamically relaxed clusters, dynamically perturbed clusters, heavy groups and galaxy-like objects respectively, as seen in Table 4.1.

<sup>1</sup><http://healpix.sourceforge.net>

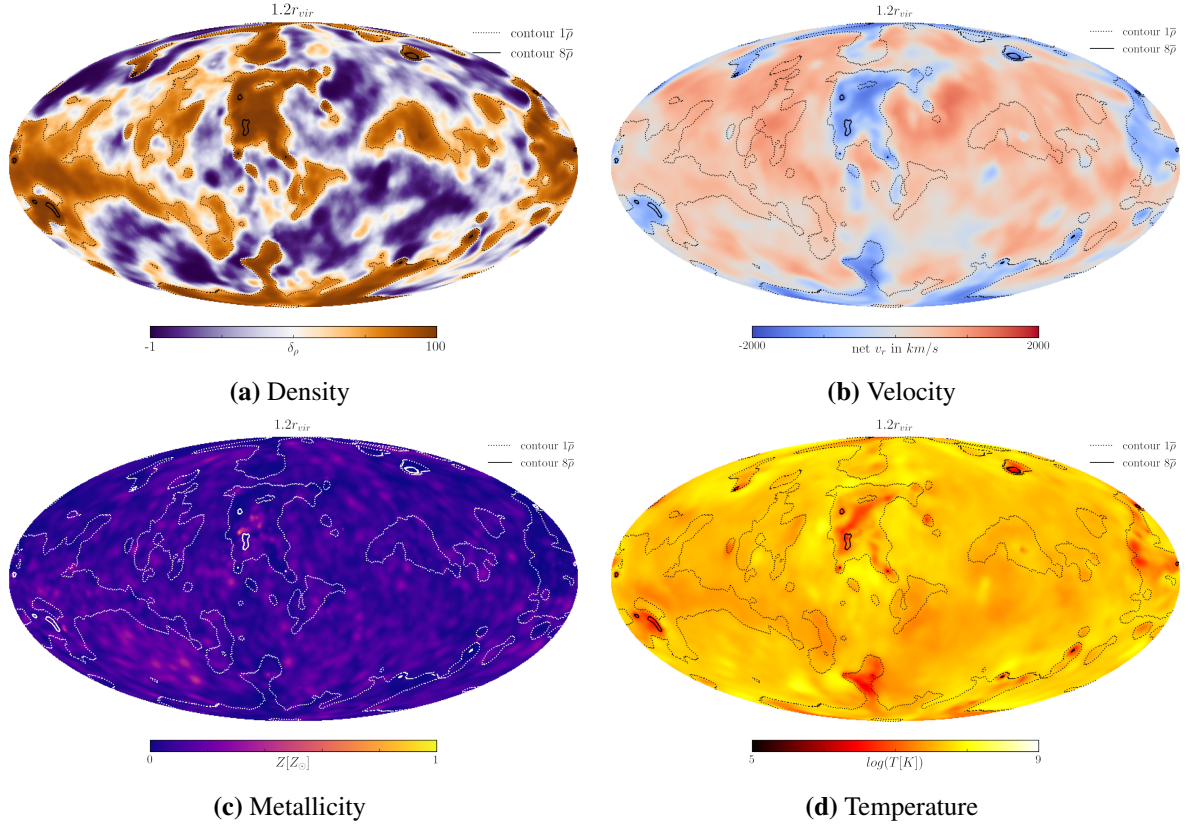
## 4.4 A sky full of flows: The spatial distribution of mass accretion and decretion

Structure formation theory sees accretion onto clusters and groups happen mainly along the directions of the large scale filaments as seen in Figure 4.1 (even though there are possible differences between clusters and groups regarding in-fall symmetry according to studies like (Gouin et al., 2022)). This means that the geometry of these flows is mainly dictated by the peculiar gravity. In contrast, the outflows we could reasonably expect from haloes are driven by distinctly different processes like feedback from the member galaxies and MA-shocks, with the common denominator being, that they are regulated and shaped by the thermodynamical properties of the gas. Therefore one would expect to see a difference also in the spatial distributions of these two modes, with the colder in-flowing gas being more concentrated in the filaments and the hotter out-flowing gas more homogeneously distributed. With the analysis pipeline outlined in the previous section, it is straightforward to verify this from our simulation data, since the calculated healpix maps provide this information in addition to the total flow. This chapter is a detailed case study of the "poster child" sub-sample introduced in Table 4.1.

**Field analysis at a fixed radius** As a first example, we will consider the most massive halo of this subset, cluster 5: Figure 4.3 shows a general agreement with the hypothesis above: While the inflow regions align with the dense filament contours, the outflow regions spare these areas, showing a fairly spherically symmetric distribution otherwise. The temperature map shows that the gas inside the gravity dominated filaments is colder than the outflowing gas, which reaches temperatures above  $10^8 K$ , comparable to the hot gas phase in cluster centers (Gouin et al., 2022). Interestingly the temperature hot spots accumulate in the out-flowing regions just outside the filaments. This is where one would expect to find the accretion shocks generated by the rapid in-fall lending weight to the idea that these shocks, or their interaction with merger shocks to form MA-shocks drive material outwards by heating the cold gas, subsequently inducing adiabatic expansion. Enrichment shows no pronounced preference for in-falling or out-flowing regions and is largely homogeneously distributed, with a few hot spots around pronounced over-densities most likely in-falling haloes within the filaments. This hints at an early enrichment process within the filaments, with the enriched gas then being distributed by the shocks. I will return to this point later to investigate the precise enrichment mechanisms for clusters.

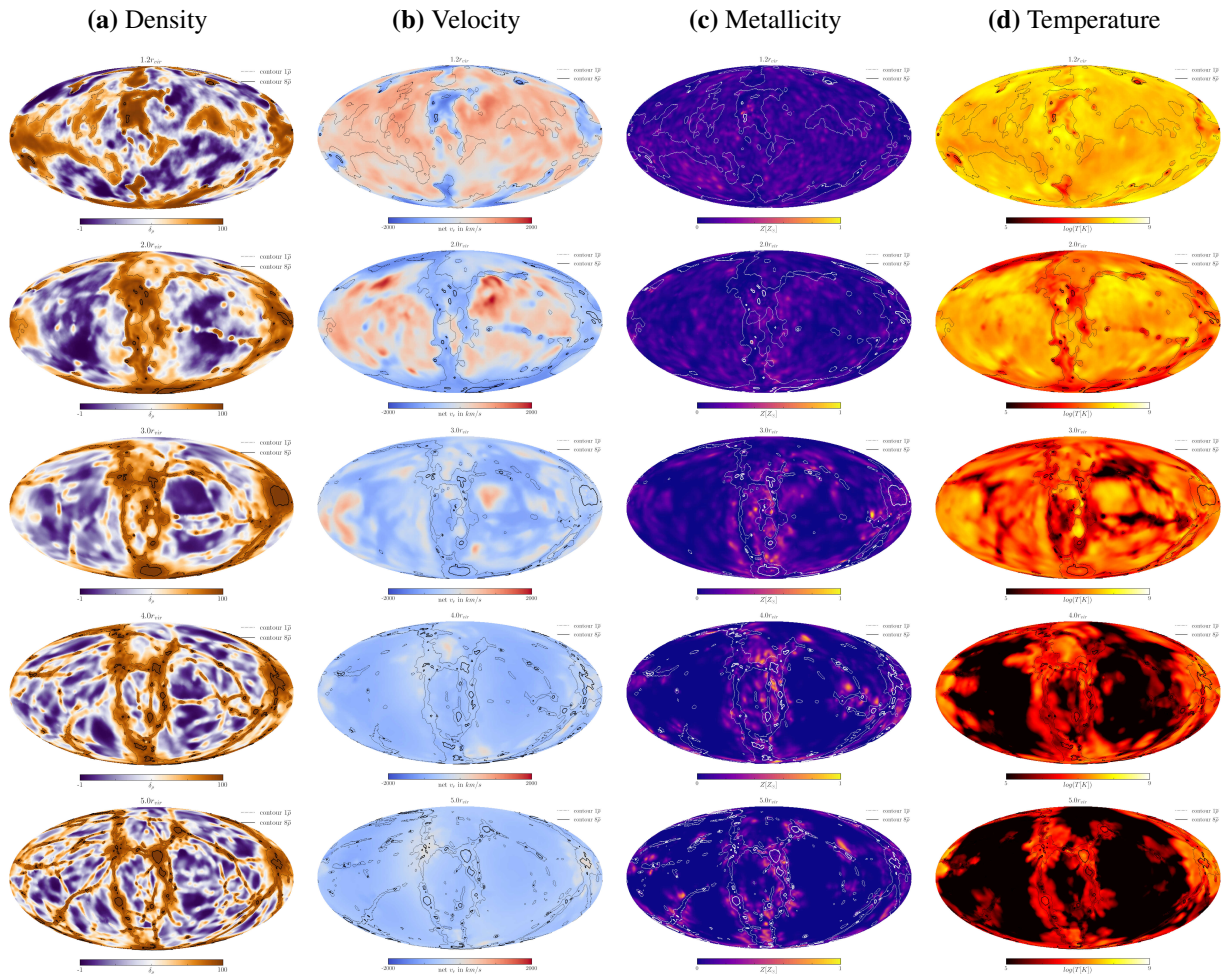
**Radial evolution of the fields: The giants** To investigate the radial extent of the features in the outskirts of the halos it is necessary to map the radial evolution of the fields.

Figure 4.4 shows the same fields at 5 different radial bins. The radial extent of the outflowing component is striking. At  $2r_{vir}$  its distribution is nearly unchanged while at  $3r_{vir}$  it begins to fade in some regions, almost completely vanishing at  $4r_{vir}$ . This extent and the the typical blossom-like structure (see  $3r_{vir}$ ) created by localized shocks hint very strongly at



**Figure 4.3:** Full sky field components for cluster 5 at  $1.2r_{vir}$ . The  $8\bar{\rho}$  over-density and  $1\bar{\rho}$  contours are overlaid onto each map. The density map is drawn with histogram color weighting to enhance contrast, as it is shown only to visualize the meaning of the contours. Here and in the following  $v_r < 0$  will mean inflow and  $v_r > 0$  outflow.

an MA-shock as described in Zhang et al. (2020). Cluster 5 is a fairly relaxed halo (Kimmig, 2022), so it can be argued that the shock would have had time to travel this far outwards since the last merger event accelerating the accretion shocks. A comparison with cluster 20 – the dynamical counterpart to 5 – confirms this: Here the shock features are less extended as most likely not as much time has passed since the last merger shock was formed. Both cluster 5 and 20 show a strong drop in the temperature after the shock fronts are left behind, with only occasional hot spots from  $3r_{vir}$  most likely associated with smaller haloes in-falling within the filaments. The metallicity also loses its homogeneity further out as the enriched gas distributed by the shocks gets left behind. It accumulates in the vicinity of the filaments but outside of the overdensities, forming an enriched and diffuse atmosphere for the dense spines of the cosmic web. The clear emergence of the general cosmic web structures at large radii for both clusters should also be read as a warning to keep in mind for the following sections: The flows we calculate with the methods outlined above are *halocentric*, however at sufficiently large radii the motion we are registering is not necessarily only correlated to the halo anymore, but to the general neighbourhood it exists in. One clusters outflow might well be another’s inflow and vice versa in these regions, which makes interpretation not always straightforward as we shall see. This is another reason for also computing the gas temperature and metallicity as the additional information can help disentangling contributions from different environments.



**Figure 4.4:** Maps of the four fields at radial slices for cluster 5.  $r \in [1.2, 2.0, 3.0, 4.0, 5.0]r_{vir}$

**Radial evolution of the fields: The dwarfs** To highlight the differences between the scales, Figure 4.6 and Figure 4.7 show the same radial evolution at the low mass end of the sample. The density structures in Figure 4.6 and Figure 4.7 appear to contradict a self-similarity of the surrounding web structure down to those scales. At the outer radii the web-like morphology seen around the clusters is not observed. Since the sampling procedure selected only parent haloes, this difference can not be explained by the groups and galaxies being embedded in larger overdensities. The cosmic filaments these groups and galaxies most likely live in appear to not have a fractal property. Whether this is due to resolution limits is unclear at this point. Temperatures and velocities are significantly lowered for haloes 53 and 384 compared to the massive clusters in the previous section. Both effects are closely linked and mainly caused by their much shallower potential wells. The correlations seen between flow direction and density at the spherical surface are much less clear for the two smaller haloes. This is also true for the link between outflows and temperature enhancement.

**Symmetry** In the previous sections, it became apparent that the out-flowing gas component is more homogeneously distributed on the sphere than the inflow, because the latter is organized in filaments while the former is distributed by shock heating and subsequent thermal gas expansion. To both check whether this perceived discrepancy is quantifiable

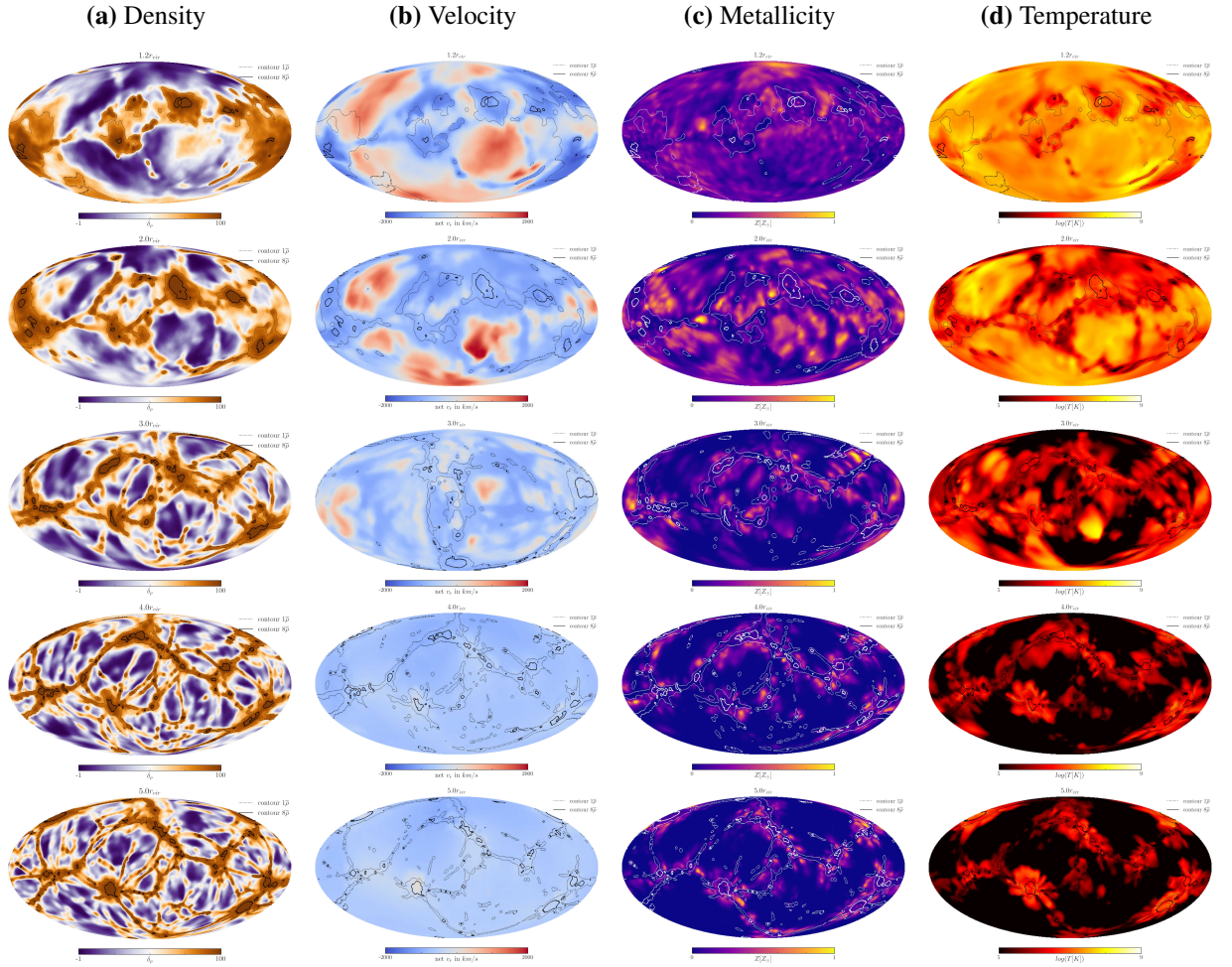


**Figure 4.5:** Maps of the four fields at radial slices for cluster 20.  $r \in [1.2, 2.0, 3.0, 4.0, 5.0]r_{vir}$

and also true for the sample at large, I used the power spectrum of the spherical harmonic functions. This idea was inspired by the symmetry analysis traditionally used for the CMB and the work by [Gouin et al. \(2022\)](#), who used a similar method on simulated clusters in 2D projection, notably finding a distinction between the symmetry of the hot gas in clusters vs. groups. The spherical harmonics are defined by:

$$\Delta_{S^2} Y_{lm} = -l(l+1)Y_{lm}, \quad (4.5)$$

namely they are the eigenfunctions of the Laplace operator on the sphere (for a concise summary see [Bartelmann et al. \(2014\)](#)). As such they span the space of square-integrable functions on the sphere. This means that every scalar function on the sphere  $f \in L^2_{S^2}$  can be expressed as a scalar combination of the spherical harmonics:

$$f(\theta, \varphi) = \sum_{l=0}^{\infty} \sum_{m=-l}^l a_{lm} Y_{lm}(\theta, \varphi) \quad (4.6)$$

The  $a_{l,m}$  are the vector components of the base function, which are obtained, like vector components usually are, by projecting the function onto the respective spherical harmonic. These spherical harmonics have different angular symmetries (an intuitive rule of thumb is

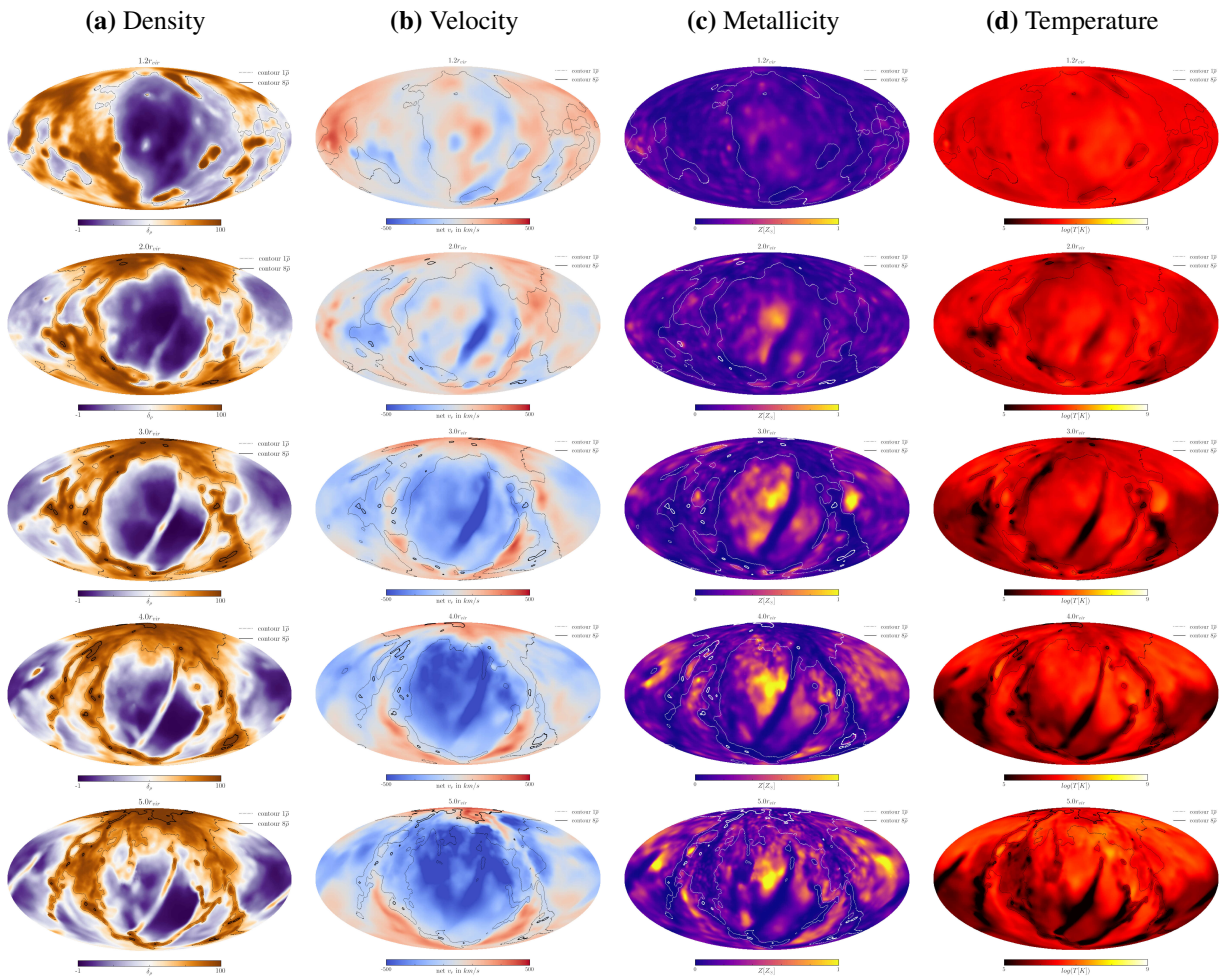


**Figure 4.6:** Maps of the four fields at radial slices for cluster 53.  $r \in [1.2, 2.0, 3.0, 4.0, 5.0]r_{vir}$

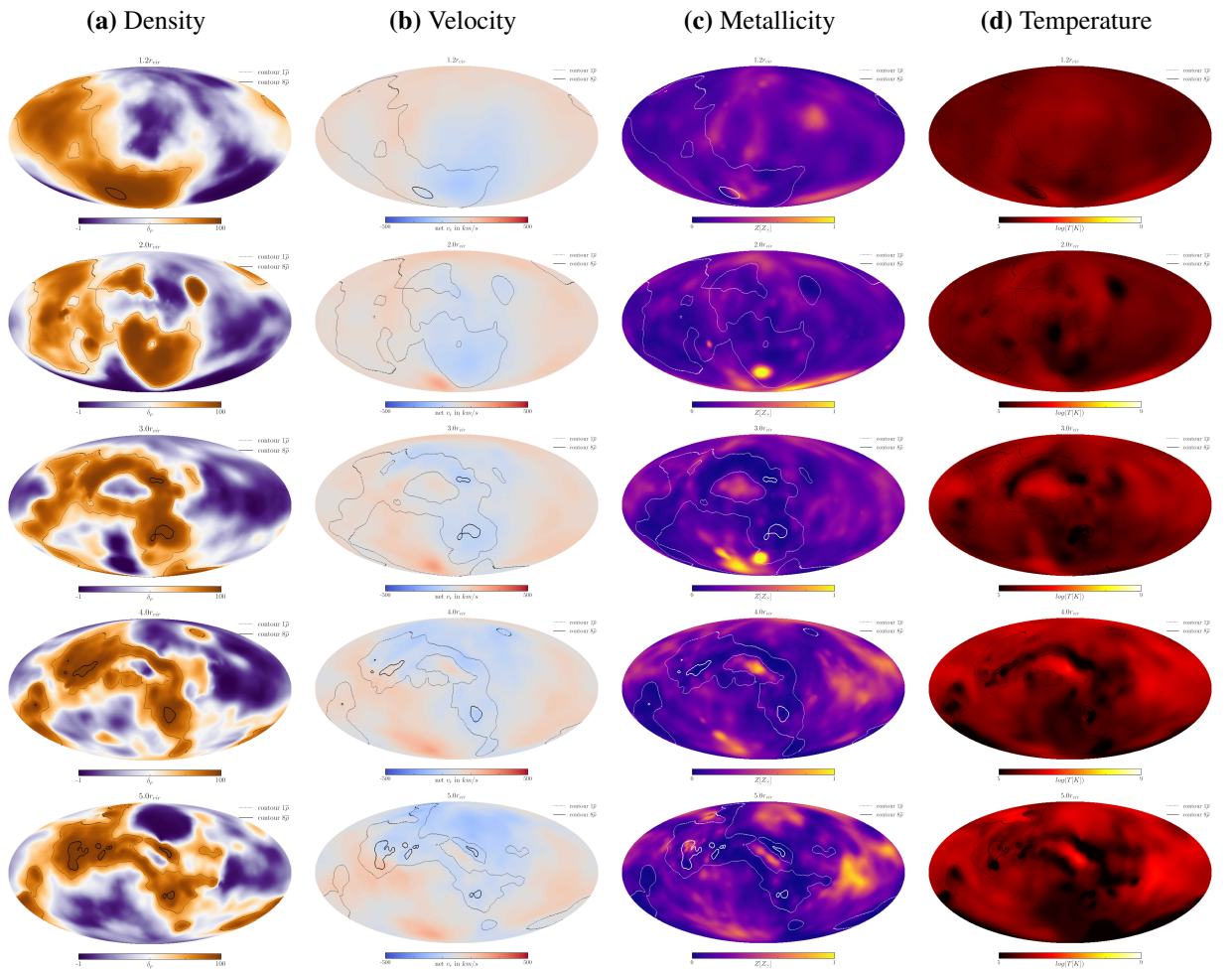


**Figure 4.7:** Maps of the four fields at radial slices for cluster 384.  $r \in [1.2, 2.0, 3.0, 4.0, 5.0]r_{vir}$

that the  $Y_{lm}$  varies on an angular scale of  $\frac{2\pi}{l}$ , so the monopole is homogeneous, the dipole varies on a  $2\pi$  wavelength etc. ), so to measure the "power" in a certain symmetry, one has to calculate the power spectrum of the multipole expansion:

$$C_l = \langle |a_{lm}|^2 \rangle \quad (4.7)$$

The python library *healpy* (Zonca et al., 2019) provides a framework for handily computing the power spectra of *healpix* maps. In order to define the total deviation from the monopole distribution, I define the quantity

$$\zeta = \sum_{l=1}^{300} l(l+1)C_l \quad (4.8)$$

as a measure of the power in the moments higher than the monopole. Figure 4.8 shows

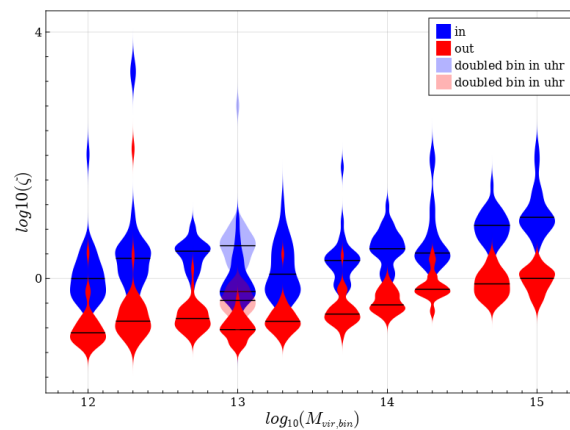


**Figure 4.8:** Excess asphericity for the sample of haloes computed from the mass in- and outflow fields. The distributions of the individual haloes at each bin are shown at the mean bin mass. The  $10^{13}M_{\odot}$  bin is present in both Box4 and Box2b, hence it is doubled. The distribution of the Box4 bin is shown with transparency.

what we saw before by visual inspection: In general the samples inflow component has more power in the aspherical modes than the outflowing component due to the in-falling particles being concentrated in the filaments. Gouin et al. (2022) found the WHIM phase to be more symmetrical in groups than in clusters. Figure 4.8 shows this trend to some degree, although it should be noted that this figure does not split the gas by phase but by direction of the radial velocity, so a direct comparison should be taken with a grain of salt. Especially the out-flowing components, which reach temperatures of around  $10keV$  in the cluster outskirts according to Figure 4.3, Figure 4.4 dilute this picture, as they are partially in the hot gas regime and might not be traced well by the WHIM. Unfortunately there is no analysis of the symmetries of the hot gas outside of  $R_{200}$  in the work by Gouin et al. (2022).

Another interesting observation from Figure 4.8 is the transition bin between the two resolutions. Groups at the  $10^{13}M_{\odot}$  bin appear to have more power in higher-order symmetries in the *uhr* box than the *hr* box. A possible explanation is that filamentary structures are resolved to finer detail in the higher resolution run, generating a more aspherical distribution.

This could be tested in future analysis by applying appropriate smoothing to the data to eliminate the additional noise. It is worth bearing in mind however, that especially the high resolution bin samples haloes at the very top of the mass range of the small *uhr* box, so in addition to the low number statistics, it also has a significant scatter in mass, so this offset should not be over-interpreted. Follow-up studies to these exploratory results are necessary and can shed more light on the symmetries in the gas components from *Magneticum* haloes.

## 4.5 Must what goes in indeed come out? – Accretion rates across the scales

**Mass flows at low redshift** Now that we have studied the spatial distribution of individual velocity fields, let us return to the first question posed in the introduction: Figure 4.9 shows

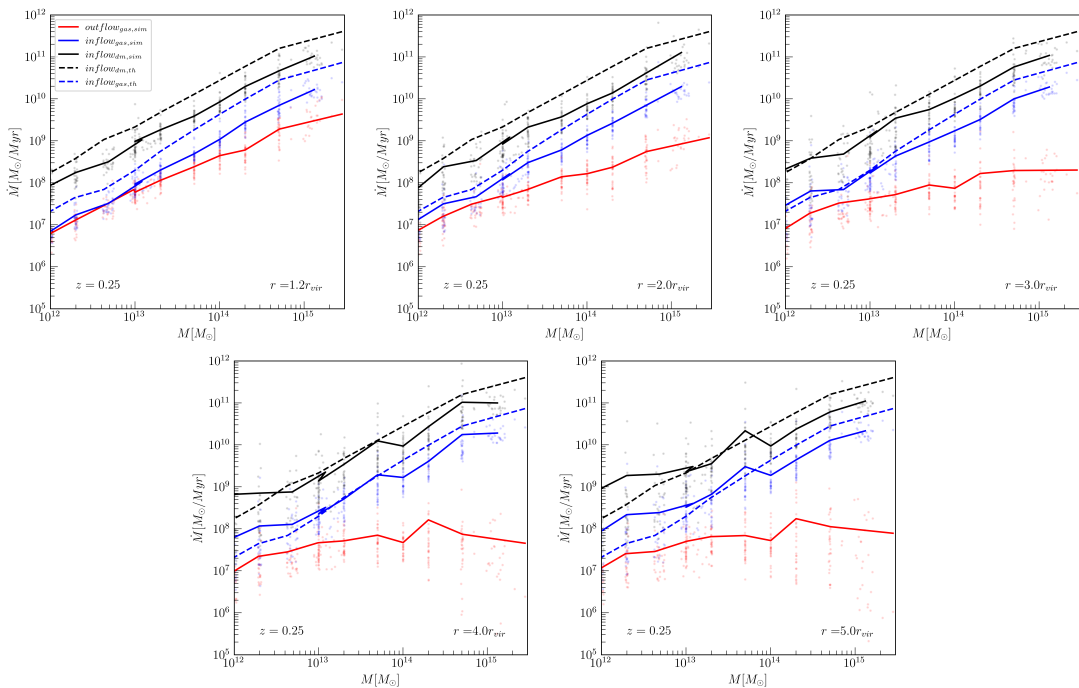


**Figure 4.9:** In- and outflow rates over the entire mass range of bins as compared to the theoretical accretion rates obtained with the model described in van den Bosch (2002). The theoretical gas curve is computed from dark matter with the stellar mass fraction fit from Andreon (2010).

a distinct mass trend for both flow modes with a relatively constant slope for each radial bin. The inflow curves imply a strong self-similarity in the accretion of haloes, remarkably so down to the galaxy mass range and across the resolution border at  $10^{13} M_{\odot}$ . The outflow curve noticeably flattens out towards higher masses with increasing radii, indicating a higher outflow generation efficiency for smaller objects. This is possibly due to the different mechanisms that can drive the outflows at the two extreme ends of the scale. While the large galaxy cluster can only drive outflows by thermal effects, galaxies also have AGN and Supernova-driven outflows that could be able to extend further out radially than the expanding hot atmospheres of the clusters. Additionally the deep potential well of a heavy cluster might prevent out-flowing

more efficiently. An alternative explanation for the persistence of outflows at low masses is a smoother transition into environmental flows for these halos. Because of hierarchical collapse smaller halos have formed first, The general shape of the [van den Bosch \(2002\)](#) model is reproduced quite well by the sample, which is remarkable given the simplistic assumptions (purely spherical collapse) it is built upon.

**Mass flows at high redshift** Accretion processes undergo permanent evolution across time, so it is a good idea to ask how the picture of [Figure 4.9](#) changes once we take a step (or in this case rather a leap) back from  $z = 0.25$  to  $z = 4.23$ . In general accretion rates are expected to increase with increasing redshift (compare the redshift dependency of the MAH [cross reference to theory] or for a numerical study [Fakhouri et al. \(2010\)](#)). For the following analysis the mass bins were kept from  $z = 0$  to allow for a direct comparison with [Figure 4.9](#) and to avoid tracing back individual haloes via the merger tree. This however means that the halo sample is necessarily different from the first plot, since the 319 haloes in that sample would be at an earlier stage in their evolution and thus in lower mass bins. Unfortunately this goes along with lowering statistics even further due to the lower abundance of high mass objects in both boxes, leaving the sample at only two bins, representing the seeds from which the clusters and heavy groups in the low redshift sample grow. Results should therefore be interpreted with caution here, they serve as a first look at the temporal evolution of the scaling relations found in [Figure 4.9](#). At high redshift, the mass accretion rate is systematically higher

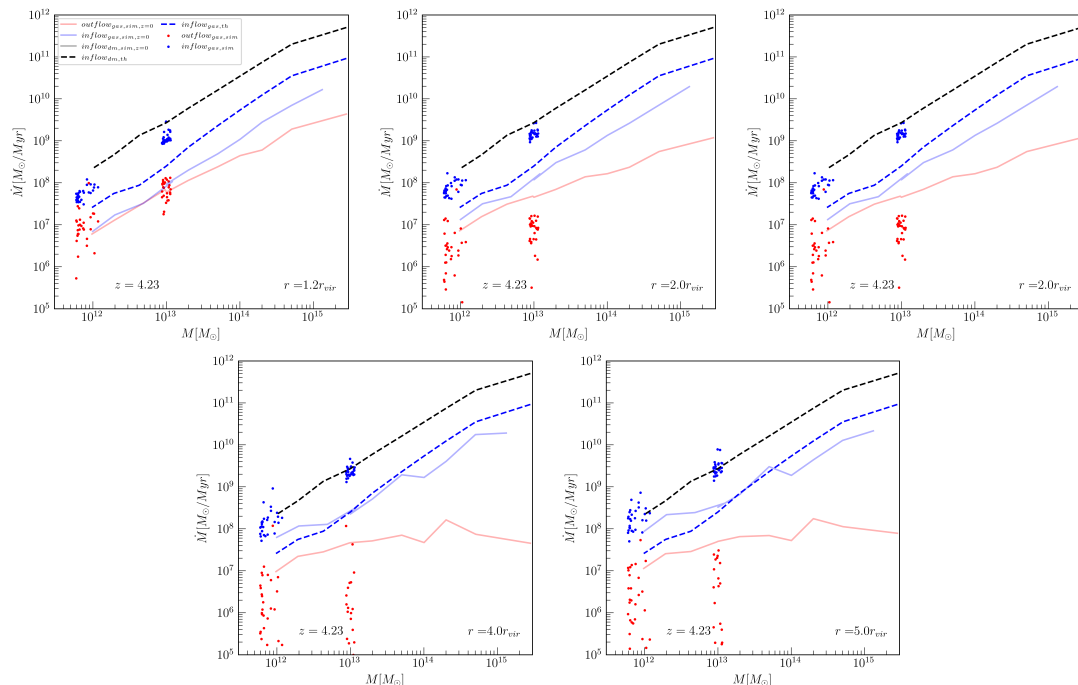


**Figure 4.10:** In- and outflow rates over the entire mass range of bins with the theoretical curves as before at a higher redshift. The transparent lines indicate the data at  $z = 0.25$ .

than at low redshift, as expected. The inflow rates are significantly higher than the theoretical curves predict, sitting on top of the *dark matter* curve. The former is hardly surprising as the model used to compute stellar fractions was obtained from low-redshift observations only,

severely overestimating the stellar fractions (and underestimating the gas fraction) at high redshift. Furthermore the accretion rate in the  $10^{12}M_{\odot}$  mass bin exhibits a shallower growth radially than at late times, remarkably so while the  $10^{13}M_{\odot}$  bin shows a radial evolution more consistent with the low redshift sample. Interestingly, the outflow at the innermost radial bin is unchanged compared to the low redshift sample implying that the formation pathway of these outflows remains the same across time. The radial drop in outflow rate is faster than at late times, most likely because the shocks have not had time to traverse the outskirts as far, lending further weight to the model of shock driven outflows.

**Metallicities and temperatures** As discussed in the introduction to this chapter, gas temperature and metallicity are important signifiers of the driving mechanisms of the outflows and the origins of the gas they comprise of. In the maps of section 4.4 some differences between the temperature and metallicity distributions at the opposing end of the mass scale already became apparent. For a more quantitative view of this, Figure 4.11 shows these two quantities across the sample in the same way as Figure 4.9 did for accretion rates. In general

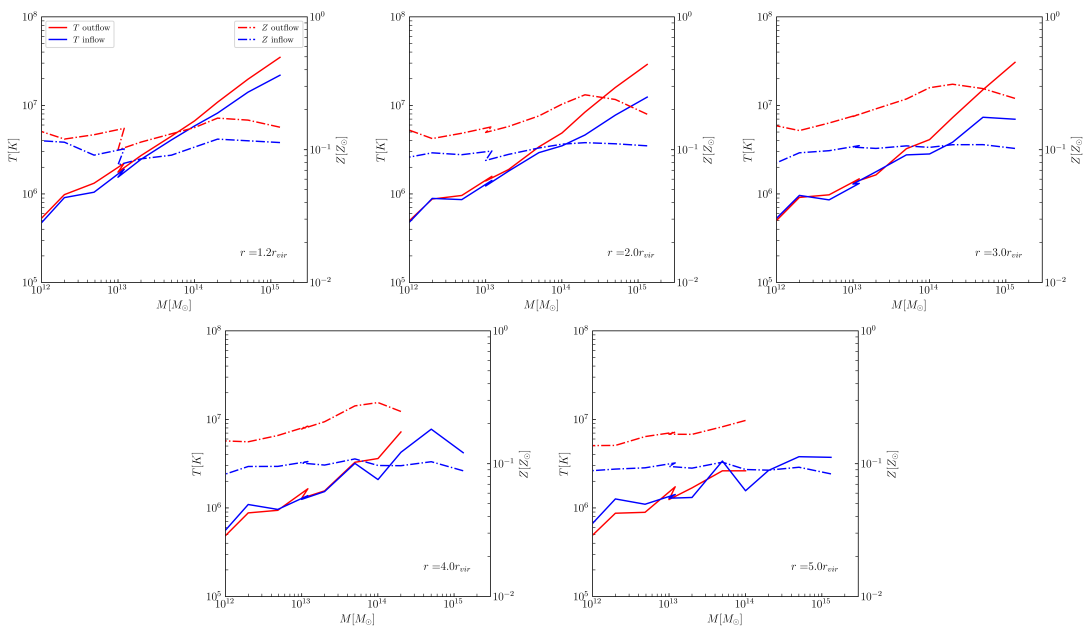


**Figure 4.11:** Metallicities and Temperatures of the in- and outflow dominated regions. The outflowing curves terminate at large radii for the most massive bins, because these clusters tend to be completely inflow dominated pixel-wise.

Figure 4.11 demonstrates outflowing gas to be more metal rich and hotter than in-flowing gas, albeit the inflow temperature is not consistent with a cold gas inflow as we have already seen in Figure 4.4. This agrees with the findings of Zinger et al. (2016), who registered that the in-falling gas had already reached  $10^6 K$  at the virial surface of clusters (albeit at  $z=0$ , so it is interesting that the value at  $z=0.25$  is almost exactly the same), consistent with the values in Figure 4.11. This warm, rather than cold, inflow can penetrate into the inner regions, contributing to the complex gas dynamics within the virial surface of the cluster (Markevitch & Vikhlinin, 2007).

A notable exception to the general rule that outflowing gas is hotter than in-flowing gas is the outermost region at the low mass end of the sample with the inverse true from  $4r_{vir}$  outwards. Considering the temperature map of the lightest "poster child", this is likely caused by environmental contamination. Figure 4.7 shows an isolated hot spot in this region, enveloped by the density contour. So the hot "inflow" for these objects could just be the diffuse outflow of their next larger or equally sized neighbour. This would also explain the crossing of the temperature curve in the high mass end of box4. The haloes at  $10^{13} M_{\odot}$  have fewer possible neighbours with sufficient mass to significantly impact the temperature of the dense and cold inflow. Between the mass bins, temperatures follow a steep scaling law closest to the halo centres, which flattens out at larger radii, most likely also due to sampling the general environment in those regions. As already hinted at in the comparison of Figure 4.4, Figure 4.5, Figure 4.6 and Figure 4.7, metal profiles are relatively flat, with a slight increase towards higher masses and notably a maximum at the bin with  $2 * 10^{14} M_{\odot}$  in both in- and outflowing regions. The origin of this peak is unclear, further analysis might shed light on this apparent saturation at large masses. Overall there is a noticeable increase of metallicity with radius, which can also be ascribed to an increased sampling of the surrounding cosmic web.

## 4.6 How are you enriching yourselves?– Flow metallicity evolution

It was briefly mentioned in the introduction that the precise type of enrichment can shed light on the history of the gas, namely whether it was enriched at early time or late time. This is due to the different supernova enrichment channels producing different types of metals: The late-type SNIa from white dwarf progenitors produce significantly more heavy elements like iron compared to the early type SNe from core collapse. This is shown in Figure 4.12 which plots the metal fraction as a function of species for the different supernova models. The

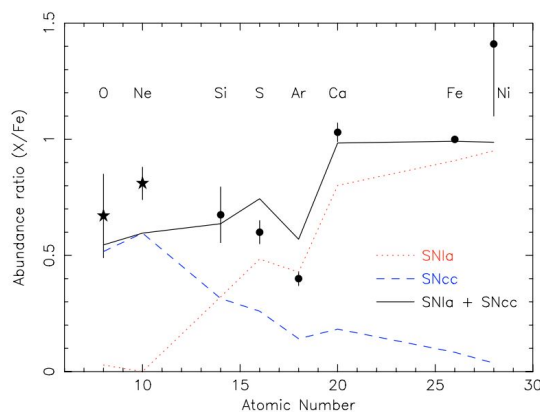
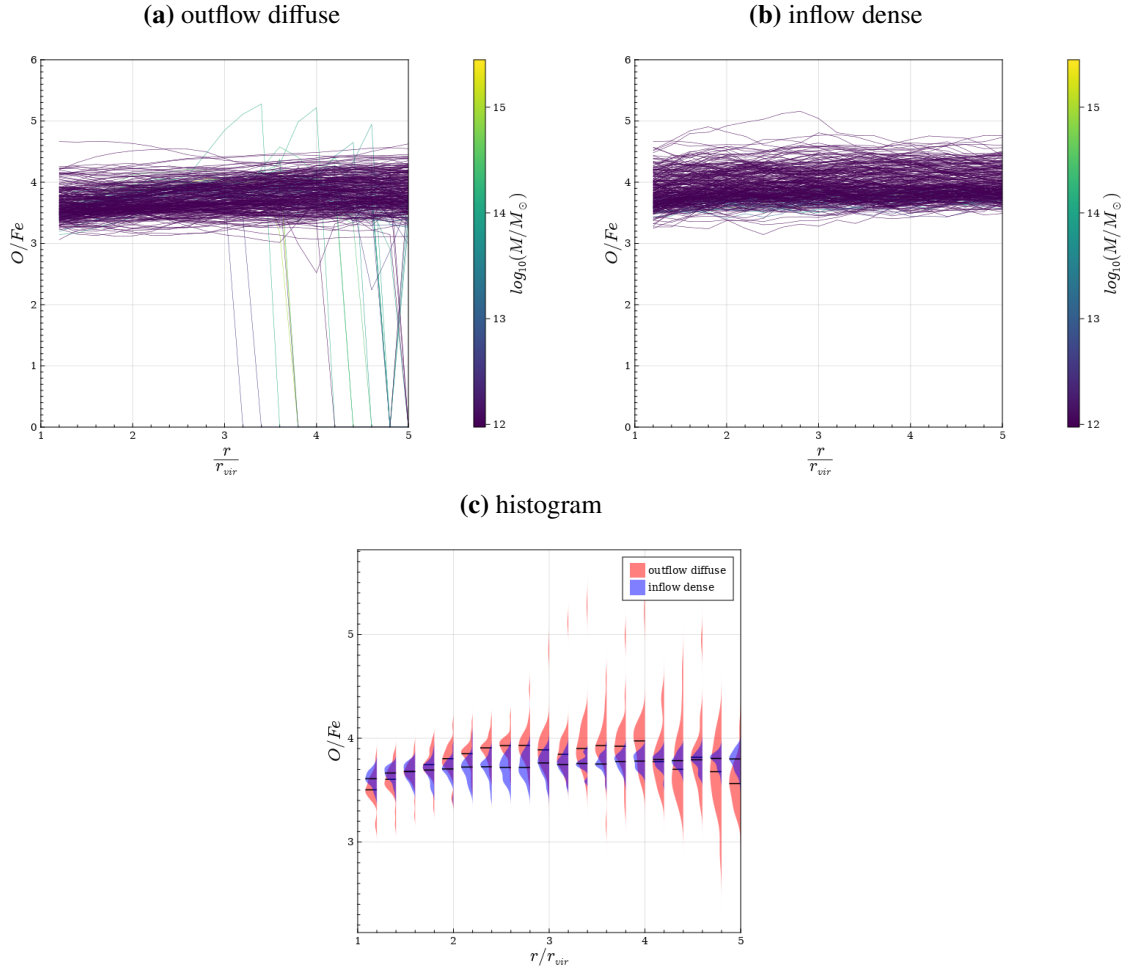


Figure 4.12: Enrichment models from de Plaa et al. (2007) Figure 9.

metal model by Tornatore et al. (2007) implements these enrichment models for the simulated

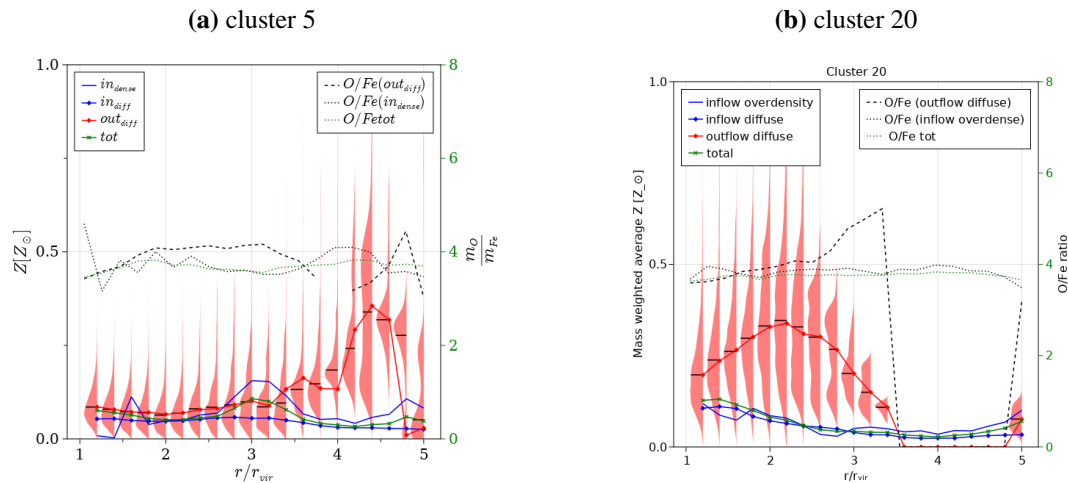
gas in the *Magneticum* boxes, therefore the relative amount of metal species present in the gas can provide information about the enrichment process. We use specifically the ratio  $\frac{m_O}{m_{Fe}}$  (abbreviated to O/Fe in the following) to discern between early and late enriched gas. Figure 4.13 reveals a flat O/Fe profile for most of the haloes with ratios clustered around



**Figure 4.13:** Radial O/Fe profiles for the complete sample. The *healpix* map has been filtered to include only the diffuse outflowing regions with  $\rho < 10 * \bar{\rho}$  and only the dense inflow regions with  $\rho > \bar{\rho}$ .

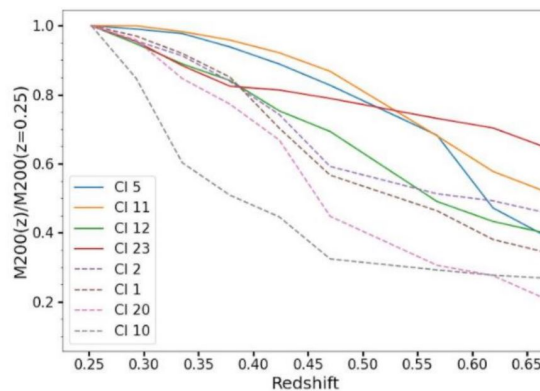
3.6. This is overall consistent with the expectation of early enriched gas largely lacking the Fe mass from SNIa. The inflow profiles are largely consistent with this picture, exhibiting a slightly higher O/Fe value, likely hinting at dilution with Fe-enriched gas from the inner regions of the cluster for the outflows. There are distinct peaks for some haloes, mostly at the high mass end, exhibiting a steep rise and then a drop as the diffuse outflowing component vanishes. To try and shed light on the origins of these spikes and to test the hypothesis of an early enriched outflowing component that is first enriched while in-falling and then shock heated, we now investigate the precise enrichment properties and histories with a detailed case study of two example haloes. For this we turn once again to our familiar "poster child" haloes.

**Enrichment histories: A case study for galaxy clusters** First let's take a close look at the whole metal picture for both of these clusters:



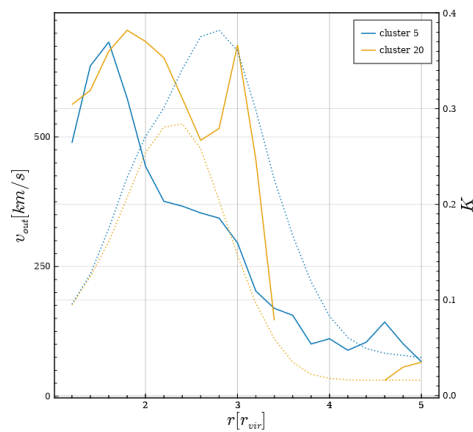
**Figure 4.14:** Radial profiles of  $Z$  and  $O/Fe$  for all flow components. Density definitions as before.

Figure 4.14 shows a clear distinction between the two clusters: While cluster 5 proves to be a "flat" halo, with the only significant enhancement at large radii where the environment becomes noticeable, cluster 20 is one of the haloes identified in Figure 4.13, exhibiting a peak both in total metallicity and in  $O/Fe$  ratio of the diffuse outflow. This hints at a more recent induction of early enriched gas, which is consistent with the classification of the two clusters by Kimmig (2022): Cluster 20 is one of the most dynamically active clusters in the



**Figure 4.15:** Accretion histories for a selected subset of the 29 clusters in the high-mass bin. Note the difference between the two "poster children" 5 and 20. Figure 8.42 from Kimmig (2022)

highest mass bin, having only recently acquired a large portion of its mass (see Figure 4.15). The observed enrichment crest is most likely a remnant of this recent activity. Interestingly there is a delay between the two peaks, with the  $O/Fe$  ratio increasing first and the general enrichment peak following behind at a distance of approximately  $1.3r_{vir}$ . Could this be an indicator of two separate processes, causing a spike in early enriched gas first and a second spike with a relatively higher ratio of late enriched gas, possibly from the inner regions of the cluster? To answer this question, consider the dynamical state of the gas: Figure 4.16 shows that the peak in total enrichment is not only located upstream of the  $O/Fe$  peak, but likely



**Figure 4.16:** Radial evolution of outflow velocity and total entropy for clusters 5 and 20. The shocks are clearly visible in the entropy profiles, while the velocities show clear discrepancies between the haloes.

also inside the shock front, indicated by the clear entropy peak. This could be an indication for a different origin of this particular outflow, which is clearly separate from the outflowing peak downstream of the shock. A link to recent merger activity is possible and with the full information of the merger trees, future work can shed more light on these peculiar profiles. Notably the in-flowing component, dominating the total mean because of its larger density, is flat for both clusters. The filaments that feed these two very different objects appear to be similar in composition.

To draw back the curtain even further, a look at the real enrichment histories of the outflowing gas is worthwhile. So far the information about the exact timeline of the metal evolution in the cluster outskirts has been present in the radial profiles, but convoluted with radial density profiles and possible mixing of the different layers. To isolate the temporal evolution I chose a tracking approach: 40 particles were selected at random, though in specific enrichment type ranges (see caption of Figure 4.17) from the diffuse outflowing component at  $z=0$ . I then follow each of these particles back in time and record their enrichment, O/Fe ratio and temperature at each snapshot. The much talked about early enrichment becomes apparent: The particles that will eventually constitute the outflow fall in and get enriched at cool to moderate temperatures where star formation is possible. They are then shock heated at the boundary. During this heating process there is dilution with iron richer gas, as O/Fe ratios drop to then remain relatively stable with regards to their metallicity at late times. Cluster 5 exhibits a number of particles that are already heated at  $z=4$  and consequently don't undergo significant enrichment. Unfortunately the histories of cluster 20 do not reveal a clear separation in time between the two radial enhancement peaks observed. In general there is not clear discrepancy to be made out between the dynamically relaxed and unrelaxed cluster. Since the metals get enriched in similar filaments for both of these haloes, this is reassuring.

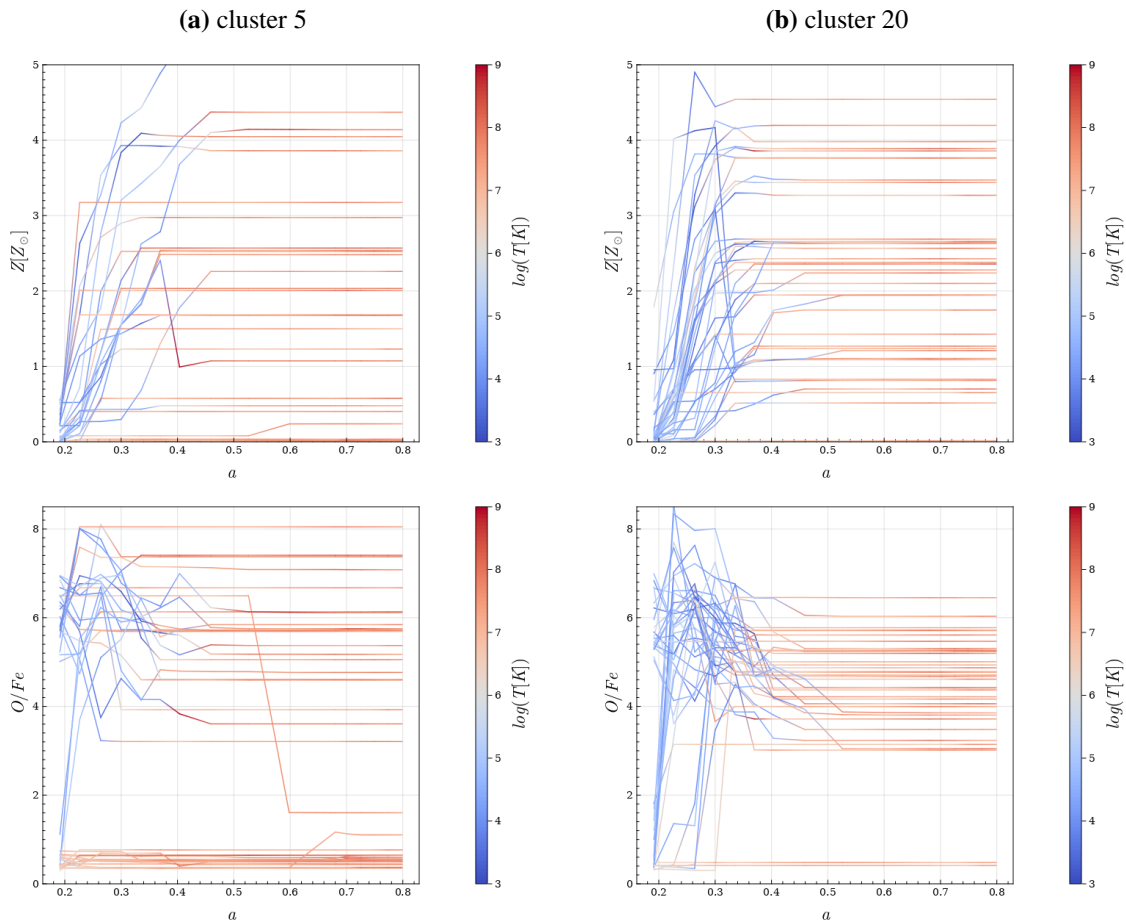


**Figure 4.17:** Enrichment histories for clusters 5 and 20. Each line represents a single particle that is in the outflowing component at  $z=0.25$ . Out of this set two discrete groups of particles have been selected based on their  $O/Fe$  ratio at  $z=4$ : 20 particles with  $O/Fe \in [0, 2]$  and 20 particles with  $O/Fe \in [5, 7]$ .

## 4.7 Summing up: What we learned about haloes

Before moving on let's take a moment to review what we learned so far: This chapter's goal was to forward understanding of the gas accretion processes and their influence on the outskirts of haloes of a variety of sizes. We used a sample of 319 simulated haloes from cluster to group scale and measured the flows, temperatures, densities and metallicities in their outskirts. The general model of a warm filamentary inflow and a hot diffuse outflow was confirmed by the spatial distribution of in- and outflows and their temperatures, though it should be noted that the situation looks less clear at the low mass end. This difference in spatial configuration of the in- and outflows manifests itself in the spherical symmetries of the respective streaming fields in that in general outflows are more spherically symmetrical. A clear mass trend was not apparent, however there is a hint at the decrease of asphericity with decreasing mass reported by [Gouin et al. \(2022\)](#). Here future simulations combining the high resolution of box4 and the size of box2b might help to clarify the trends, as there is a peculiar jump at the transition between the two boxes.

One of the two main questions this chapter was intended to address was whether the gas and dark matter accretion is a self-similar process. [Figure 4.9](#) showed a striking self-similarity

stable to scale and even resolution. The comparison to an accretion model derived from the EPS formalism demonstrated a good approximation of simulated flows with gas accretion by that model. The observed self-similarity of the inflows does not hold for the outflows when going to larger radii with a deviating slope already visible at  $r = 1.2r_{vir}$  at the high mass end. This indicates a possible discrepancy between the outflow driving mechanisms for clusters and galaxies. Another explanation is the difference in large-scale environment between these two types of haloes. Further investigations, with more focus on the shock positions and properties as well as correlation of the galactic outflows with AGN jets and starbursts that also drive powerful outflows can help shed more light on these findings. A future study should also include a method for separating environmental inflows from halo outflows more clearly, as this picture is quite unclear at the moment.

From the gas and temperature maps the picture of initially cold in-falling gas that gets heated to a warm ( $\sim 10^6 K$ ) phase and enriched in the filament, before being shock heated to a hot phase at the outer boundaries of the clusters and largely maintaining its chemical composition is solidified. This also means that the end state of the hot gas in the outskirts of clusters could be useful as a tracer of the in-fall history of that gas. A follow-up study to the connection between in-fall and chemical history can shed further light on this. A more focused study on the more peculiar features we encountered in this chapter could also be useful in furthering the understanding of the processes in the cluster and galaxy outskirts beyond this thesis. Future simulations can also help with this process as maintaining realistic large scale structure with adequate box sizes while improving resolution to model the dynamics in greater detail will improve statistics and precision of these analyses. There is yet a lot to learn about the universe in the fringe regions of overdensities.



# Chapter 5

## The Presence of Absence: Cosmic Voids

“I love talking about nothing, father. It is the only thing I know anything about.”

---

Lord Goring, *An ideal husband* by

Oscar Wilde

### 5.1 One man’s gain is an other’s loss: Decretion

The previous chapters have treated structure formation from the perspective of initially overdense regions that collapse to eventually form the rich structures we observe today. However, like most stories, structure formation has two sides: While matter accumulates onto the growing filaments and nodes, it leaves behind growing regions of emptiness in between those building block of the cosmic web. If we were to ignore those voids, we would ignore the largest structures we can observe in the universe and along with them a majority of its volume (Sheth & Tormen, 2004). To get a good first order understanding of what these "objects" are exactly we can think of them as anti-haloes. Where haloes accrete matter, voids decrete. Because of their large sizes (exactly opposite to haloes they *grow* in co-moving space with time) and their extremely low matter densities, voids are regions of interest for many subdisciplines of astrophysics: They can be used to analyse matter organization patterns on the largest scales, trace local tidal fields and due to their poorness in matter and thus gravity, provide something close to alternate universes with cosmological parameters tilted more towards the mysterious dark energy component, allowing us to probe its properties. Because the matter that remains in them still undergoes structure formation, albeit strongly suppressed by the more rapid expansion, galaxies in voids are used to study formation scenarios for these objects free (or nearly free) from environmental influences. Lastly, as we will see in the next chapter, void shapes are a promising candidate for the independent measurement of otherwise degenerate cosmological parameters, strengthening our understanding of the composition of the world we live in. In this chapter we will consider these fascinating regions from a theoretical perspective. Theory can offer us predictions as to how voids evolve and

shed light on their typical properties like sizes and shapes. Furthermore we can derive recipes for how to define these regions and how to extract them from data we are usually provided.

## 5.2 Turning the top hat inside out: Model of an isolated void

The simplest model for the individual evolution of a void is the formation an "inverted" spherical top-hat from an isolated, initially spherical, underdensity – basically an anti-halo (compare section 3.3.5)(Blumenthal et al., 1992). The analysis of spherical underdensities allows for a 1-D treatment of the dynamics, which simplifies matters significantly. While the initially overdense regions expand slower than the background universe, eventually reaching a maximum radius at turnaround at which point they completely decouple from the background and collapse, the opposite is true for underdensities: A spherical mass shell centered on an initial underdensity will expand faster than the general expansion of the universe due to the density deficit inside it. As in the collapsing case, this effect is also self reinforcing as the shell begins to expand in co-moving space the density inside it drops further, leading to a peculiar acceleration relative to co-moving space. This acceleration increases closer to the center, proportional to the density deficit, so the closer to the center of the spherical top-hat a shell is, the faster it accelerates. Eventually this effect leads to a **shell-crossing**, i.e. the shells that started inside catch up with the slower shells that started at a larger radius. This is generally associated with the formation of a void. Since at the shell-crossing time all shells have expanded to the same co-moving radius, similar to the collapsing shells reaching  $r = 0$  at  $t_{coll}$ , the void has formed an infinitely steep spherical wall at its border, which can from this point onward be considered a single mass shell expanding outward self-similarly (Bertschinger, 1985). Calculations show (Sheth & van de Weygaert, 2004), that at this time the density inside the void has reached 20% of the average density of the universe (this is contrasted by the unphysical underdensity the void would have reached, had it evolved linearly for the same period  $\delta_v = -2.81$ ). This parameter is widely used as the maximum density a region can have to still be considered a void by the common void finders (Sutter et al., 2014b). The outermost mass shell of the void region has expanded by a characteristic factor of  $\approx 1.7151$ . It is fairly intuitive, that initially spherical underdensities remain spherical. There is however a peculiarity of isolated voids, that ensures even initially non-spherical setups to become more spherical with time: When we talked about the ZA approximation in chapter 3, we saw that there is a preferred collapse along the direction with the largest eigenvalue of the tidal field, which corresponds to the shortest initial axis, leading to the structure known as a pancake. For an initial non-spherical underdensity the argument remains exactly the same. The only difference is that the orientation is exactly reversed, due to the inverted density profile. This means that expansion will once again be the fastest along the shortest axis, *erasing* initial asphericities instead of enhancing them. Isolated voids will always grow more spherical as they evolve.

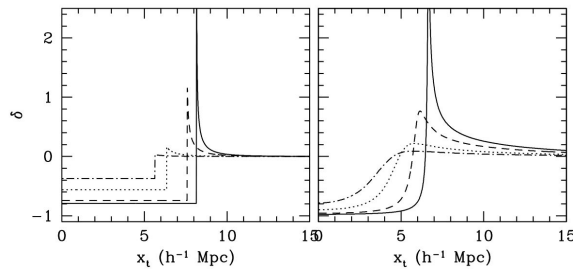


**Figure 5.1:** Spherical evolution of two initial radial profiles. The left profile starts as a pure top-hat depression while the right profile has the same initial density contrast, but is smoothed out for a more realistic profile. Both initial conditions evolve to similar top-hat like final states with the characteristic sharp ridge. Figure 3 from [Sheth & Tormen \(2004\)](#).

## 5.3 Empty in numbers: The void size function

In the previous section we have seen how voids form. Akin to asking for the statistical properties of halos in terms of their mass (and later accretion rate) to better understand these objects, we now want to examine the properties of voids from a theoretical perspective. A logical starting point is to ask for the typical sizes of these objects:

### 5.3.1 The two-threshold excursion set formalism

The hierarchical model of structure formation and specifically the excursion set formalism introduced in chapter 3 has not ceased to be useful for our purposes. Similar to the way we described haloes as the result of the overdensity field crossing a certain collapse threshold, we might think of thinking voids as results of the exact opposite effect, i.e. the density field down-crossing a certain underdensity threshold. Similar to the overdense case, it is possible to derive from a top-hat spherical collapse description ([Bertschinger, 1985](#)) a density of non-linearity  $\delta_v$  (the linear underdensity at the time when mass shells start to cross due to the accelerated expansion inside the underdensity) that can be associated with the formation of a void. The naive approach would now be to simply invert the EPS method: A trajectory that first down-crosses  $\delta_v$  at a certain filter scale is simply associated with a void of this scale. For underdensities however, there is a decisive complication to the simple method of counting first up-crossings within a certain scale range: For the accurate description of a halo, the  $\delta_v$  barrier is essentially irrelevant: A  $\delta_c$  up-crossing inside a forming void region will collapse regardless and for the so-called *void-in-cloud* scenario of a void enclosed in a larger underdensity, the void will eventually collapse. From the perspective of describing voids with the Excursion Set formalism, this means however, that the *void-in-cloud* scenario can not be ignored, making the problem a "two-threshold" problem. For a given down-crossing of  $\delta_v$  at some scale  $R_1$ , we need to be wary of an earlier up-crossing of  $\delta_c$  at some scale  $R_2 > R_1$ . However this can be implemented into the Excursion set formalism with relative ease ([Sheth & van de Weygaert, 2004](#)). Essentially the fraction of volume tied up in voids of volumes between  $V_1, V_1 + dV$  is proportional to the fraction of trajectories that cross  $\delta_v$  between  $R_1, R_1 + dR$  (read: at a larger scale) without having crossed  $\delta_c$ . This gives size functions of

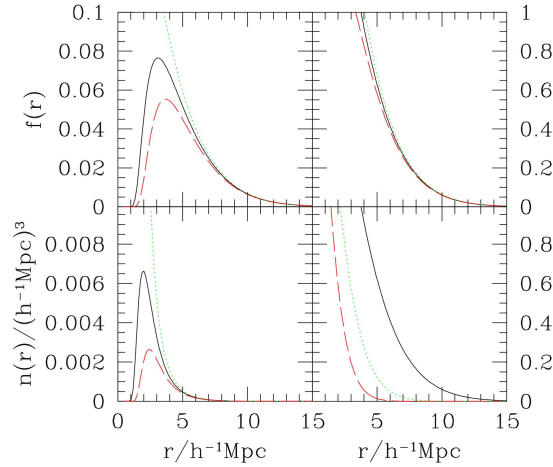


**Figure 5.2:** Void size functions computed by Sheth & Tormen (2004) (Fig 8.). The top panels show the mass fraction as a pdf (left) and cdf (right). Bottom panels show number densities, pdf and cdf. In all but the bottom right panel the colors indicate different choices for  $\delta_c$ , with  $\delta_v = \text{const.} = -2.81$ : Dashed red:  $\delta_c = 1.06$ , solid black:  $\delta_c = 1.686$ , dotted green: no void-in-cloud process, effectively  $\delta_c = 0$ . In the bottom right panel the time evolution of the size function is shown: solid black:  $z = 0$ , dotted green:  $z = 0.5$ , dashed red:  $z = 1$

the form shown below: Computing this fraction, one finds that  $V_{\text{void}} \propto 1 - D \propto \frac{\delta_c}{\delta_c + |\delta_v|}$  (Sheth & van de Weygaert, 2004), where  $D$  is called the *void-in-cloud* parameter, a measure for how close the two thresholds are to each other. Computing the volume fractions of all voids this way, one finds that for the "linear" parameters  $\delta_c = 1.686$ ,  $\delta_v = -2.81$  the volume fraction of voids is larger than 1 (Sheth & Tormen, 2004). This oversimplified calculation offers another view on the cosmic web discussed in chapter 3: Voids fill most of the available universe, leaving only the web-like structures surrounding them for the overdense regions in a foam-like configuration. Tuning the two threshold parameters is not as trivial as in the pure overdensity case, it is a matter of at which stage of collapse one would want to exclude a void enclosed within a larger overdensity that is collapsing giving radically different results in terms of the resulting void size function (Sheth & van de Weygaert, 2004). It should be noted that when speaking of "fixing"  $\delta_v, \delta_c$ , the understanding is that this means fixing these values at  $z = 0$ . As we have seen in chapter 3, the actual values of these thresholds will evolve in time with the linear scale factor  $D(z)$ . Similar to the case of haloes, from the Excursion Set formalism also arises a *void hierarchy* with sub-voids within voids. From considerations analogous to the overdense scenario, one can once again deduce that smaller voids emerge first and then merge to constitute larger voids (if they are not embedded within an overdensity) (Sheth & van de Weygaert, 2004).

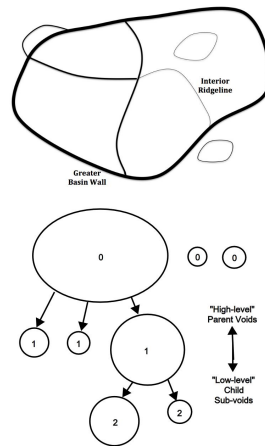


**Figure 5.3:** A schematic of the void hierarchy and its signature in void zones. The ridge lines drawn into the super-void are the remaining walls of its children. Figure 1 from Sutter et al. (2014a)

## 5.4 Nothing is ever really empty: Void substructure and other complications

Though heavily underdense, voids still contain matter. Although structure formation is heavily quenched in these regions they can still form galaxies and even larger structures like filaments and sheets:

### 5.4.1 A web between the web: Structure in voids

The hierarchical formation of voids discussed in the previous section has another implication: As smaller voids merge to form larger voids, their walls do not simply disappear. While over time most substructure will be swept away by the rapid outflows of the large mode underdensity, filaments and walls can also survive within a larger super-void, given a sufficient initial density. Signatures of such walls and filaments were already observed in early numerical simulations specifically dedicated to simulating voids (van de Weygaert & van Kampen, 1993). Sutter et al. (2014b) call this process *annexion* to contrast it to proper merging which erases the traces of the initial void hierarchy. These annexion events allow also for an analysis of the arising sub-voids at the present time, akin to subhaloes. This is another important difference to haloes: In mergers of large clusters significantly more information about the progenitors is lost in the violent relaxation processes and through the baryonic physics evolved. The void hierarchy allows for a much more primordial look at the density structure in the universe.

### 5.4.2 Don't leave me here to die: Void galaxies

From the perspective of hierarchical structure formation, we expect every positive peak in the density field to eventually collapse. This is also true for local density enhancements embedded into a large mode underdensity like a void. Consequently even these regions contain galaxies and sometimes even clusters. Because of the unique conditions in voids, i.e.

the low abundance of potential merging/collision partners and the absence of replenishment mechanisms these haloes are promising test subjects to forward our understanding of the formation processes of galaxies and their evolution in general.

## 5.5 I have no sphere: The non-spherical shapes of voids

In the simple case of an isolated underdensity discussed in the sections above, we have seen that voids are expected to grow more spherical as time proceeds, evening out any potential primordial asphericities due to the fact that they experience a super-Hubble expansion that is fastest along the shortest axis. However this calculus only considers isolated underdensities and it has been shown quite early on (Icke, 1984) that for realistic conditions the opposite is true most of the times. Voids are subject to their non-linear environments and tend to get distorted heavily by the strong and non-uniform tidal fields in their neighbourhoods. One of the reasons for this is, that a density depression – as opposed to a peak – can never grow in excess of  $|\delta| = 1$ , as the underdensity is bounded by  $\rho = 0$  with  $\delta = \frac{\rho - \bar{\rho}}{\bar{\rho}} = -1$ . For this reason, underdensities are relatively weak compared to the typical virialization overdensities for haloes of  $\delta = \mathcal{O}(10^2)$  (Böhringer et al., 2012). As was the case with the non-spherically collapsing filaments of the cosmic web, one way to approach the non-spherical evolution of voids is once again the Zel’dovich approximation. Ellipsoidal voids are as before slightly more accurate than spherical ones: For a standard  $\Lambda$ CDM model without baryons, Park & Lee (2007) derived an analytical solution for the statistical distribution of void ellipticities, defined as  $\epsilon = 1 - \frac{a}{c}$ , where  $a, c$  are the longest and shortest axes of an ellipsoid respectively: As we have seen before, in the Zel’dovich approximation the density can be written as

$$\delta(\mathbf{x}, t) + 1 = \frac{1}{(1 - \lambda_1)(1 - \lambda_2)(1 - \lambda_3)} \quad (5.1)$$

where  $\lambda_{1,2,3} = \lambda_{1,2,3}(t)$  are the eigenvalues of the tidal or distortion tensor as before and we have absorbed the time dependency from the linear growth factor  $D(t)$  into the eigenvalues themselves. As before this indicates a tri-axial collapse or expansion, depending on the initial density contrast. Contrasting the earlier discussion about the expansion of isolated voids, the tidal tensor here is explicitly **external** in nature, generated by the statistics of the large scale perturbation field. If we assume an eigenvalue ordering  $\lambda_1 > \lambda_2 > \lambda_3$  the axes ratios are given by  $\nu = \left(\frac{1-\lambda_1}{1-\lambda_3}\right)^{1/2}$  and  $\mu = \left(\frac{1-\lambda_2}{1-\lambda_3}\right)$ . From the definition of the ellipticity we can see that  $\epsilon = 1 - \nu$ . To get an analytical form for the ellipticity distribution of voids, it is therefore necessary to determine the probability distribution of the parameter  $\nu$  from the statistics of the Gaussian density field at a certain redshift  $z$ . We will not go through the exact steps of how this is derived here, but an outline of the argument is as follows: As we have already seen in chapter 3 (Equation 3.24), the distortion tensor in the ZA is related to the linear potential

at the Lagrangian position  $\mathbf{q}$ :

$$T_{i,j} = -\frac{\partial s_i}{\partial q_j} \propto \frac{\partial}{\partial q_j} \nabla \phi_{lin}(\mathbf{q}) \quad (5.2)$$

which is in turn to linear order completely specified by the density perturbation. It is therefore reasonable to assume that the components  $T_{ij}$  also follow a Gaussian distribution, with its mean and variance determined by the respective statistics of the density perturbation field (Doroshkevich, 1970). From these assumptions Doroshkevich (1970) derives

$$p(\lambda_1, \lambda_2, \lambda_3; \sigma_R) \propto \frac{1}{\sigma_R^6} e^{-\frac{f_1(\lambda_{1,2,3})}{\sigma_R^2} + \frac{f_2(\lambda_{1,2,3})}{2\sigma_R^2}} (\lambda_1 - \lambda_2)(\lambda_2 - \lambda_3)(\lambda_1 - \lambda_3) \quad (5.3)$$

where once again the smoothing scale enters as a parameter through the smoothing of the underlying density field and the functions  $f_1, f_2$  are both  $\mathcal{O}(\lambda^2)$ . The final distribution will thus depend on the smoothing scale chosen, a critical point to note, when comparing this model to observations and simulations alike. Park & Lee (2007) then impose the additional constraint of  $\delta_v = \lambda_1 + \lambda_2 + \lambda_3$  from the Taylor expansion of Equation 5.1 w.r.t. the eigenvalues to fix the density contrast to the void density contrast since the intention is to sample the eigenvalues specifically at underdensities. From this, the probability computed by Doroshkevich (1970) and the relationships of the axis ratios to the eigenvalues, they are then able to obtain the conditional probability  $p(v, \mu | \delta_v, \sigma_R)$  and by marginalising  $\mu$  via integration  $p(v | \delta_v, \sigma_R)$ . This then fixes the distribution function of ellipticities at a smoothing scale  $R$  for a void density contrast  $\delta_v$ . The authors suggest a value of  $\delta_v = 0.9$ , as we will see in modern implementations of void finding algorithms a value of  $\delta_v = 0.8$  is more common, however this choice is more or less arbitrary. The most important aspect of this analytical ellipticity distribution is its clear dependence on the cosmological parameters as shown by Figure 5.4. The cosmological parameters enter via  $\delta_v = \delta_v(z) = \frac{\delta_{v,0}}{D(z)}$  and  $\sigma_R(z) \propto \frac{\sigma_8}{D(z)}$

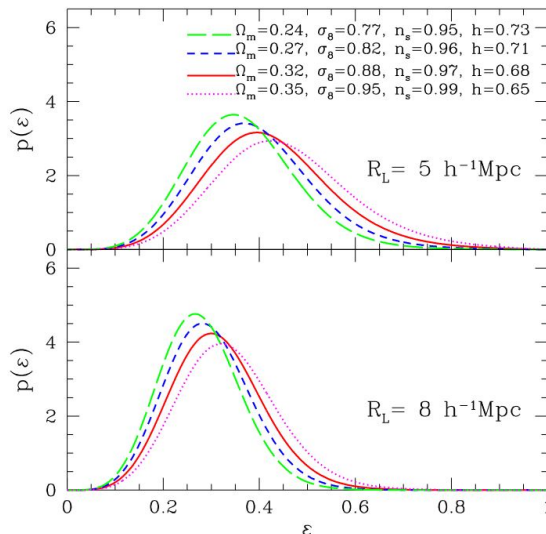


**Figure 5.4:** Ellipticity distributions calculated by Park & Lee (2007) (Figure 1) from their analytical model for different cosmological parameters. Top and bottom panel at two different smoothing scales.

because  $D(z) = D(z, \Omega_0, \Omega_\Lambda)$  in standard  $\Lambda$ CDM (Carroll et al., 1992).

## 5.6 These are(n't) the voids you're looking for: Void finding algorithms

Before we move on to analysing simulated voids, we need to establish how to find them. There is a wide variety of approaching the problem of finding voids in a given volume. Historically, the first split of methodologies was between algorithms that used the dark matter field directly (with an obvious orientation towards simulations) and those that used galaxies as tracers of the underlying density fields. A major problem of using haloes (or galaxies) as tracers is their occupation bias towards denser areas, diluting the information that can be extracted about the density field. As a result of numerous void oriented studies towards this problem, today void finders are often a hybrid between those two, allowing for more robust comparisons between observations and simulations by directly controlling for those biases. A second important distinction to make is between void finding algorithms that assume a specific shape and (geometric) parameter free void finders.

**Void finders based on spherical geometry** The former often assume a spherical void shape, are mostly intended for halo catalogues and essentially find the largest empty (empty in the sense of containing *no* haloes above a certain mass or luminosity threshold) sphere around centers pre-defined by some method (e.g. finding the most underdense particle in a box by sampling particles and their neighbours Brunino et al., 2007). An idea that takes this approach further was implemented by Hoyle & Vogeley (2002): Here the sample of haloes is split into void galaxies and wall galaxies based on their third-neighbor distances. The sample is then emptied of the void galaxies and the wall galaxies are binned into a regular grid. For every empty grid cell a sphere is grown until it touches a non-empty cell. The union of these spheres is then defined as a void. This algorithm already allows for a complex void structure, nevertheless the individual building blocks of the voids are still spherical.

**Tessellation based void finders** The next class of void finders make use of known mathematical methods for dividing a certain domain into geometrical subvolumes based on a set of sampling points (which in the case of void finding are the dark matter particles or haloes): The two most common way of doing this are the **Voronoi tessellation** and the **Delaunay triangulation**. Both are intimately related in the sense that one can be reconstructed from the other (mathematically speaking they are duals)(Ito, 2015). As a result both algorithms discussed here operate similarly. The *ZOBOV* (Zones Bordering On Voids) (Neyrinck, 2008) algorithm tessellates the volume into Voronoi cells of constant density based on the respective cell size. The *Watershed Void Finder* (Platen et al., 2007) leverages the Delaunay triangulation to apply a multi-dimensional linear interpolation to the constant Voronoi density values, giving a continuous field. Both methods then apply a watershed transform to merge the

obtained density depression zones into voids. This algorithm can be visually understood by invoking the picture of flooding a hilly landscape gradually with water. In this picture, the hills represent the overdensities and the valleys are the voids we are looking for. Initially

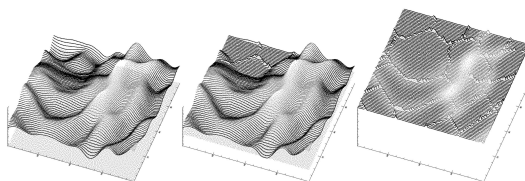


**Figure 5.5:** Qualitative picture of the Watershed transform. Depressions correspond to void zones. Figure 1 from (Platen et al., 2007)

there will be a very fragmented collection of small ponds. As the water rises the depressions separated by lower walls will gradually merge to form larger basins. In the extreme case of flooding everything, the water will have reached a single continuous surface. As this is generally not desirable in the context of void finding, the common practice is to assign a maximum water level (i.e. a maximum density a structure within a void can have to still be considered part of a single void as opposed to a wall between two smaller voids). Motivated by the considerations in section 5.2 this value is often set to  $0.2\bar{\rho}$  or, as we have seen before, the theoretical mean density of an isolated void. The void finder we are going to use for the analysis in the next chapter, *VIDE*, is based on the *ZOBOV* method outlined here.

**Dynamical void finders** Another method to identify voids is closely related to our observations in the introduction to chapter 4. There we considered the geometric setup of the velocity field. It was apparent that a void corresponds to a region where all streamlines diverge. In more formal terms this means that all eigenvalues of the tidal tensor (or the closely related velocity shear tensor) are negative in void regions, i.e. they are expanding along all three major axes. This can be used to classify void regions by discretizing the density or velocity field to a grid and then computing the respective tensor and its eigenvalues at every grid cell, connecting the cells with all negative eigenvalues to form voids.

## 5.7 Summing up: The end of the desert

In this chapter we have seen the other side of matter accumulating in the overdense regions. We have introduced voids with the simple model of a spherical underdensity expanding at a super-Hubble rate and deduced first important properties like the build up of matter at the edges and the time of shell crossing from this. Using the familiar method of exploiting the statistics of the Gaussian perturbation fields, we have derived typical void sizes and found a new way of looking at the intricate web structure of the cosmos as the small fraction of volume, where voids are *not*. From the emerging hierarchy of voids out of the statistics of the density perturbation field, we have seen that voids can have substructure in the form of relics from smaller voids merging, or being annexed, into larger voids. Voids also house

galaxies that are, due to their unique environments, important specimen for studies of galactic evolution. Adding another layer of complexity, we strayed from the isolated, increasingly spherical evolution of voids to more realistic conditions. From the statistics of the tidal fields (or more precisely their eigenvalues) we have seen how to arrive at an analytical description of the distribution of void ellipticities. The primary result was a clear functional relationship between these distribution functions and the cosmological parameters governing structure formation. In the following chapter we will focus on this aspect of void evolution. To introduce the methodology that the next chapter will be built on, we have finally reviewed some of the most important approaches to finding voids in density field samples. Now we can use all this to analyse voids in a fully hydrodynamical simulation, hoping to test the model and its feasibility against realistic conditions. If the model is robust against the full range of physics, it can offer a path to determining the cosmological parameters from observations independently from current methods and in the best case help break the degeneracies that continue to puzzle modern cosmology.

# Chapter 6

## Shaping up: Tracing cosmological parameters with void shapes

### 6.1 Nothing (else) matters: Void shapes and cosmology

Voids are used to solve problems on local and global scales in our universe. Among their qualities as statistically isotropic objects discussed in the introduction, their intrinsic properties have been found to be promising tracers of the dark energy equation of state (Bos et al., 2012) and the initial conditions (Park & Lee, 2007) in a standard  $\Lambda$ CDM cosmology. Most of these studies involve the  $\epsilon$ -parameter, which is defined as  $1 - \frac{a}{c}$ , where  $a$  and  $c$  are the largest and smallest ellipsoidal axes respectively. While the simplest analytical models expect these regions to become more spherical in shape – as we have seen in the theory – erasing any imprints of primordial asphericities, voids in simulations and observations alike have been demonstrated to be highly complex and aspherical in nature even at low redshifts. Figure 6.1 demonstrates this with a small volume sample of a collection of voids from the *Magneticum* suite of cosmological simulations. In the following chapter we will use this

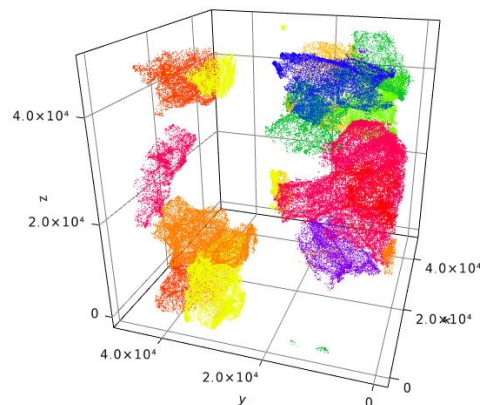


**Figure 6.1:** Example volume with void particles from simulation box4. The colors indicate the different voids. A  $40^3$  Mpc/h volume is shown, demonstrating the shapes produced by the VIDE void finder.

richness in shape to investigate the dependency of the large-scale geometry on cosmological initial conditions, following the path laid out by (Park & Lee, 2007). While the impact of baryonic physics is expected to be negligible on void scales, there are impacts at the low-size end, where the definition of a void becomes unclear and voids tend to be embedded in larger scale overdensities (Paillas et al., 2019). Therefore we will perform our studies in a fully hydrodynamical simulation box, to capture these effects as well.

## 6.2 Nothing is clear: Goals and questions

In the previous chapter we have seen the analytical derivation for the void ellipticity distribution and the effects that varying the cosmological initial conditions (within  $\Lambda$ CDM) has based on the Zel’dovich approximation. As this derivation is based on an approximation that is only valid until the quasi-linear regime (Hidding et al., 2014) a comparison to numerical simulation can verify its validity and possibly shed light on deviations from the model due to non-linear aspects of voids. Park & Lee (2007) already compared their model prediction to a cosmological simulation. It was the *Millennium* run (Springel et al., 2005), which showed good agreement to the model (Park & Lee, 2007). However this was a very limited comparison to only one set of cosmological parameters and a dark-matter-only cosmological box with relatively low resolution. Therefore it is worthwhile to revisit the relationship between ellipticity and cosmology in light of a modern simulation with full hydrodynamics and significantly higher resolution. In the following we will do just that: The question to answer will be to what extent the assumptions made by (Park & Lee, 2007) hold for voids in a universe with baryonic physics.

## 6.3 Nothing on my mind: Tools and Methods

To start working with voids the first and foremost task is to find them. As we have seen in the background chapter, there are a number of different approaches and tools to define these underdense domains. While these generally agree better than structure finding methods concerned with overdense structures (Libeskind et al., 2018), there are still differences between the methods that one has to keep in mind when comparing results obtained with different tools (Paillas et al., 2019) (owing to collaboration projects such as Colberg et al., 2008 there is however a quite extensive understanding of the differences between the different approaches). In the following analysis, I used the VIDE void finding suite (Sutter et al., 2014b) to extract the simulated voids.

### 6.3.1 VIDE setup

As discussed before, VIDE is based on the ZOBOV (Neyrinck, 2008) void finding algorithm. To summarize the discussion in the previous chapter, first the volume is Voronoi tessellated into zones of constant densities using the tracer particles. In our case, these are the dark

matter particles. The cell density is inversely proportional to the size of the cell. A watershed transform is then applied to the density field sampling obtained this way, merging adjacent depressions into voids. The merging threshold – in other words the maximum density the edges of a depression can have for it to still be merged with an adjacent depression – is essentially a user parameter. The construction of the void catalogs we are going to analyse in the following applies the standard value for the maximum wall height we can merge over:  $0.2\bar{\rho}$  (derived from the mean void density discussed in chapter 5). In this work only the top most voids in the hierarchy are used, disregarding sub-voids. I checked this method for consistency and including sub-voids does not alter results significantly (see Figure A.1). From the void zones and their volume (the sum of the individual Voronoi cell volumes) the effective radius is defined as  $R_{eff} = \left(\frac{3V}{4\pi}\right)^{1/3}$ . We will use this radius as the void radius in the following. The void ellipticity is computed by *VIDE* via the inertia tensor of all the particles in the void zone. From its eigenvalues the ellipticity  $\epsilon$  is then obtained by  $\epsilon = 1 - \frac{J_1}{J_3}$  where  $J_1$  and  $J_3$  represent, as before, the largest and smallest eigenvalue (or the shortest and longest ellipsoidal axis). To save performance and avoid sampling the field at small scales, it is common to apply a tracer sub-sampling before tessellating. This is implemented in the preprocessing framework of *VIDE* and reduces tracer count by randomly picking a fraction of all tracers. The sub-sampling I employed to obtain the void catalogs ensured a tracer density of  $4 * 10^{-3}/\text{Mpc} * h^{-1}$ , comparable to the sampling used by Sutter et al. (2013). This samples the density field still at a rather fine level, allowing in turn for relatively small voids. As the following sections show however, there are some interesting effects present at the low-size end of the catalogue, therefore I decided to leave those voids in. With the simulation resolution the effective minimal void size is 5 Mpc/h. Every Void catalog analysed in the following also has the standard *VIDE* density cut applied: Voids with central densities more than 20% of the mean density are disregarded as spurious.

### 6.3.2 Parameter Activity: The multi cosmology box from *Magneticum*

To probe the cosmology dependence of void shapes, we use a set of runs with varying cosmological parameters from *Magneticum*. Box1a provides such a suite of cosmological runs. With a box size of 896 Mpc and  $2 * 4536^3$  particles it is suited to produce both realistic large scale structure and adequate resolution for our analysis. To capture also the evolution of the voids, all analysis will be done with two snapshots,  $z = 0.0$  and  $z = 5.3$  respectively. The parameters that are varied between each run are: The critical fraction of total matter density,  $\Omega_0$ , the critical fraction of baryon density  $\Omega_b$ , the clustering (variance of the density field) of matter on the scale of 8 Mpc  $\sigma_8$ , the Hubble parameter  $H_0$  and the fraction of baryons  $f_b = \frac{\Omega_b}{\Omega_0}$ , which of course cannot be varied independently, but serves a good indicator to the ratio of the strength of baryonic effects to gravity. An overview of the different parameters is repeated in Table 6.1 from Table 2.1 for convenience:

run	$\Omega_0$	$\Omega_b$	$\sigma_8$	$H_0$	$f_b$
C1	0.153	0.0408	0.614	66.6	0.267
C2	0.189	0.0455	0.697	70.3	0.241
C3	0.200	0.0415	0.850	73.0	0.208
C4	0.204	0.0437	0.739	68.9	0.214
C5	0.222	0.0421	0.793	67.6	0.190
C6	0.232	0.413	0.687	67.0	0.178
C7	0.268	0.0449	0.721	69.9	0.168
C8	0.272	0.0456	0.809	70.4	0.168
C9	0.301	0.0460	0.824	70.7	0.153
C10	0.304	0.0504	0.886	74.0	0.166
C11	0.342	0.0462	0.834	70.8	0.135
C12	0.363	0.0490	0.884	72.9	0.135
C13	0.400	0.0485	0.650	67.5	0.121
C14	0.406	0.0466	0.867	71.2	0.115
C15	0.428	0.0492	0.830	73.2	0.115

**Table 6.1:** Parameters of the different runs in Box1a. All runs were performed with the same initial conditions.

### 6.3.3 Resulting void catalogs

For an overview of the sample sizes and the average properties of their voids, we provide Table 6.2. As can be seen from the table, both the mean ellipticity and the mean effective radius show variation for the different runs. This thesis focuses on the void shapes, but the stage is set for future research involving also the sizes and their variation. With the

run	$N_{voids}$	$\langle \epsilon \rangle$	$\langle R_{eff} \rangle$
C1	24306	0.156	14.35
C2	21920	0.158	14.96
C3	18096	0.162	15.67
C4	20974	0.160	15.19
C5	19486	0.160	15.47
C6	22224	0.157	14.95
C7	21389	0.157	15.15
C8	18672	0.159	15.82
C9	18968	0.159	15.74
C10	17399	0.161	15.97
C11	18962	0.159	15.73
C12	17796	0.159	15.99
C13	23564	0.154	14.80
C14	18334	0.158	15.94
C15	19272	0.158	15.77

**Table 6.2:** Overview of the void catalogs extracted at  $z = 0$  with most important properties

parameters set and the catalogs specified we can now investigate the impact of cosmology on void shapes:

run	$N_{voids}$	$\langle \epsilon \rangle$	$\langle R_{eff} \rangle$
C1	44158	0.147	12.04
C2	43663	0.148	12.10
C3	41906	0.147	12.21
C4	43046	0.148	12.14
C5	42986	0.147	12.15
C6	43989	0.147	12.08
C7	43570	0.147	12.11
C8	41210	0.147	12.32
C9	42295	0.147	12.19
C10	42242	0.147	12.21
C11	43107	0.147	12.12
C12	42796	0.147	12.20
C13	44757	0.146	12.07
C14	42804	0.147	12.17
C15	43895	0.146	12.17

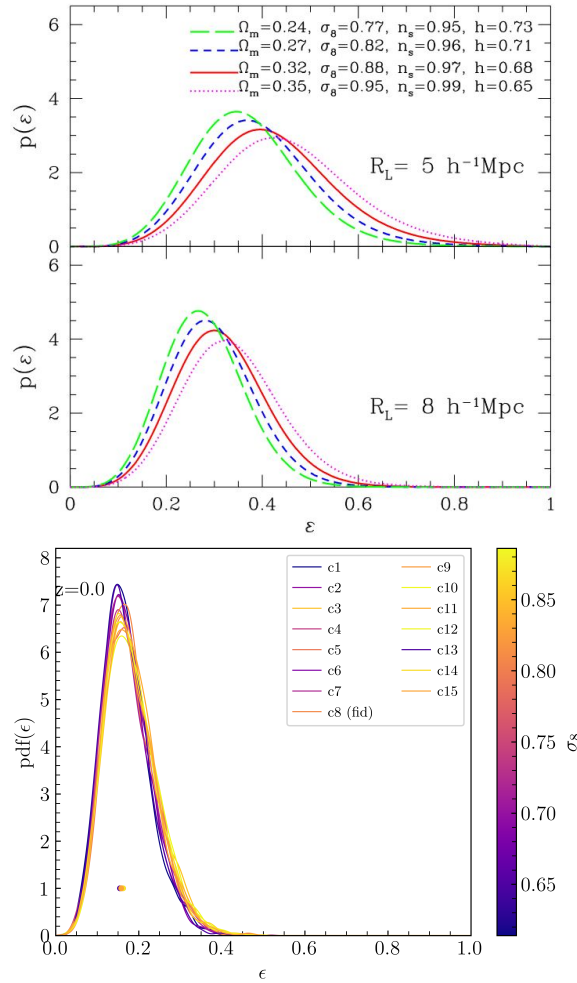
**Table 6.3:** Overview of the void catalogs extracted at  $z = 5.3$  with most important properties

## 6.4 The ellipticity distribution

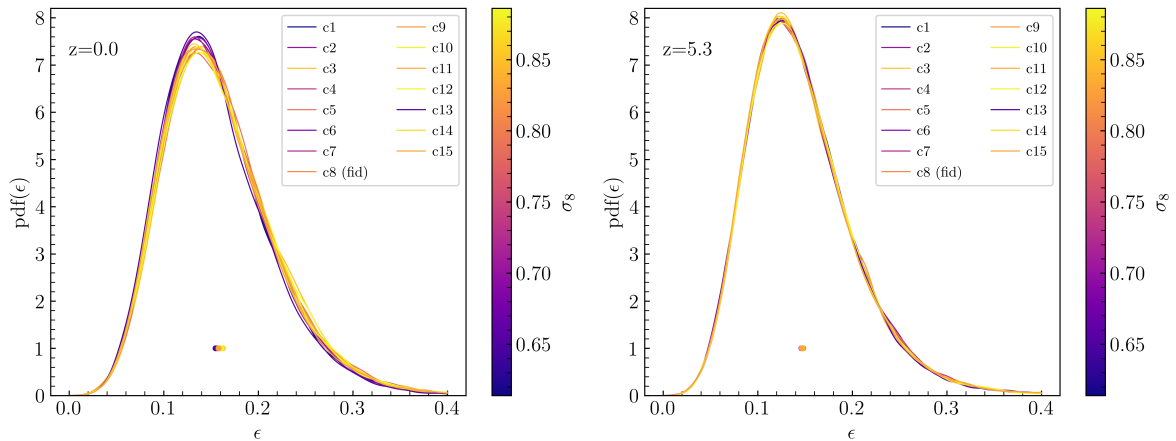
We compute the probability density distributions for each cosmology by first calculating histograms with equal bins  $N_{bin} = 500$  and then smoothing these histograms with a Gaussian kernel to obtain continuous curves.

**Limited comparison to the model** Figure 6.2 compares the ellipticity functions from *Magneticum* to those of the model. Notable is a significantly smaller mean ellipticity and a much more tight spread of the distribution when compared to the results and model of Park & Lee (2007). This is especially surprising since the void sizes in Park & Lee (2007) as well as Bos et al. (2012) match well with Table 6.2 overall. Further investigations are needed as to why the *Magneticum* voids appear to be so spherical. A direct comparison with the results of Park & Lee (2007) is further complicated by the fact that for the test set in that paper, the parameters are varied in a rather different fashion than for Box 1a. One example of this is that  $\sigma_8$  anti-correlates with  $H_0$  in the (Park & Lee, 2007) set, while in the *Magneticum* set, there is an 80% positive correlation between those parameters. A full comparison will necessitate calculating the model predictions for the full *Magneticum* set. Unfortunately we will have to leave this to future work. For now we will focus on the ellipticity functions obtained from the simulation and compare trends to the findings of (Park & Lee, 2007) where appropriate.

**Ellipticities of the full sample** Figure 6.3 shows the total ellipticity distribution for all voids in each cosmology. The impact of cosmology is seen, albeit significantly smaller than the model predicts. A possible reason is the influence of baryonic physics, which should have the strongest influence at the low size end. From the colors of the curves, one can deduce that cosmologies with lower  $\sigma_8$  parameters peak at lower ellipticities, i.e. an increase in this parameter gives more elliptical voids in general. Ellipticities are more pronounced at

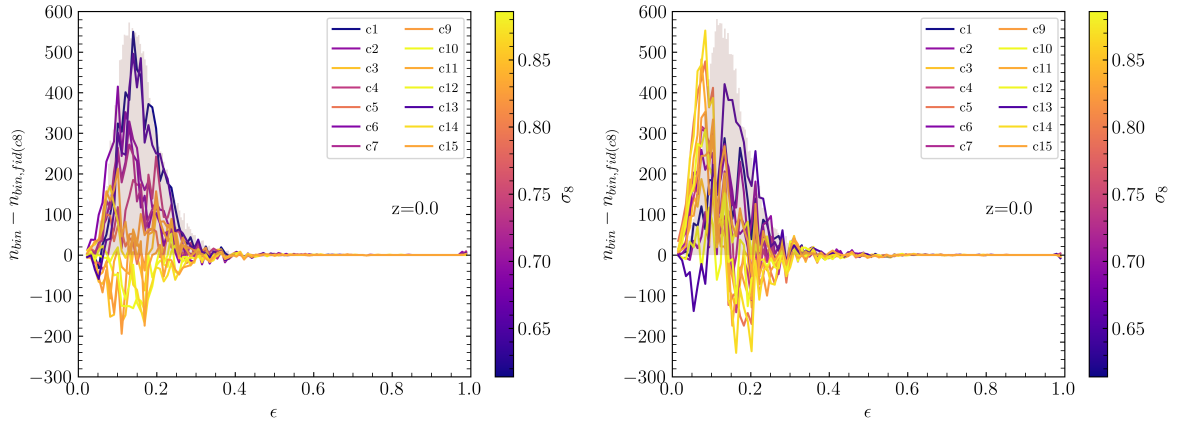


**Figure 6.2:** Ellipticity distributions from the (Park & Lee, 2007) model compared to the *Magneticum* results. To maximize comparability, a single radial bin with  $\langle R_{eff} \rangle = 10 \text{ Mpc}$  was used for each cosmology. This corresponds to the upper panel from the model with  $R_L = 5 \text{ Mpc}$ , following the formula given in (Park & Lee, 2007) for computing the smoothing radius from the mean void radius of a bin:  $R_L = (1 + \delta_v)^{1/3} R_{eff}$  (where  $\delta_v = -0.9$  was assumed).



**Figure 6.3:** Ellipticity distributions for the different cosmologies at two redshifts. The mean of each curve is overplotted below the curve. The colors indicate the  $\sigma_8$  parameter of the cosmologies.

later times, contradicting the linear paradigm of voids growing more spherical in time, but in line with more detailed theoretical expectations (Park & Lee, 2007, Lee & Park, 2009, Bos et al., 2012). As the matter distribution evolves, the differences between the cosmologies grow significantly stronger. To quantify those differences, we can consider the deviations from the fiducial model. For this we bin the ellipticity distributions for the different runs into histograms of 100 bins respectively. At each bin center and for each cosmology, the difference between the respective histogram and the fiducial histogram is then computed. The resulting difference plot is shown in Figure 6.4: The deviations confirm what was already hinted at in



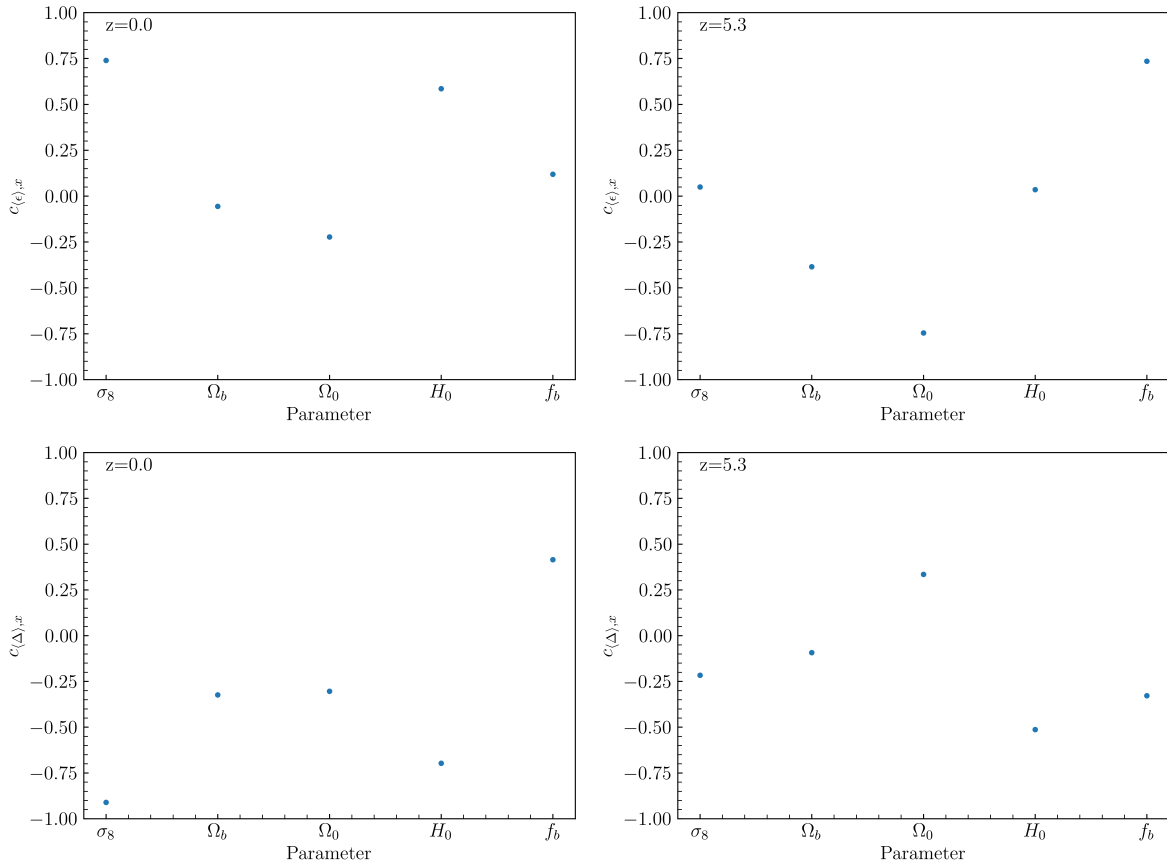
**Figure 6.4:** Absolute ellipticity distribution deviations from the fiducial distribution. The shape of the fiducial distribution is indicated by the grey histogram in the background (not to scale).

Figure 6.3. The largest deviations from the fiducial model can be seen for the cosmologies with the lowest  $\sigma_8$ . The smaller deviations in the pdf in Figure 6.3 at higher redshift appear to be caused by the larger number of voids in the high redshift sample, since the deviation amplitudes are of the same order of magnitude as in the low redshift set. The coloring of the cosmologies by  $\sigma_8$  indicate that the deviations are not as influenced by this parameter at high redshift as they appear to be at low redshift, showing a much clearer trend in the left panel of Figure 6.4 compared to the right panel.

To try and deconvolve the influences of the individual parameters as best we can, we will now study how strongly these parameters correlate with the shape of the ellipticity distribution. We will use two parameters to characterize the distribution, the mean ellipticity  $\langle \epsilon \rangle$  and the mean absolute deviation (per bin) of a given cosmologies' distribution from the fiducial cosmology (c8), which we will call  $\langle \Delta \rangle$ . The latter is for each cosmology the average of the deviation amplitudes shown in Figure 6.4. To quantify their influence on the void shapes I compute for each of the cosmological parameters  $\{\sigma_8, \Omega_b, \Omega_0, H_0, f_b\}$  the **pairwise Pearson correlation coefficient** w.r.t.  $\langle \epsilon \rangle$  and  $\Delta$  given by

$$c_{X,Y} = \frac{\langle (X - \langle X \rangle)(Y - \langle Y \rangle) \rangle}{\sigma_X \sigma_Y}. \quad (6.1)$$

Figure 6.5 outs  $\sigma_8$  as the main cause of deviation from the fiducial. Interestingly, this is not the case at  $z=5.3$ , where this parameter does not correlate with deviations *at all*. In general there are no strong correlations between the deviations from the fiducial and the parameters



**Figure 6.5:** Correlation coefficients of the parameters with the mean absolute deviation from the fiducial ellipticity distribution

at high redshift, confirming the picture presented in Figure 6.4. So the tidal fields from the clustering of the matter around the voids apparently only become important later on, as the overdensity are enhanced by their accretion of matter. The correlations with the mean draw a surprising picture: Once again, the mean shows a relatively strong positive correlation with  $\sigma_8$ , which is physically intuitive, since the stronger the clustering of matter is, the steeper is the force gradient at the void walls and thus the stronger the tidal fields distorting them. Contrary to the expectations of Park & Lee (2007), at late times the data indicate a positive relationship between  $H_0$  and  $\langle \epsilon \rangle$ . This runs counter to the picture of a faster expansion evening out ellipticities more effectively. A reason for this might be the so-called void bias: The smaller voids that drive the ellipticities are generally found in less underdense regions (Sheth & Tormen, 2004) with a consequently weaker local expansion rate and dominating tidal fields, dampening the effect of an overall faster expansion. An alternative explanation is entirely unphysical in nature: Box1a co-varies  $H_0$  very strongly with  $\sigma_8$  with  $c_{H_0, \sigma_8} = 0.83$ , so another cause for this could just be the stronger dependency of the mean on  $\sigma_8$  causing this puzzling discrepancy. Surprisingly the "tug-of-war" image with the expansion parametrized by  $H_0$  erasing ellipticity and the tidal fields from  $\Omega_0$  competing with this effect invoked by Park & Lee (2007) also fails to manifest in terms of the matter density:  $\Omega_0$  shows an anti-correlation early on and almost none at late times. This seems to indicate that it is more the configuration of mass than the abundance early on determining the local effects tidal fields

have on the void shapes. Another notable observation is the strong influence of the baryon fraction at early times, while it seems rather unimportant for the void shapes at late times. This indicates that as voids grow, baryonic physics become less important to their shapes and would indicate that baryonic physics renders voids even more elliptical early on. It might also offer up an alternative explanation for the initially negative correlation of the overall matter density: Baryon fraction and overall matter density are varied almost exactly opposite ( $c_{\Omega_0, f_b} = -0.95364797$ ) and the baryon fraction has a strongly positive correlation with mean ellipticities early on. So this counter-intuitive influence of the overall matter density might again be caused by its variation with another parameter with a strong influence early on. Overall a more focused variation of the cosmological parameters in the future might help shed further light on which of these intriguing correlations are truly of physical nature. It is at this point hard to discern the effects of this specific variation of parameters from physical effects. Very clear is that the ellipticity function is influenced by many different cosmological factors, making a follow-up critical.

## 6.5 The big nothing: Void size and ellipticity

It is generally expected that voids are more irregular the smaller they get because smaller voids tend to be found in less underdense regions than bigger voids (dubbed the *Void bias* (Sheth & Tormen, 2004)). As a result, smaller voids experience stronger tidal fields at their boundaries. The radius-ellipticity relation in Figure 6.6 plots the individual void ellipticities

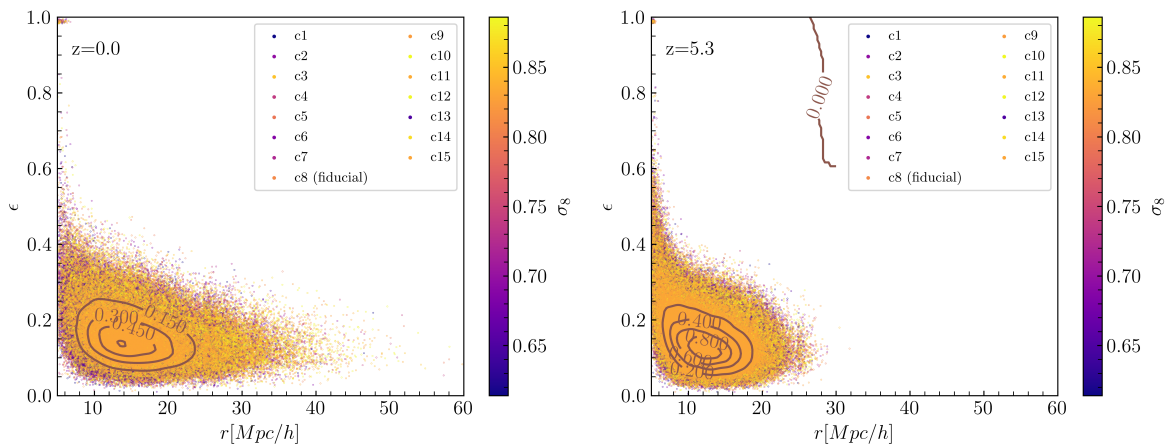


**Figure 6.6:** Effective Radius-ellipticity distribution. The contours indicate the percentiles of the fiducial model. A negative shape to radius correlation can be seen.

against their radii and visualizes nicely how the voids grow over time via expansion and merging. Given the trend of ellipticities increasing with time shown in Figure 6.3, it is interesting to see how the high-ellipticity voids still present at  $z=5.3$  seem to vanish for most cosmologies as the cosmic web evolves. This trend is somehow *overcompensated* by the general ellipticity of mid-size voids increasing, as is evident by the contour shifting upward and to the right. This suggests that small and high-ellipticity voids constitute a relatively small fraction of the total population. As these outliers evolve, they either merge

with other voids, are squeezed out by surrounding overdensities, or grow to become more spherical. The *void-in-cloud* process is significantly more likely at the small-size end of the void population, since larger underdensities need even larger overdensities enclosing them in order to be squeezed out (Sheth & van de Weygaert, 2004). A weak negative correlation of size to ellipticity can be found, aligned with previous investigations (Pisani et al., 2015) and the theoretical considerations discussed in chapter 5. To answer the question how the shape evolution depends on the void size, I binned the voids by radii and plotted the ellipticity distribution for each cosmology at each bin: In Figure 6.7 (upper panels) the differences

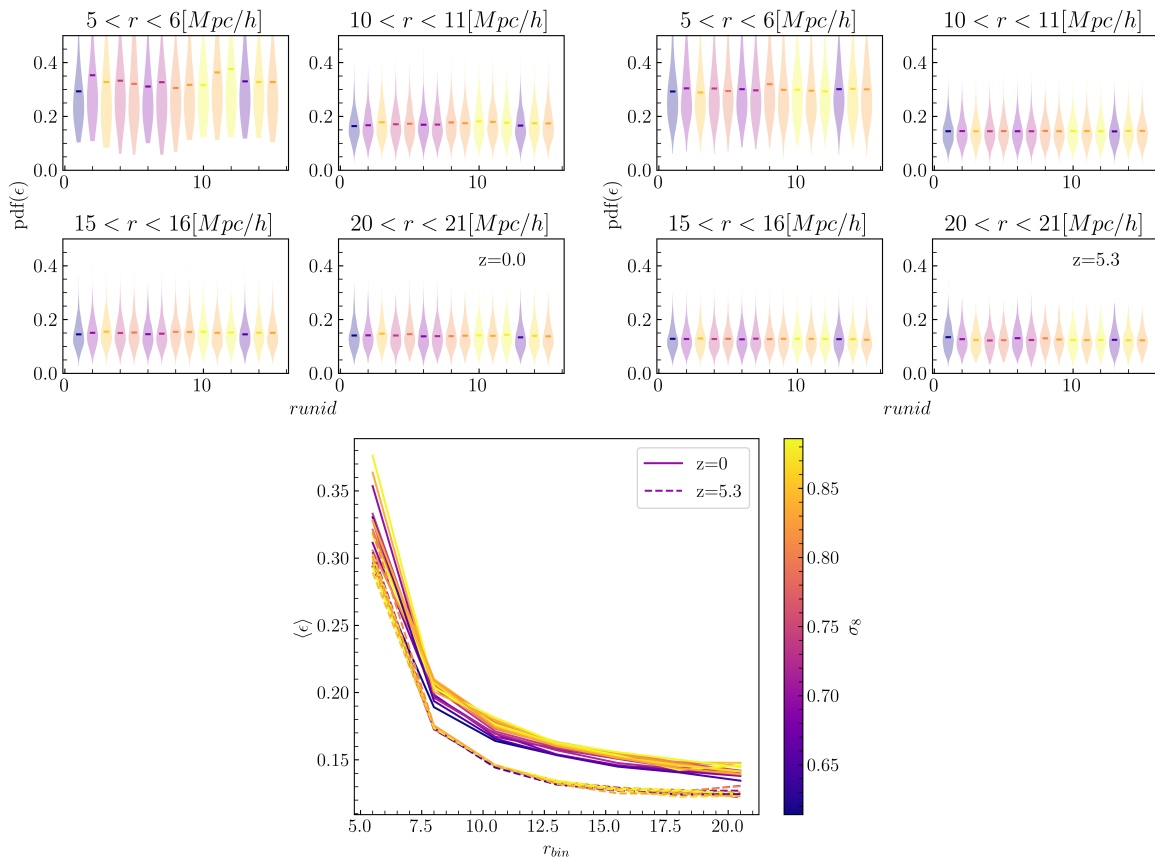


**Figure 6.7:** (Upper panels): Ellipticity distribution for each cosmology at four radial bins. The bars indicate the means of the distributions. (Lower panel) The mean of each cosmology connected between the radial bins. Both snapshots are shown with the line style indicating redshift.

between the cosmologies appear most pronounced for small voids. While the larger voids stay aligned with regards to their shapes, the shift that drives the overall distribution to more elliptical shapes can clearly be seen. This is most likely at least in part due to the high- $\epsilon$  voids growing and thus entering a higher  $r$ -bin, but cannot be wholly explained by this. Voids growing more elliptical in the tidal fields of their environments is a possible explanation for this additional total shift of ellipticities. The radial ellipticity profiles (lower panel) for the individual cosmologies demonstrate the negative relationship between ellipticity and radius seen in Figure 6.6 once more. A narrowing of the cosmological spread at larger radii indicates that it is indeed the smaller voids that are mainly driving the differences between cosmologies.

## 6.6 The shape of nothing: Conclusions

We have explored the connection between void shapes and the underlying cosmology with the help of 15 multi-cosmology runs. We confirmed the pronounced dependency of void shapes on the cosmological parameters derived from theory earlier. This makes real-space shape analysis a promising candidate for an independent derivation of these parameters from observations. The parameter with the most apparent impact on how spherical the *Magneticum* voids are was found to be  $\sigma_8$  with the general trend being an increase of deviations from sphericity with an increase of clustering on the scale of 8 Mpc. Other parameters do not show very clear correlations, with notably  $H_0$  directly contradicting physical expectations from (Park & Lee, 2007). A follow up study will be needed to shed more light on these correlations and possibly rule out systematics due to co-variation of certain parameters. Interestingly, analysing the distributions at two different redshifts showed that cosmology-induced differences between the ellipticity distributions are significantly smaller at early times compared to lower redshifts. Combined with an overall increase in mean ellipticity, which also appears to be robust to variations in the cosmological parameters, this implies that the observed cosmological variances increase along with the mean ellipticities. At this point we can make no statement about numerical effects arising due to multiple runs with the same seed, which can be an issue. A follow up investigation would be helpful here to properly separate the proper cosmology influences from purely numerical effects.



# Chapter 7

## Weaving it all together: Conclusions

This work has been dedicated to the two most fundamental building blocks of the cosmic web and the influence of baryonic physics on them. The first part focused on the matter rich regions in the universe and the galaxies and clusters that populate them, while the second part turned to the vast and underdense voids. To study the physics that shape and govern these regions in great detail and free from observational biases, we used state-of-the-art cosmological simulations with full hydrodynamics from the *Magneticum* suite. In the first part special attention was given to the accretion velocity fields and the outflows the baryonic interactions can give rise to in the outskirts of haloes. A large mass range of haloes ( $10^{12} - 10^{15} M_{\odot}/h$ ) was selected.

It was shown that, while in general galaxies and clusters cannot be considered scaled versions of each other, the accretion processes in their outskirts exhibit an astounding self-similarity. The scaled radial sampling from  $1.2 - 5r_{vir}$  that was employed demonstrated this to hold at every stage of accretion. Comparisons to the predictions of a semi-analytic model (van den Bosch, 2002) built on the paradigm of hierarchical structure formation demonstrated a good agreement despite the additional physics. Accretion processes are largely dominated by gravity however and the self-similarity was found to be broken once the baryonic physics become more important: The hot ( $T \approx 10^8 K$ ) gaseous outflows driven predominantly by thermal effects demonstrate a clear schism between galaxies and clusters at large radii, hinting at possible different driving mechanisms or environmental influences for these outflows. Around galaxy clusters, these outflows were found to be less extended, with the general radial profiles consistent with the model of shock driven outflows. Meanwhile galactic outflows persist to larger radii, indicating either different outflow driving mechanisms or different environmental conditions. A final verdict is left as an open question to future investigation.

While the mass flow rates are not consistent between galaxy and cluster outflows, they share a similar spatial distribution: Inflows were shown to mostly be concentrated in dense and colder filaments (which still contained significant amounts of gas in the warm phase  $T \approx 10^6 K$ ), while the outflowing gas is hotter, more diffuse and more homogeneously spread across the outskirts, in general agreement with expectations (Gouin et al., 2022). Based

on this picture the duality between dark matter (gravity) dominated physics and baryonic (pressure dominated) physics is demonstrated quite clearly.

A detailed investigation of the enrichment history of outflowing gas in cluster outskirts resulted in a rather unambiguous confirmation of our initial suspicions: The outflowing gas is most likely both pre-heated and enriched at early times in the filaments by their internal dynamics. At the cluster border this pre-enriched gas is then redistributed by the shocks and remains cut off from further enrichment and dilution.

On the losing side of the accretion balance a clear dependence of void shapes on the cosmological parameters was demonstrated in a fully hydrodynamical simulation set. This confirms theoretical considerations built on a dark matter only model (Park & Lee, 2007) (and before only tested against dm-only evolution) and implicates real-space void shapes as a candidate for independent measurements of these parameters, desperately needed to resolve the current tensions between methodologies. Deviations from the theoretical expectations manifested themselves in so far as the main driver of void asphericities seems to be the initial clustering of matter,  $\sigma_8$  (instead of the balance between expansion  $H_0$  and matter density  $\Omega_0$  as suggested by (Park & Lee, 2007)). If this can be confirmed in future studies, it has the potential to offer a path towards resolving the " $\sigma_8$  tension".

Analysing the void shapes at different timesteps has proven the voids to grow more elliptical in time, contradicting the simple model of isolated voids evolving towards a spherical shape. This is in alignment with expectations for voids in realistic environments however, as the local tidal effects grow in relative strength to the expansion of the void as matter becomes increasingly organized. Additionally this explains the observation that the differences between cosmologies increase from high redshifts to low redshifts. A parameter by parameter analysis indicated that baryonic effects are important only at high redshifts, while showing almost no impact on present day shapes. There appears to be a transition in the evolution of voids, after which they are too large to be significantly impacted by baryons. When exactly this takes place and the implications for structure formation will be investigated in future work.

To take a step back, one of the essential statements of these results is that the importance of baryonic effects undergoes exactly contrary evolution in voids and haloes: As the voids expand with time, the influence of baryons is quickly waning, while the compression in haloes enhances baryonic effects at the borders. As a result, we see almost no baryonic influences on the void shapes at late times, while the gas outflows of clusters and galaxies are almost entirely caused by the collisionality of the baryonic gas. Given what we have learned from both very overdense and very underdense regions, it has once again been demonstrated, that a complete picture of structure formation needs to implement both extremes consistently. Future simulations, implementing yet more detailed physics but also a further developed theory of structure formation will, in combination with comparisons to the state-of-the-art observations of today, be integral in forwarding our understanding of the universe from galaxy to superstructure scale and how these regimes connect.

# Appendix A

## Parents vs. children: Impact of the void hierarchy

As a sanity check I computed the ellipticity distribution for a catalog with subvoids included: No significant impact on the distributions is seen, making the choice most likely irrelevant in this specific scenario.

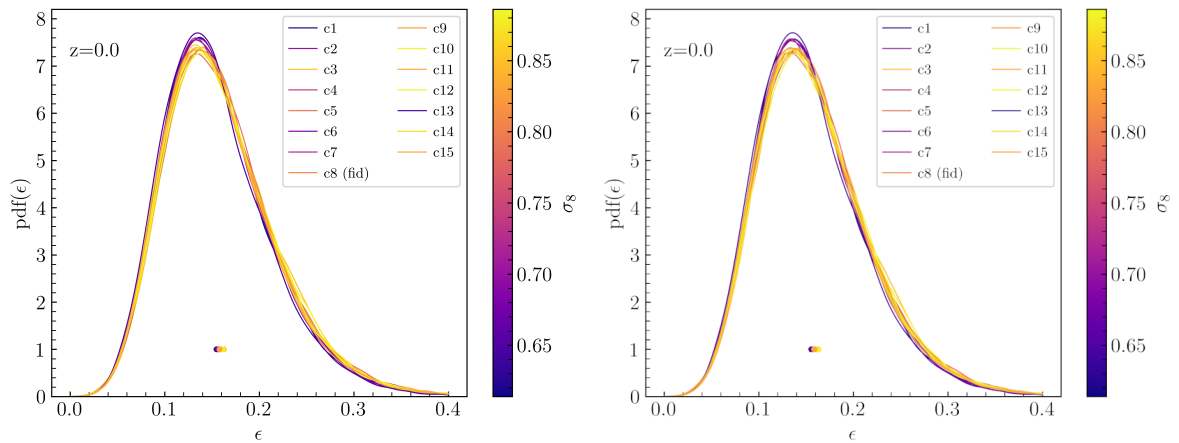


**Figure A.1:** Comparison of the void sample without subvoids (left panel) and with subvoids (right panel)



# References

- Andreon, S. (2010). The stellar mass fraction and baryon content of galaxy clusters and groups: Stellar mass fraction and baryon content. *Monthly Notices of the Royal Astronomical Society*, 407(1), 263–276.
- Barnes, J., & Hut, P. (1986). A hierarchical  $O(N \log N)$  force-calculation algorithm. *Nature*, 324(6096), 446–449.
- Bartelmann, M., Feuerbacher, B., Krüger, T., Lüst, D., Rebhan, A., & Wipf, A. (2014). *Theoretische Physik*. Springer-Verlag.
- Bertschinger, E. (1985). Self-similar secondary infall and accretion in an Einstein-de Sitter universe. *The Astrophysical Journal Supplement Series*, 58, 39–65.
- Blumenthal, G. R., da Costa, L. N., Goldwirth, D. S., Lecar, M., & Piran, T. (1992). The largest possible voids. *The Astrophysical Journal*, 388, 234.
- Böhringer, H., Dolag, K., & Chon, G. (2012). Modelling self-similar appearance of galaxy clusters in X-rays. *Astronomy & Astrophysics*, 539, A120.
- Bond, J. R., Cole, S., Efstathiou, G., & Kaiser, N. (1991). Excursion Set Mass Functions for Hierarchical Gaussian Fluctuations. *The Astrophysical Journal*, 379, 440.
- Bond, J. R., Kofman, L., & Pogosyan, D. (1996). How Filaments are Woven into the Cosmic Web. *Nature*, 380(6575), 603–606.
- Bos, E. G. P., van de Weygaert, R., Dolag, K., & Pettorino, V. (2012). The darkness that shaped the void: Dark energy and cosmic voids. *Monthly Notices of the Royal Astronomical Society*, 426, 440–461.
- Brecht, B. (1964). *Der gute Mensch von Sezuan..* Suhrkamp Verlag.
- Brunino, R., Trujillo, I., Pearce, F. R., & Thomas, P. A. (2007). The orientation of galaxy dark matter haloes around cosmic voids. *Monthly Notices of the Royal Astronomical Society*, 375(1), 184–190.
- Carroll, S. M., Press, W. H., & Turner, E. L. (1992). The cosmological constant. *Annual Rev. Astron. Astrophys.*, Vol. 30, p. 499-542 (1992), 30, 499.

- Castello, S., Högåås, M., & Mörtzell, E. (2022). A Cosmological Underdensity Does Not Solve the Hubble Tension. *Journal of Cosmology and Astroparticle Physics*, 2022(07), 003.
- Colberg, J. M., Pearce, F., Foster, C., Platen, E., Brunino, R., Neyrinck, M., Basilakos, S., Fairall, A., Feldman, H., Gottloeber, S., Hahn, O., Hoyle, F., Mueller, V., Nelson, L., Plionis, M., Porciani, C., Shandarin, S., Vogeley, M. S., & van de Weygaert, R. (2008). The Aspen–Amsterdam Void Finder Comparison Project. *Monthly Notices of the Royal Astronomical Society*, 387(2), 933–944.
- Cui, W., & Zhang, Y. (2017). The Impact of Baryons on the Large-Scale Structure of the Universe.  
URL <https://arxiv.org/abs/1708.02644v3>
- de Plaa, J., Werner, N., Bleeker, J. A. M., Vink, J., Kaastra, J. S., & Méndez, M. (2007). Constraining supernova models using the hot gas in clusters of galaxies. *Astronomy & Astrophysics*, 465(2), 345–355.
- Dodelson, S., & Schmidt, F. (2021). Initial conditions. In *Modern Cosmology*, (pp. 157–194). Elsevier.
- Dolag, K. (2022). Magneticum homepage. last accessed:2022-09-05.  
URL <http://www.magneticum.org/simulations.html>
- Dolag, K., Borgani, S., Murante, G., & Springel, V. (2009). Substructures in hydrodynamical cluster simulations. *Monthly Notices of the Royal Astronomical Society*, 399(2), 497–514.
- Dolag, K., Hansen, F. K., Roncarelli, M., & Moscardini, L. (2005). The imprints of local superclusters on the Sunyaev-Zel’dovich signals and their detectability with Planck. *Monthly Notices of the Royal Astronomical Society*, 363, 29–39.
- Dolag, K., Mevius, E., & Remus, R.-S. (2017). Distribution and Evolution of Metals in the Magneticum Simulations. *Galaxies*, 5(3), 35.
- Doroshkevich, A. G. (1970). Spatial structure of perturbations and origin of galactic rotation in fluctuation theory. *Astrophysics*, 6, 320–330.
- Fakhouri, O., Ma, C.-P., & Boylan-Kolchin, M. (2010). The merger rates and mass assembly histories of dark matter haloes in the two Millennium simulations. *Monthly Notices of the Royal Astronomical Society*, 406, 2267–2278.
- Fortuné, S. (2022). *Spin Evolution of Galaxies in the Magneticum Pathfinder Simulations*. Master’s thesis, LMU, Munich.
- Friedman, A. (1922). Über die Krümmung des Raumes. *Zeitschrift für Physik*, 10(1), 377–386.

- Gorski, K. M., Hivon, E., Banday, A. J., Wandelt, B. D., Hansen, F. K., Reinecke, M., & Bartelmann, M. (2005). HEALPix: A Framework for High-Resolution Discretization and Fast Analysis of Data Distributed on the Sphere. *The Astrophysical Journal*, 622(2), 759–771.
- Gouin, C., Gallo, S., & Aghanim, N. (2022). Gas distribution from clusters to filaments in IllustrisTNG. *Astronomy & Astrophysics*, 664, A198.
- Gunn, J. E., & Gott, J. R., III (1972). On the Infall of Matter Into Clusters of Galaxies and Some Effects on Their Evolution. *The Astrophysical Journal*, 176, 1.
- Guth, A. H. (1981). Inflationary universe: A possible solution to the horizon and flatness problems. *Physical Review D*, 23(2), 347–356.
- Halle, A., & Combes, F. (2013). Influence of baryonic physics in galaxy simulations: - A semi-analytic treatment of the molecular component. *Astronomy & Astrophysics*, 559, A55.
- Hamaus, N., Pisani, A., Choi, J.-A., Lavaux, G., Wandelt, B. D., & Weller, J. (2020). Precision cosmology with voids in the final BOSS data. *Journal of Cosmology and Astroparticle Physics*, 2020(12), 023–023.
- Harrison, E. R. (1970). Fluctuations at the Threshold of Classical Cosmology. *Physical Review D*, 1(10), 2726–2730.
- Hawking, S. W. (1982). The development of irregularities in a single bubble inflationary universe. *Physics Letters B*, 115(4), 295–297.
- Heinrich, A. M., Chen, Y.-H., Heinz, S., Zhuravleva, I., & Churazov, E. (2021). Constraining black hole feedback in galaxy clusters from X-ray power spectra. *Monthly Notices of the Royal Astronomical Society*, 505(3), 4646–4654.
- Hidding, J., Shandarin, S. F., & van de Weygaert, R. (2014). The Zel’dovich approximation: Key to understanding cosmic web complexity. *Monthly Notices of the Royal Astronomical Society*, 437, 3442–3472.
- Hidding, J., van de Weygaert, R., & Shandarin, S. (2016). The Zeldovich & Adhesion approximations, and applications to the local universe.  
URL <http://arxiv.org/abs/1611.01221>
- Hirschmann, M., Dolag, K., Saro, A., Bachmann, L., Borgani, S., & Burkert, A. (2014). Cosmological simulations of black hole growth: AGN luminosities and downsizing. *Monthly Notices of the Royal Astronomical Society*, 442, 2304–2324.
- Hoyle, F., & Vogeley, M. S. (2002). Voids in the Point Source Catalogue Survey and the Updated Zwicky Catalog. *The Astrophysical Journal*, 566, 641–651.

- Icke, V. (1984). Voids and filaments. *Monthly Notices of the Royal Astronomical Society*, 206(1), 1P–3P.
- Ito, Y. (2015). Delaunay Triangulation. In B. Engquist (Ed.) *Encyclopedia of Applied and Computational Mathematics*, (pp. 332–334). Berlin, Heidelberg: Springer.
- Kimmig, L. C. (2022). *Are You Bound or Just Projected? The Behavior of Substructures From Expansion to Galaxy Clusters*. Master's thesis, LMU, Munich.
- Klypin, A. A., & Shandarin, S. F. (1983). Three-dimensional numerical model of the formation of large-scale structure in the Universe. *Monthly Notices of the Royal Astronomical Society*, 204(3), 891–907.
- Kobayashi, C., Karakas, A. I., & Lugaro, M. (2020). The Origin of Elements from Carbon to Uranium. *The Astrophysical Journal*, 900(2), 179.
- Komatsu, E., Smith, K. M., Dunkley, J., Bennett, C. L., Gold, B., Hinshaw, G., Jarosik, N., Larson, D., Nolta, M. R., Page, L., Spergel, D. N., Halpern, M., Hill, R. S., Kogut, A., Limon, M., Meyer, S. S., Odegard, N., Tucker, G. S., Weiland, J. L., Wollack, E., & Wright, E. L. (2011). Seven-Year Wilkinson Microwave Anisotropy Probe (WMAP) Observations: Cosmological Interpretation. *The Astrophysical Journal Supplement Series*, 192(2), 18.
- Lee, J., & Park, D. (2009). Constraining the Dark Energy Equation of State with Cosmic Voids. *The Astrophysical Journal*, 696(1), L10–L12.
- Libeskind, N. I., van de Weygaert, R., Cautun, M., Falck, B., Tempel, E., Abel, T., Alpaslan, M., Aragón-Calvo, M. A., Forero-Romero, J. E., Gonzalez, R., Gottlöber, S., Hahn, O., Hellwing, W. A., Hoffman, Y., Jones, B. J. T., Kitaura, F., Knebe, A., Manti, S., Neyrinck, M., Nuza, S. E., Padilla, N., Platen, E., Ramachandra, N., Robotham, A., Saar, E., Shandarin, S., Steinmetz, M., Stoica, R. S., Sousbie, T., & Yepes, G. (2018). Tracing the cosmic web. *Monthly Notices of the Royal Astronomical Society*, 473(1), 1195–1217.
- Maggiore, M., & Riotto, A. (2010). THE HALO MASS FUNCTION FROM EXCURSION SET THEORY. I. GAUSSIAN FLUCTUATIONS WITH NON-MARKOVIAN DEPENDENCE ON THE SMOOTHING SCALE. *The Astrophysical Journal*, 711(2), 907–927.
- Markevitch, M., & Vikhlinin, A. (2007). Shocks and cold fronts in galaxy clusters. *Physics Reports*, 443(1), 1–53.
- Mukhanov, V. (2005). *Physical Foundations of Cosmology*. Cambridge: Cambridge University Press.
- Neyrinck, M. C. (2008). ZOBOV: A parameter-free void-finding algorithm. *Monthly Notices of the Royal Astronomical Society*, 386(4), 2101–2109.

- Nguyen, D. D., & Thompson, T. A. (2022). Galactic winds and bubbles from nuclear starburst rings.  
URL <http://arxiv.org/abs/2205.13465>
- Paillas, E., Cautun, M., Li, B., Cai, Y.-C., Padilla, N., Armijo, J., & Bose, S. (2019). The Santiago-Harvard-Edinburgh-Durham void comparison II: Unveiling the Vainshtein screening using weak lensing. *Monthly Notices of the Royal Astronomical Society*, *484*, 1149–1165.
- Papovich, C., Kawinwanichakij, L., Quadri, R. F., Glazebrook, K., Labbé, I., Tran, K.-V. H., Forrest, B., Kacprzak, G. G., Spitler, L. R., Straatman, C. M. S., & Tomczak, A. R. (2018). The Effects of Environment on the Evolution of the Galaxy Stellar Mass Function. *The Astrophysical Journal*, *854*(1), 30.
- Park, D., & Lee, J. (2007). Void Ellipticity Distribution as a Probe of Cosmology. *Physical Review Letters*, *98*(8), 081301.
- Penzias, A. A., & Wilson, R. W. (1965). A Measurement of Excess Antenna Temperature at 4080 Mc/s. *The Astrophysical Journal*, *142*, 419–421.
- Pisani, A., Sutter, P. M., & Wandelt, B. D. (2015). Mastering the effects of peculiar velocities in cosmic voids.  
URL <http://arxiv.org/abs/1506.07982>
- Planck Collaboration (2020). Planck 2018 results. VI. Cosmological parameters. *A&A*, *641*, A6.
- Platen, E., Van De Weygaert, R., & Jones, B. J. T. (2007). A cosmic watershed: The WVF void detection technique. *Monthly Notices of the Royal Astronomical Society*, *380*(2), 551–570.
- Press, W. H., & Schechter, P. (1974). Formation of Galaxies and Clusters of Galaxies by Self-Similar Gravitational Condensation. *The Astrophysical Journal*, *187*, 425–438.
- Riess, A. G., Filippenko, A. V., Challis, P., Clocchiatti, A., Diercks, A., Garnavich, P. M., Gilliland, R. L., Hogan, C. J., Jha, S., Kirshner, R. P., Leibundgut, B., Phillips, M. M., Reiss, D., Schmidt, B. P., Schommer, R. A., Smith, R. C., Spyromilio, J., Stubbs, C., Suntzeff, N. B., & Tonry, J. (1998). Observational Evidence from Supernovae for an Accelerating Universe and a Cosmological Constant. *The Astronomical Journal*, *116*(3), 1009–1038.
- Rost, A., Kuchner, U., Welker, C., Pearce, F., Stasyszyn, F., Gray, M., Cui, W., Dave, R., Knebe, A., Yepes, G., & Rasia, E. (2021). The threehundred: The structure and properties of cosmic filaments in the outskirts of galaxy clusters. *Monthly Notices of the Royal Astronomical Society*, *502*(1), 714–727.

- Santoro, F., Tadhunter, C., Baron, D., Morganti, R., & Holt, J. (2020). AGN-driven outflows and the AGN feedback efficiency in young radio galaxies. *Astronomy & Astrophysics*, *644*, A54.
- Schuster, N., Hamaus, N., Pisani, A., Carbone, C., Kreisch, C. D., Pollina, G., & Weller, J. (2019). The bias of cosmic voids in the presence of massive neutrinos. *Journal of Cosmology and Astroparticle Physics*, *2019*(12), 055–055.
- Sheth, R. K., Mo, H. J., & Tormen, G. (2001). Ellipsoidal collapse and an improved model for the number and spatial distribution of dark matter haloes. *Monthly Notices of the Royal Astronomical Society*, *323*, 1–12.
- Sheth, R. K., & Tormen, G. (2004). Formation times and masses of dark matter haloes. *Monthly Notices of the Royal Astronomical Society*, *349*, 1464–1468.
- Sheth, R. K., & van de Weygaert, R. (2004). A hierarchy of voids: Much ado about nothing. *Monthly Notices of the Royal Astronomical Society*, *350*(2), 517–538.
- Springel, V. (2004). The largest N-body simulation of the universe. MPA research highlight of August 2004. last accessed:2022-08-24.  
URL [https://wwwmpa.mpa-garching.mpg.de/mpa/research/current\\_research/h12004-8/h12004-8-en.html](https://wwwmpa.mpa-garching.mpg.de/mpa/research/current_research/h12004-8/h12004-8-en.html)
- Springel, V. (2005). The cosmological simulation code GADGET-2. *Monthly Notices of the Royal Astronomical Society*, *364*(4), 1105–1134.
- Springel, V., & Hernquist, L. (2003). Cosmological smoothed particle hydrodynamics simulations: A hybrid multiphase model for star formation. *Monthly Notices of the Royal Astronomical Society*, *339*, 289–311.
- Springel, V., White, S. D. M., Jenkins, A., Frenk, C. S., Yoshida, N., Gao, L., Navarro, J., Thacker, R., Croton, D., Helly, J., Peacock, J. A., Cole, S., Thomas, P., Couchman, H., Evrard, A., Colberg, J., & Pearce, F. (2005). Simulations of the formation, evolution and clustering of galaxies and quasars. *Nature*, *435*, 629–636.
- Springel, V., White, S. D. M., Tormen, G., & Kauffmann, G. (2001). Populating a cluster of galaxies - I. Results at  $z=0$ . *Monthly Notices of the Royal Astronomical Society*, *328*(3), 726–750.
- Sutter, P., Lavaux, G., Wandelt, B., Weinberg, D., & Warren, M. (2013). The dark matter of galaxy voids. *Monthly Notices of the Royal Astronomical Society*, *438*.
- Sutter, P. M., Elahi, P., Falck, B., Onions, J., Hamaus, N., Knebe, A., Srisawat, C., & Schneider, A. (2014a). The life and death of cosmic voids. *Monthly Notices of the Royal Astronomical Society*, *445*(2), 1235–1244.

- Sutter, P. M., Lavaux, G., Hamaus, N., Pisani, A., Wandelt, B. D., Warren, M. S., Villaescusa-Navarro, F., Zivick, P., Mao, Q., & Thompson, B. B. (2014b). VIDE: The Void IDentification and Examination toolkit. *Astrophysics Source Code Library*, (p. ascl:1407.014).
- Tornatore, L., Borgani, S., Dolag, K., & Matteucci, F. (2007). Chemical enrichment of galaxy clusters from hydrodynamical simulations. *Monthly Notices of the Royal Astronomical Society*, 382(3), 1050–1072.
- Tweed, D., Devriendt, J., Blaizot, J., Colombi, S., & Slyz, A. (2009). Building merger trees from cosmological N-body simulations - Towards improving galaxy formation models using subhaloes. *Astronomy & Astrophysics*, 506(2), 647–660.
- Vallés-Pérez, D., Quilis, V., & Planelles, S. (2021). Void replenishment: How voids accrete matter over cosmic history. *The Astrophysical Journal Letters*, 920(1), L2.
- van de Weygaert, R. (2018). COSMIC STRUCTURE FORMATION. Lecture Notes. Last accessed: 2022-08-24 .  
URL <https://www.astro.rug.nl/~weygaert/tim1publication/lss2018/>
- van de Weygaert, R., & van Kampen, E. (1993). Voids in Gravitational Instability Scenarios - Part One - Global Density and Velocity Fields in an Einstein - De-Sitter Universe. *Monthly Notices of the Royal Astronomical Society*, 263, 481.
- van den Bosch, F. C. (2002). The universal mass accretion history of cold dark matter haloes. *Monthly Notices of the Royal Astronomical Society*, 331, 98–110.
- van den Bosch, F. C. (2020). ASTR 610 Theory of Galaxy Formation. lecture notes. last accessed:2022-07-12.  
URL <http://www.astro.yale.edu/vdbosch/astro610>
- Walker, S., Simionescu, A., Nagai, D., Okabe, N., Eckert, D., Mroczkowski, T., Akamatsu, H., Ettori, S., & Ghirardini, V. (2019). The Physics of Galaxy Cluster Outskirts. *Space Science Reviews*, 215(1), 7.
- Zel'dovich, Y. B. (1970). Fragmentation of a homogeneous medium under the action of gravitation. *Astrophysics*, 6(2), 164–174.
- Zhang, C., Churazov, E., Dolag, K., Forman, W. R., & Zhuravleva, I. (2020). Encounters of merger and accretion shocks in galaxy clusters and their effects on intracluster medium. *Monthly Notices of the Royal Astronomical Society*, 494, 4539–4547.
- Zinger, E., Dekel, A., Birnboim, Y., Kravtsov, A., & Nagai, D. (2016). The role of penetrating gas streams in setting the dynamical state of galaxy clusters. *Monthly Notices of the Royal Astronomical Society*, 461(1), 412–432.

Zonca, A., Singer, L., Lenz, D., Reinecke, M., Rosset, C., Hivon, E., & Gorski, K. (2019). Healpy: Equal area pixelization and spherical harmonics transforms for data on the sphere in Python. *The Journal of Open Source Software*, 4, 1298.

# Acknowledgments

This thesis would have never been written without the support from a considerable list of people. I would like to thank Klaus Dolag for offering me a thesis in his fantastic group and his never dwindling stream of new ideas and impulses he offered during the many discussions we had over the last year. Whenever I entered his office to find him at his whiteboard I knew that the next 60 minutes would be well spent. Additionally I owe gratitude to Andreas Burkert for his support of my work and many interesting discussions and suggestions during my time in the CAST group. The opportunity to meet the community during my master's thesis and discuss my work and the work of a number of inspiring scientists at the annual EAS meeting in Valencia in July was an invaluable boon to my scientific development.

I am grateful for the support, both spiritual and scientific, I enjoyed from the terrific trifecta of Rhea-Silvia Remus, Lucas Valenzuela and Lucas Kimmig, especially – but not limited to – the closing phase of writing this thesis. Thank you for being a great team! Furthermore I would like to mention Sivlio Fortuné and Tadziu Hoffmann for the many elucidating scientific conversations we had in the past year and Tadziu again for offering the best support for all things technical one could hope for. A big thank you is also owed to Ludwig Böss for his very useful Julia<sup>1</sup> libraries, which I used for most of my postprocessing routines. All of the aforementioned people were also present in some constellation in the very instructive group meetings for the CAST, Hydrosims and DRAGONS teams respectively. Thank you also to all the other group members that made those meetings worthwhile and especially for the always enlightening discussions we had after the talks. The second part of this thesis would not have been possible without the helpful collaboration with Jochen Weller's physical cosmology group. In particular I would like to thank Nico Hamaus and Nico Schuster for helping me get started with VIDE and voids in general.

Last, but definitely not least, I owe the completion of this thesis to the undying support from my girlfriend, my family and my friends. Thank you so much for walking this path with me!

I would like to end as I started on a befitting quote this time by Berthold Brecht. He ends his book *Der gute Mensch von Sezuan* with the following iconic sentence (that unfortunately does not translate well to english): "Wir stehen selbst enttäuscht und sehn betroffen // Den Vorhang zu und alle Fragen offen." (Brecht, 1964). Contrary to Brecht's statement though, I would argue that in science, open questions are a *good* thing.

---

<sup>1</sup>[www.julialang.org](http://www.julialang.org)



# Selbstständigkeitserklärung

Hiermit erkläre ich, die vorliegende Arbeit selbstständig verfasst zu haben und keine anderen als die in der Arbeit angegebenen Quellen und Hilfsmittel benutzt zu haben.

München, 09.09.2022

---

Benjamin Seidel